Synthesis and Aerosol-phase Treatments of Environmental and Materials Nanoparticles

A DISSERTATION
SUBMITTED TO THE FACULTY OF THE GRADUATE SCHOOL
OF THE UNIVERSITY OF MINNESOTA
BY

Brandon James Winters

IN PARTIAL FULFILLMENT OF THE REQUIREMENTS
FOR THE DEGREE OF
DOCTOR OF PHILOSOPHY

Jeffery T. Roberts

August 2011

Acknowledgements

Many long hours have been spent working toward this goal. I am humbled by the talent and selflessness of the people who have surrounded me along the way. Not only did these individuals act as catalysts for deeper investigations, they often offered unique and valuable insights leading to new understandings. For all of your efforts, I am forever indebted.

For all of the help with new instrumental techniques and good conversations with friends I would like to thank the people I have become closest to. To Steven Calder, thank you for your valuable insights and random conversations, I always looked forward to chatting with you. To Jason Holm, thank you for your great insights into the silicon nanoparticles and your help getting me started with these projects. I could not have done this without your help. To Aalo Gupta, Matt Jansma, and Susie Emond, thank you for your friendship. At the start, your friendly faces and welcoming personalities offered more comfort than you will ever know. To Melissa Fierke, thank you for the help using the Stein group instruments, but more importantly, thank you for good conversations about teaching and future plans. Your company filled much of the gap of being alone in the department. Finally, I wish each of you success as you move on.

While the responsibilities and obligations of a wife and growing family can take their toll, I don't think I could have remained sain if it were not for the wonderful distractions that home life is almost always certain to offer. Thank you Katie, my beautiful wife, for your enduring love and understanding. To Cameron, Levi, and Elsie, thank you for loving me even when I have been distracted and busy. I hope there is always time for family wrestling or a small game of baseball in the yard.

It would be impossible to ignore the impact of one's research advisor. Thank you Jeff, for adapting your advising to fit my needs. Whether by design or accident I am not sure, but your advising has always pushed me to improve from one day to the next. I have really enjoyed my time in your group and I am certain that I will be able to glean new insights into student advising in the coming years. I look forward to keeping in touch as I step into a new career.

I would be remiss if I didn't thank my personal Lord and savior, Jesus Christ, for the many blessings I have received. Through this process, I have often felt as though I was walking through the "valley of the shadow of death," I have been humbled and discouraged, but you have been their every step of the way. It has been a delight to see your hand at work in my life and to lean more heavily on you than I ever thought possible. I am more certain today than ever that this success is yours, not mine. From the bottom of my heart, thank you.

Dedication

This dissertation is dedicated to my wife, Katherine, who stood by my side day after day as I struggled to find motivation, and to my children, Cameron, Levi, and Elsie for their unfailing love.

Table of Contents

Chapter 3

Nanostructural Changes to Thermally Oxidized Natural Gas Soot

Chapter 4

Sulfuric Acid Treatment and Water Adsorption of Freshly Generated Natural Gas Soots

List of Tables

Chapter 3

List of Figures

Chapter 1

Chapter 2

Chapter 3

Chapter 4

Chapter 1

Introduction to Aerosols and Nanoparticles

The following chapter is intended to serve as an introduction to aerosol and nanoparticle chemistry. For the work presented herein, all primary aerosol particles have been shown to be in the low nanometer size regime. An introduction to nanoparticles will be presented alongside the aerosol introduction. The characterization of nanoparticles based on four characteristics (size, composition, shape, and surface) will be explored primarily in terms of techniques that will be used in subsequent chapters. The work presented in this thesis has been focused on two areas of research: silicon nanoparticles and soot nanoparticles. Both of these lines of work have utilized aerosol phase synthesis and processing. An introduction to the background and some pertinent information about silicon and soot is given in sections 1.3 and 1.4 respectively. Each of the following chapters will include an additional introduction that is more clearly focused on the line of research in question.

1.1 Introduction

Aerosols , defined as any “assembly of liquid or solid particles suspended in gaseous medium long enough to enable observations” (Baron and Willeke 1993), are all around us. Ranging in size from many microns in diameter to only several nanometers (Seinfeld and Pankow 2003), they can be naturally occurring or anthropogenic, and derived from many sources including pollen, spores, bacteria, viruses (Sengupta, Brar et al. 2007), cosmetics, sunscreens, pigments, catalysts, pharmaceuticals, building materials and electronic devices (Burleson, Driessen et al. 2004). Being either liquid or solid they may take on many different shapes including spherical, crystalline, fibrous or irregular and can be organic, inorganic or biological (John 1993). The smallest of aerosol particles essentially behave like large gas molecules, while larger ones react to inertial forces (John 1993). Aerosols are very complex.

Naturally occurring aerosols belong to one of three general categories: continental, marine, or urban (John 1993) and are believed to comprise 65% - 95% of the global aerosol mass, with an ever growing contribution from anthropogenic sources (Maynard and Kuempel 2005). While research, in general, is aimed at improving our quality of life through gaining better understanding (Masciangioli and Zhang 2005), aerosols are known to effect human health, climate, visibility and deposition of pollutants (DeCarlo, Slowik et al. 2004). This means that without careful development there exists a real dichotomy in the area of aerosol research; new developments could very well create new health and environmental hazards. Within the past several years interest in nano-scale aerosols has grown dramatically and with it concern regarding hazards

associated with these ultrafine materials (Maynard and Kuempel 2005). It has been shown in several cases that the smallest aerosols can cause significant health problems (Brown, Wilson et al. 2001; Cassee, Muijser et al. 2002). Brown et al., for example, have shown that inhalation of polystyrene nanoparticles present significant health risks (Brown, Wilson et al. 2001). Furthermore, for many particles the potential hazards depend strongly on the chemical state of the atoms contained within the particle (Burleson, Driessen et al. 2004).

Recently there has been a shift in the motivation for aerosol research. For several decades the primary interest was in the area of particulate pollution control. While that subject will remain important, new applications of engineered nanomaterials have brought with them a great deal of interest in gas-to-particle production methods, requiring new methods for aerosol characterization and monitoring (John 1993). While nanoparticles and aerosols are not mutually inclusive topics, these new production methods have created a common ground in that nanoparticles are now being produced in the aerosol phase.

Nanoparticles are defined to be 1 - 100 nm in diameter. These ultra small particles could be used in a diverse array of applications ranging from renewable energy sources like “paintable” self-assembling photovoltaic cells to “smart dust”, which are sensors and observations devices incorporated into small particles (Mulhall 2005). These “dust” particles could contain cameras, communications devices and sensors for temperature, chemicals and sound (Mulhall 2005). Nanotechnology is likely to be a significant contributor to the 21st century economy (Dabrowski and Mussig 2000) and is

expected to play a huge role in reducing world energy needs through use of fewer resources, less energy for manufacturing, and more efficient electronics and automobiles (Masciangioli and Zhang 2005). For example, as of the year 2000 it was believed that widespread use of high brightness light emitting diodes (LEDs), developed through nanotechnology, could cut the US's energy demand in half by 2020 (Masciangioli and Zhang 2005). This reduction could result in over $100 billion in savings over 20 years (Masciangioli and Zhang 2005). Furthermore, nanotechnology is known to address a wide range of sustainability issues. Global climate change, depletion of resources, population related problems like infectious disease, urbanization and social disintegration, and environmental degradation are the five main categories of sustainability that nanotechnology can play a major role in (Karn 2005). For example, nanotechnology has the potential to improve drinking water conditions worldwide through the development of better sensors and filters for detecting and removing pollutants and toxins (Karn 2005). Nanotechnology should also enable a large reduction in chemical use for manufacturing resulting in less toxic waste and fewer unwanted byproducts (Karn 2005).

For all the positive interest in nano-development, however, there is ample concern regarding issues of nanoparticle's potentially negative biological and environmental impacts, as well as concerns about nano-terrorism through development of new toxins, disease organisms, and crop killing agents (Karn 2005). With such a wide range of possible benefits and hazards associated with nanotechnologies, it is clear that thought and discussion must happen simultaneously with development, but research into the

fundamental chemistry and possible applications of nanoparticles should not be put on hold.

Nanomaterials can have different properties than their bulk material counterparts, indeed, this is cause for a great deal of interest in their application (Maynard and Kuempel 2005). Chemical, mechanical, electrical, optical, magnetic and biological properties are known to be different in the bulk and engineered nanomaterials (Maynard and Kuempel 2005). For example, Buffat and Borel showed that the melting temperature of crystalline gold nanoparticles was lower than that of bulk crystalline gold (Buffat and Borel 1976). The differences in the properties of nanomaterials are often attributed to the large relative surface area of particles. While bulk materials have a relatively small number of atoms or molecules on the surface, a nanoparticle 5 nm in diameter has half of its atoms at the surface (Burleson, Driessen et al. 2004). This means that the properties of the particle are influenced much more heavily by the properties of surface atoms. On the surfaces of nanoparticles, atoms are typically undersaturated or bonded to species other than the bulk (Burleson, Driessen et al. 2004). Due to changes in size-dependent properties and the increased relative surface area of nanoscale materials, their controlled production is very important. Moreover, a single nanoscale contaminant on a circuit board has the ability to ruin the entire circuit (Willeke and Baron 1993). As a result, researchers are interested in developing a deeper understanding of aerosol chemistry. While there are currently characterization techniques available for studying these particles on substrates or in thin films, the deposition of particles to a surface can change

their surface characteristics (Keller, Fierz et al. 2001). It is therefore, important to characterize them in the gas/aerosol phase.

While the surface of a particular particle is very important to its chemistry, the shape and porosity are perhaps equally important (Burleson, Driessen et al. 2004). These factors along with the ultra small size, and often undefined composition of the materials are what make nanomaterials a complex research endeavor (Seinfeld and Pankow 2003). In order for new applications of nanoaerosols to be developed in a manner in which they are both biologically and environmentally friendly as well as useful, it is crucial to understand more about their specific chemistry. This means gaining a deeper understanding of particle size, density, composition, shape, and surface reactivity. Each of these factors presents new challenges and requires different characterization methods.

1.2 Aerosol Characterization

As mentioned above, aerosol characterization which requires a diverse arsenal of techniques has been and ongoing area of research for many years (Willeke and Baron 1993). Aerosol measurements are classified by the quantity or characteristic being measured (Lehtimaki and Willeke 1993). The most common of which is particle concentration. This is generally defined as the mass of particles per unit volume of gas, but can be redefined to include only a small subset of particles within the whole sample or even the surface area, charge density or volume of a sample of particles (Lehtimaki and Willeke 1993). One of the limiting factors of existing aerosol measurement techniques is that each technique covers only a finite range of particle sizes,

concentrations, shapes and compositions, so the proper technique must be chosen based on the purpose of the work (John 1993).

In general, characterization can happen in one of two ways: on-line or off-line(McMurry 2000). For off-line characterization, particles may be collected on a filter or substrate and preserved for analysis at some later time. Several major advantages of this are the relatively cheap cost of most off-line characterization techniques, the ability to conduct studies under different conditions than the production apparatus allows, and the often simple setup for these measurements (Lehtimaki and Willeke 1993). Two primary disadvantages, however, are the time delay between particle production and characterization, and possible chemical changes in particles due to ambient exposure (Lehtimaki and Willeke 1993).

On-line measurements are taken in real-time and do not expose the particles to ambient environment. This also allows for particles to be analyzed in the aerosol phase immediately after production or even during production to obtain time resolved data on the mechanism of particle growth. A severe limitation of many on-line measurements, however, is that they offer little information about particle chemical composition. They are also typically very expensive and are not usable in harsh conditions. In the following sections, several pertinent aerosol characteristics will be discussed with some instrumental techniques that accompany them. It should be noted that this is not an exhaustive list of particle properties or characteristics, but rather ones that are significant to later work, which will be presented in the subsequent chapters. Techniques that will be used in later chapters will be labeled as such.

1.2.1 Particle Size

Particle size affects the motion of particles through an aerosol system since particle size changes their aerodynamic properties. For many techniques, the flow of particles though an aerosol system must be well controlled. In an ideal case, the particle stream would be monodisperse with regard to diameter, but this is not typically possible. Furthermore, the term "monodisperse" does not carry with it a well-defined parameter for aerosol particles. While there is beginning to be some agreement among scientists that a monodisperse aerosol stream must have a calculated standard deviation less than 1.2, this is not a general concensus (Lehtimaki and Willeke 1993).

Particle size affects more than just characterization, it often defines useability (Holm and Roberts 2007). For some applications this is ultimately due to restrictions based on the purpose. For example, the particles in nanoaerosols used for inhalated drug applications may need to be less than 100 nm in diameter but larger than 5 nm to obtain the best efficacy (Oberdorster 2005). For other applications the size restriction maybe due to the occurrence of a desired property within a narrow size range. He et al. have shown that 45 ± 4 nm diameter silica nanoparticles bioconjugated with amino acids are able to protect DNA from cleavage (He, Wang et al. 2003). Whatever the case, both controlling and characterizing particle size are of critical importance to aerosol science.

Off-line measurements of aerosols may be made using many different approaches. For example, samples may be collected on a substrate for transmission electron microscopy (TEM) and then direct measurements of their diameters can be made (Holm

and Roberts 2007). This can be very tedious if an average particle diameter is desired because a minimum of 10,000 individual measurements are needed for a such a calculation, but it is very effective for small numbers of particles and is currently the method with the best resolving power (Burleson, Driessen et al. 2004). This method will only be used in the most qualitative sense for the work presented here allowing for qualitative observations of primary particle diameters and agglomerate shapes.

When an average particle diameter is needed, on-line methods are most often used, these measurements can be made in several ways. Three common measurements are aerodynamic size, diffusion battery and electrical mobility analysis (McMurry 2000). It is pertinent to note that the actual physical size of particles is not measured using these on-line techniques. Instead, other physical properties of the particles are measured and then used to equate equivalent sizes (Baron and Willeke 1993). Equivalent size is defined as the diameter of a sphere that would give the same measurement as the particle being measured (DeCarlo, Slowik et al. 2004). Because different sets of properties can result in the same equivalent diameter, producing particles with uniform properties is crucial. For example, when measuring particles using aerodynamic particle size analysis, aerosol particles accelerated through a nozzle will accelerate more slowly than the carrier gas (McMurry 2000). Additionally, larger particles will accelerate more slowly than smaller ones; this difference in acceleration is measured and used to assign particle diameters based on known quantities (McMurry 2000). Therefore, particles of uniform density and surface structure are needed to ensure that measurements are accurate because aerodynamic size equivalents are based on equal gravitational settling velocities

(Baron and Willeke 1993). Diffusion batteries, on the other hand, are used to classify particle size distributions by measuring the rate at which particles are depositing on a surface. As particle size increases the rate at which particles deposit decreases (McMurry 2000).

Finally, electrical mobility is measured by flowing an aerosol stream past a charged electrode and relies on different trajectories for charged particles of varying sizes. The force exerted on the charged particles as they travel through the atmospheric pressure analyzer is what separates them and causes different trajectories. Electrical mobility diameter (d_m) is defined as the diameter of a sphere that has an equivalent migration velocity to the particle, under a constant electric field. It assumes that all particles are spherical in shape and equally charged, but is currently considered, by some, to be the best method for determining particle size distributions (McMurry 2000) with an ultimate size resolution of 0.05 ± 0.02 nm (Liao, Nienow et al. 2006). Figure 1 shows a diagram schematic of a differential mobility analyzer (DMA) (TSI, Inc. model 3085 nano DMA). Once the particles are produced they are uniformly charged in a bipolar diffusion charger and then introduced into the DMA, which operates near atmospheric pressure. The DMA size selects particles by applying a constant DC charge to the central rod electrode, while keeping the outer casing electrically grounded. Particles with mobility diameters too great or too small follow trajectories that exclude them from the sampling stream (·····), but particles with the proper mobility diameter follow a trajectory that places them in the size-selection stream (- - - -). The voltage bias of the DMA is stepped from low to high voltage while the particles are optically counted in an ultrafine

condensation particle counter (UCPC). This process generates a particle size distribution. The further use of this technique with tandem DMAs used to measure size changes in aerosolized nanoparticles will be discusses in Chapter 4.

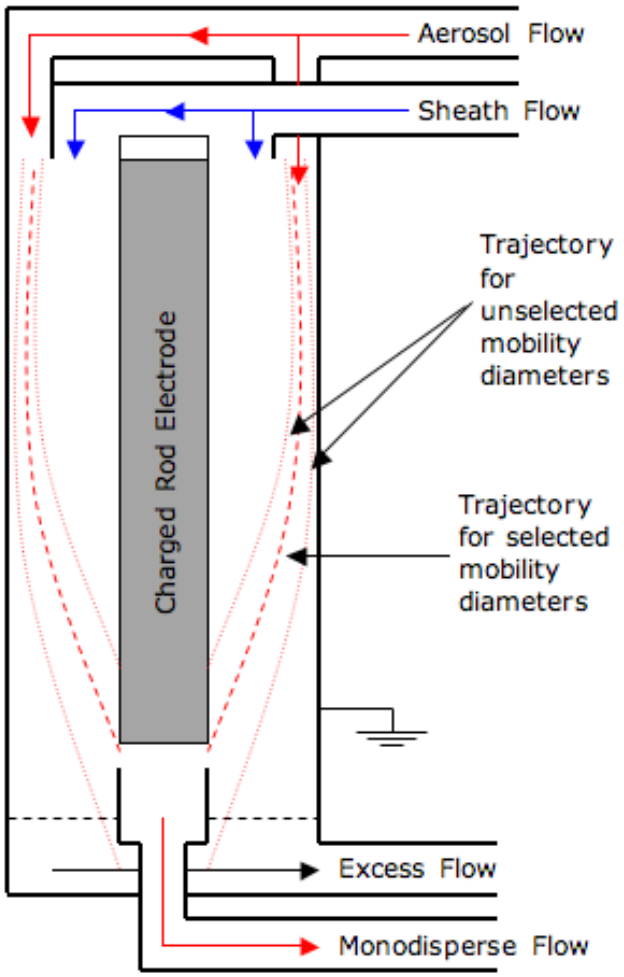

Figure 1.1: Schematic diagram of a differential mobility analyzer

1.2.3 Particle Composition

Particle composition is at the foundation of particle reactivity. While the often-unexpected properties of particles are thought due to size effects, the composition ultimately defines reactivity. There are several on-line measurement techniques for particle composition, but they are mainly in the development stage (McMurry 2000) since online techniques will require much lower detection limits. One technique that seems particularly well suited for online compositional analysis is Fourier transform infrared spectroscopy (FTIR). Flow cells have been built that allow for the measurement of the particles within the aerosol stream, but they require long beam path lengths due to the low concentration of particles in the aerosol phase. In light of this difficulty, FTIR has been adapted to perform quasi-online measurements by collected particles on an IR transparent filter media and passing the beam through the sample without opening the collection cell to ambient. Figure 2 shows an illustration of one such cell that has been used for this work. The collection of samples necessary for the quasi-online measurements allows for future off-line measurements of the same samples using other techniques and makes for easy incorporation of various sample treatment techniques.

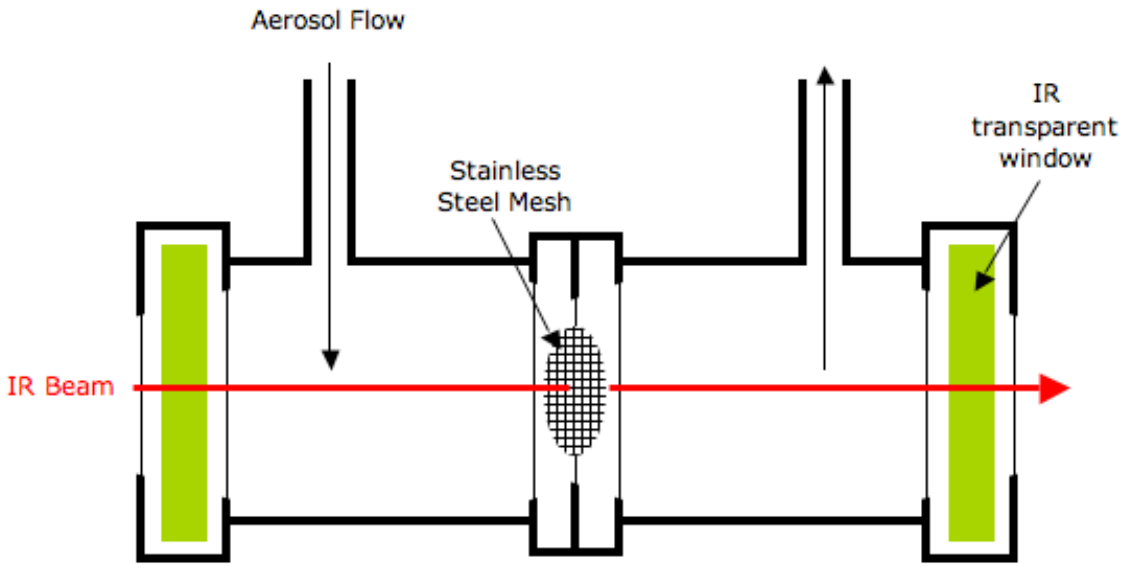

Figure 1.2: Schematic diagram of a quasi-online FTIR aerosol collection cell

Aerosol mass spectrometry is an area of explosive recent development. If the aerosol system can be designed in a way that allows for sample insertion into the mass spectrometer, this can be a very powerful compositional tool. For example, Smith *et al.* have used mass spectrometry in tandem with DMA to analyze the composition of freshly nucleated ambient aerosol particles in the size range 6-15 nm. Their analysis has shown that ammonium and sulfate are important components of these fresh aerosol particles (Smith, Moore et al. 2005). Mass spectrometry can also be performed off-line through the use of various ionization sources. The sample need only be collected in a way that allows for the insertion of the sample into the instrument and subsequent ionization. Care should be taken to avoid sample preps that change the particle composition however.

Once the ionized in the spectrometer, it is able to detect both organic and inorganic compounds as well and differentiate surface from bulk ions.

Off-line measurements carry with them the risk of inadvertently modifying the particle through ambient exposure (McMurry 2000), but they can, nonetheless, provide in-depth information about particle composition. Some off-line techniques include electron microscopy, atomic force microscopy (AFM), gas chromatography, X-ray photoelectron spectroscopy (XPS), and differential scanning calorimetry – thermo gravimetric analysis (DSC-TGA). While these techniques are currently and traditionally thought of as off-line, the adaptation of any aerosol production system to develop new ways of performing on-line measurements is perhaps one of the greatest advantages of aerosol-phase research.

Electron microscopy can extract several different measurements of individual particle features: atomic scale structure, chemical composition, and crystal structure (Burleson, Driessen et al. 2004). For the present work, transmission elctron microscopy has been used with electron energy-loss spectroscopy and is presented in Chapter 2.

XPS relies on the photoelectron effect where an electron is ejected from the sample when it is irradiated with an X-ray source. In an ideal case, the measured energy of the ejected electron is equal to the binding energy of the atomic shell it originated in. These energies shift according to the specific bonding of the material being analyzed and can give in-depth information about composition. For these studies, XPS has been utilized for the analysis of silicon nanoparticles (Chapter 2). The oxidation state of the nanoparticles in analyzed as a function of ambient exposure time.

AFM is typically used for measurements of particle size, shape and topography, but can be adapted, through the use of special cantilever tips, to measure forces such as adhesion, and sliding friction (Burleson, Driessen et al. 2004). These quantities can be used in determining chemical composition along with particle properties like hardness and relative adhesion, but it must be remembered that the chemistry cannot be directly measured; it must be inferred from other known relationships (Burleson, Driessen et al. 2004).

The use of DSC-TGA does not give compositional information in the same way that FTIR can, but the peaks and valleys observed in the DSC spectra can yield a wealth of information nonetheless. For this technique, a sample of known mass is placed in a small crucible and then this and an empty reference crucible are placed into a furnace. The furnace temperature is ramped at a constant rate and the difference in temperature from the reference crucible and the sample is monitored. From this, the change in heat relative to the reference can be calculated. For the work presented here (Chapter 3) the DSC plot yields information about the general types of adsorbed species and chemical processes occurring at a given temperature.

1.2.4 Particle Shape

Most aerosols will form complex architectures, even if single spherical particles are produced, unless production conditions are carefully monitored. During or after particle production particles will typically aggregate to form more complex structures. Due to the many different shapes that can be formed, shape is traditionally accounted for

by a single mathematical parameter within the aerosol motion equations. This parameter, the shape factor, does not include detailed information about the particle's shape, but can help account for much of its motion (Baron and Willeke 1993). With the advent of ever greater computer power, it has become possible to characterize the outline and texture of a particle more fully, but this too is not without problems. First, accounting for the shape of each individual particle is not practical, so the shapes of a few are typically assumed representative of the whole. Second, as mentioned above, particles will often aggregate and when they do it is common for a particle to take on a fractal dimension. That is, the complexity of the particle is similar on several different length scales. Using **Figure 3** as an example, as higher and higher magnification is used to measure the outline of the particle, going from a to b to c, its perimeter will get longer and longer. These measurements can either be done by hand with a series of magnified images or with the help of computer software. In the end, a single mathematical parameter is still calculated and included in the particle motion equations, but it is not a whole number; the particle is described as being some fraction of a three dimensional object (Baron and Willeke 1993).

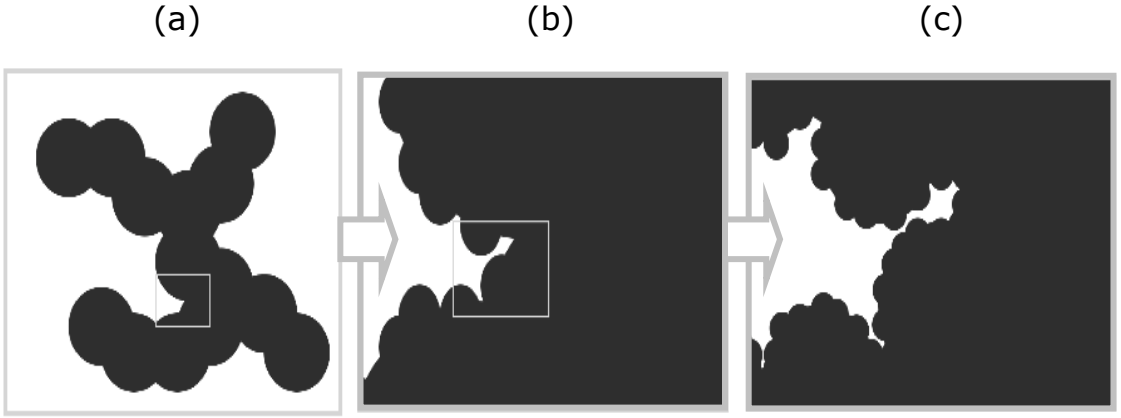

Figure 1.3: The fractal dimension of an irregular particle, increasing zoom level from a to c

1.2.5 Surface

Although the size, density, composition and shape of aerosol nanoparticles are all important, it has been suggested that the surface is more important. There are two major characteristics of a particle surface, the surface area and chemical makeup (Keller, Fierz et al. 2001). In many cases the surface area is calculated by assuming a spherical shape of the particles and then using the measured diameter to calculate the surface area of a sphere of equivalent diameter (Keller, Fierz et al. 2001). While this has some shortcomings, in cases where particles are relatively spherical, it can be very accurate. The second characteristic of particle surfaces that can be characterized is the chemical composition. Some of the methods previously mentioned can be used to that end (ie. AFM, TEM, FTIR, and XPS), but by and large these techniques are unable to detect single particles in the low nm size regime.

New challenges have presented themselves as smaller and smaller particles are being produced. For example electron microscopy has been used to make elemental composition measurements of a single particle, while the electron beam width has been decreased considerably in recent years, sample drift and nano-scale particle dimensions make it difficult to clearly examine the smallest discrete particles (Lehtimaki and Willeke 1993). This is a real problem for many researchers today because of the large number of gas-to-particle generators being used in the production of nanometer scale particles. It has become particularly difficult to characterize these particles, as there are not many characterization techniques available. For the electron energy loss spectroscopy (EELS) work presented in Chapter 2, line scans across particles were performed in an effort to

dimensionally resolve chemical information. The beam was controlled to ~ 0.5 Å, but the constant drift of the sample within the instrument made this analysis all but impossible. For larger particles, or thicker features, this technique could be used very effectively.

1.3 Silicon Nanoparticles

Silicon represents an attractive target for nanoparticle research for several reasons. First, it is abundant and relatively cheap. Its fractional composition of the earth's crust is 25.7%; only oxygen is more abundant. In fact, silicon, while not found in its elemental form naturally, is found in a rich number of sources ranging from sand to garnet. Second, it has been used as the cornerstone for electronics for several decades. It has been said that if it were not for the combination of silicon dioxide's and elemental silicon's properties, "the information revolution might have been delayed" (Dabrowski and Mussig 2000). Silicon's importance, however, is not new. Over the centuries it has been used by humanity for making clay pots, steel and glass to list only a few in a litany (Dabrowski and Mussig 2000). That being said, it can be argued that silicon is one of the most important elements to human survival and prosperity. Next, silicon in its bulk crystalline form is known to be biologically nontoxic. While silicon nanomaterials may prove to exhibit different properties in this regard, it is currently thought that they are very similar to bulk silicon (Holm and Roberts 2007). Finally, silicon can form a stable Si-C bond for functionalization. Many other popular nanodevelopment materials, including germanium, are not able to form stable bonds with carbon (Buriak 2002).

While inorganic means have also been used to functionalize silicon surfaces, the ability to attach organic monolayers could presumably open a wider range of functionalities and applications (Buriak 2002).

Recent nanodevelopment with silicon has centered largely around nanoparticles and their applications as luminescent devices (Hua, Erogbogbo et al. 2006), nontoxic biological tags (Zou, Baldwin et al. 2004), single particle transistors(Holm and Roberts 2007) and solar cells (Liao and Roberts 2006). Considering the significance of these applications, it is important to gain a clear understanding of their chemistry and reactivity. First, the production of well-defined nanoparticles is of critical importance. Without a well-developed understanding of how production conditions affect particles' characteristics, there is little hope of their widespread use and development. Second, the surface chemistry of silicon nanoparticles (Si-nps) is crucial because under ambient air conditions they are subject to rapid surface oxidation resulting in decreased efficacy in optical and electronic devices. Moreover, many current and proposed applications require surface passivation or functionalization (Liao and Roberts 2006).

Chapter 2 of this work will deal specifically with the ambient oxidation of silicon nanoparticles. The ability of these nanoparticle to resist oxidation will likely dictate their future use in various applications. More information about the justification for this specific work can be found in the introduction to Chapter 2.

1.4 Soot Nanoparticles

Soot is the product of incomplete combustion of fossil fuels or biomass. The anthropogenic volume emitted each year from the burning of fossil fuels alone is estimated to be near 24 x 10^{12} g (Tg C $year^{-1}$) (Smith and Chughtai 1997; Aubin and Abbatt 2003). Also known as black carbon or elemental carbon, these particles are a major part of the particulate matter found in the upper troposphere (Kuhn, Petzold et al. 1998). Once in the atmosphere soot particles can have profound effects on climate and health. Soot particles have been linked with respiratory disease and are known to contain small fractions of carcinogenic compounds. Depending on their size and composition, they can have positive or negative effects on the Earth's radiative budget (Smith and Chughtai 1995; Jensen and Toon 1997). Small soot particles are known to be a major source of cloud condensation nuclei (CCN), they act as seed particles on which the moisture in the atmosphere is able to condense forming cloud droplets (Seinfeld and Pandis 1998). Furthermore, it has been shown that soot particles specifically from air traffic have effects on the life-cycles and properties of cirrus clouds (Kristensson, Gayet et al. 2000). There is some uncertainty, however, as to how these hydrophobic particles are able to serve as CCN.

Developing an understanding of the process by which hydrophobic soot particles are activated to serve as CCN has required the use of various laboratory soots which have been shown to vary significantly in their hydroscopic properties (Lammel and Novakov 1995; Diehl and Mitra 1998; DeMott, Chen et al. 1999). It is currently thought that the specific properties of individual soot particles strongly influence their ability to act as

CCN. These properties include the size and composition of the graphene crystallites (Polschl, Schauer et al. 2001), the surface chemical composition, micro and meso porosity (Popovicheva, Persiantseva et al. 2008), and adsorbed organic compounds. It has also been shown that coating particles with soluble compounds reduces hydrophobicity (Andrews and Larson 1993). Although the aging process of soot is not well understood, various studies have made significant progress in this area. It has been shown that the water uptake of soot particles does increase when they are aged in air (Chughtai, Brooks et al. 1996) and that initial condensation of water occurs at surface sites with oxygen-containing functionalities (Dubinin 1980). Further studies have shown that the mechanism through which water condenses onto soot particles can vary from sample to sample. For soluble particles, activation as CCN follows Kohler theory while for insoluble particles it follows an inverse Kelvin effect (Persiantseva, Popovicheva et al. 2004). While it has been suggested that the aging process involves sulfates or sulfuric acid, it is clear that these species are not necessary for droplet activation (Karcher, Peter et al. 1996; Persiantseva, Popovicheva et al. 2004). Even though these species are not be necessary for activation, they and others (OH, O_3, HNO_3) are known to interact with soot in the atmosphere ultimately oxidizing the soot making it more hydrophilic (Kotzick, Panne et al. 1997; Chughtai, Williams et al. 1999; Kirchner, Scheer et al. 2000; Decesari, Facchini et al. 2002).

Once aged, water condenses onto the soot surface or absorbes into the porous structure and allows the particles to swell (Popovicheva, Persiantseva et al. 2008). After swelling, the particles can begin adsorbing more water allowing them to form droplets in

the atmosphere. These droplets reflect sunlight back out of the atmosphere contributing to a net cooling effect and decreasing precipitation. Particles that have not been activated, on the other hand, are strongly absorbing and have been shown to increase atmospheric temperatures (Zuberi, Johnson et al. 2005). It is clear that soot particles have complex structures, compositions, and morphologies giving rise to their complex influences on global climate and weather. Chapters 3 and 4 of this work will explore the influence of production conditions and post synthesis heating on graphene crystallite size along with the impact of these changes on the hydroscopic properties of natural gas soot. Each chapter includes a brief overview and introduction to the specific line of work.

Chapter 2

Thermal Processing and Native Oxidation of Silicon Nanoparticles

Fourier transform infrared spectroscopy (FTIR), x-ray photoelectron spectroscopy (XPS), and electron energy loss spectroscopy (EELS) were used to investigate in-air oxidation of silicon nanoparticles ca. 11 nm in diameter. Particle samples were prepared by first extracting them from an RF plasma synthesis reactor and then heating them in an inert carrier gas stream. The resulting particles had varying surface hydrogen coverages and relative amounts of SiH_x (x = 1, 2,3), depending on the temperature to which they had been heated. The particles were allowed to oxidize in air for several weeks. FTIR, XPS and EELS analyses that were performed over that period clearly establish that adsorbed hydrogen retards oxidation, but in complex ways. In particular, particles that have been heated to intermediate hydrogen coverages oxidize more slowly in air than do freshly generated particles that have a much higher hydrogen content. Additionally, the loss of surface hydride species at high processing temperatures results in fast initial oxidation and the formation of a self-limiting oxide layer. Analogous measurements made on deuterium-covered particles show broadly similar behavior, *i.e.* that oxidation is slowest at some intermediate coverage of adsorbed deuterium.

2.1 Introduction

The controlled production and functionalization of silicon nanoparticles represents an important target for further development of nano-scale electronics. These particles, when produced with diameters in the range 2-10 nm, fluoresce and are very desirable for a range of applications including light emitting devices,(Hua, Erogbogbo et al. 2006) single particle transistors,(Dong 2005) solar cells, and non-toxic biological tags.(Nayfeh 2003; Zou, Baldwin et al. 2004) While the controlled production of these particles using well-defined parameters has been achieved by us and others,(Liao, Nienow et al. 2006; Nienow and Roberts 2006; Bapat, Gatti et al. 2007; Holm and Roberts 2007; Kortshagen, Mangolini et al. 2007) most applications will require the ability to tailor specific surface chemistries and to passivate the particles against ambient reactions. The latter issue is particularly important because upon exposure to ambient conditions, the surfaces of silicon nanoparticles rapidly oxidize, causing a red-shift in light emission. This, in tandem with the desire to add new surface functionalities, has created a great deal of interest in strategies for the long-term passivation of silicon nanoparticles (Mayeri, Phillips et al. 2001; Carter, Harley et al. 2005; Liao and Roberts 2006; Rogozhina, Eckhoff et al. 2006).

The properties of nano-scale materials are known in many cases to vary from those of their bulk counterparts (Buffat and Borel 1976; Maynard and Kuempel 2005). Nanoparticles, which have very large surface area to volume ratios, have properties that are often dictated by their surface chemistries (Burleson, Driessen et al. 2004). In some cases, surface chemistry can be controlled at the nanoparticle production step. For

instance, depending on the specific precursor gas chosen (SiH_4 or SiD_4) and growth conditions, the surfaces of silicon nanoparticles particles can be terminated with either hydrogen or deuterium and with varying amounts of SiH(D), $SiH_2(D_2)$, and $SiH_3(D_3)$. While it is commonly accepted that bulk amorphous silicon oxidizes more slowly than crystalline silicon (Fritzsche 1984), this may not be the case for amorphous vs. crystalline nanoparticles (Mills, Dhandapani et al. 2003). Additionally, it has been shown that the oxidation of nano-scale particles and powders is sensitive to the oxidizing environment and that oxidation rates are sensitive to changes in particle size, shape, and surface chemistry (Tersoff, Tu et al. 1998; Kovalevskii, Shevchenok et al. 2008). Furthermore, many probable applications of silicon nanoparticles would require that they be exposed to air for extended periods of time. It has been suggested that the oxidation of silicon nanoparticles exposed to varying volume fractions of O_2 at temperatures ranging from room temperature to 1100°C follows a two-step shrinking core model (Liao, Nienow et al. 2006) and requires very little oxygen (Holm and Roberts 2007). While it is thought that both O_2 and H_2O in air are responsible for the formation of a silicon oxide layer on silicon (Miura, Niwano et al. 1996), further insight into this processes is needed.

Many techniques to process and functionalize silicon nanoparticles include a heating or annealing step (Hua, Erogbogbo et al. 2006; Rogozhina, Eckhoff et al. 2006). Heating, if capable of producing the desired results, is generally preferred for a variety of reasons including simplicity, adaptability, and relatively low cost of implementation. For these reasons and because heating can be used to perform myriad chemical reactions on silicon nanoparticles, it is important to gain greater insight into the changing surface

chemistries brought on by heat treatment of silicon nanoparticles. That being said, this study seeks to shed light on the process of native oxidation, specifically, the effect of thermal processing of synthesized particles on their susceptibility to oxidation upon subsequent exposure to air.

2.2 Experimental Details

2.2.1 Silicon Nanoparticle Synthesis

Silicon nanoparticles were synthesized in an RF plasma using a method that is extensively described elsewhere(Mangolini, Thimsen et al. 2005; Holm and Roberts 2007). Ultra-high purity argon carrier (Praxair, MN) and silane precursor (0.501% in Ar, Linde Gas Inc.) gases were introduced into the plasma cell where the silane underwent reaction in a nonthermal plasma generated by a radio frequency source (RF amplifier: Electronics and Innovation model A150, signal generator: Tektronics AFG3021) set to 13.56 MHz (Figure 1). Between 40 and 50 Watts of power was applied to the plasma cell which was constructed using a quartz tube approximately 10 cm in length and 6 mm in outside diameter. Two copper ring electrodes 6 mm wide were placed around the plasma cell with a gap of 25 mm and the plasma was maintained between these electrodes and slightly down stream from them at an operating pressure of ~7 Torr. As the gases, both inert carrier and reactive precursor, flowed through the plasma cell, silane reacted to form crystalline silicon nanoparticles, which were then further processed and studied.

Samples were collected for FTIR analysis using an home-built cell described elsewhere (Holm and Roberts 2007). In this study a reduced aperture was fitted in the IR cell to reduce the minimum cross sectional area of the cell thus allowing shorter collection times. The 25 mm aperture was most commonly used. A piece of stainless steel (s.s.) mesh (type 304, 400x400), having been washed in methanol and dried with house nitrogen, was mounted within the aperture for particle collection. IR scans to monitor surface composition of pristine and thermally processed particles were taken before opening the cell to ambient. Figure 1 is a schematic of the system as it was set-up for particle production, thermal treatment and IR characterization. The tube furnace (Lindberg/Blue model HTF55122A) was capable of operating at temperatures as high as 1200°C and had a temperature profile that was previously described (Figure 2) (Holm and Roberts 2007). The tube was Inconel steel. Special precaution was taken to bake the furnace at or above 850°C with 50-100 sccm Ar (ultra high purity) purge gas for a minimum of 60 minutes prior to use.

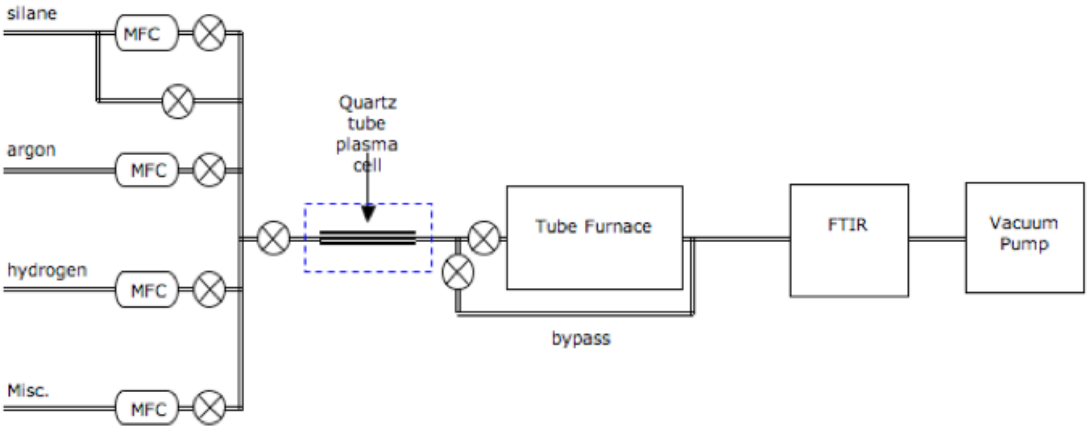

Figure 2.1: Schematic drawing of the gas-to-particle plasma system for synthesis, thermal treatment and FTIR analysis

2.2.2 Fourier Transform Infrared Spectroscopy

For native oxidation, the same *in situ* IR cell was used for collecting samples, as it preserved the planarity of the stainless steel mesh allowing for better consistency with diffuse reflectance infrared Fourier transform spectroscopy (DRIFTS). This method was used due to its capacity to handle samples having been collected on the stainless steel substrate along with its simplicity in collecting consistent time-delayed spectra of multiple samples. These samples were produced in the same fashion as the thermally desorbed samples, except that the IR cell was not contained within the IR bench. To ensure the apparatus was sufficiently purged of wet ambient air for each DRIFTS spectrum, the initial time for each set of data actually represents a delay of approximately 5 minutes from when the particles were initially exposed to ambient. After each sample was collected, it was placed on the DRIFTS stage and remained there for at least 90 minutes. This was done to minimize variation in signal strength due to sample

irregularities over that initial time frame. Thereafter, samples were removed from the IR bench and stored individually in small polystyrene boxes, which were left exposed to ambient conditions on the counter. Typical relative humidity (RH) levels were ~15% and the room temperature was maintained near 22°C. Due to irregularities of particle deposition on the mesh, samples were placed on the DRIFTS stage using visual inspection to align the laser to areas of the greatest particle coverage that also exhibited a high degree of co planarity with the stage itself.

Peak positions (ν^{max}) for FTIR spectra were obtained using OriginLab's Origin® 8 and performing a Gaussian fit at the tops of the peaks in question. Peak areas were calculated using OMNIC, the software provided by Nicolet Instrument Corporation. Peak range parameters were defined as follows: for the Si-H and Si-D stretching modes at 2100 and 1500 cm^{-1} respectively, 2175-1900 cm^{-1} and 1575-1400 cm^{-1}. The surface oxide peak near 1050 cm^{-1} was defined from a static lower limit at 950 cm^{-1} to a moving upper limit set as the tangential point where the baseline and peak met. The moving upper limit was used to ensure that the growing oxide peak was fully integrated. Peak areas represent the full spectral area within their respective bounds and ratios are presented as normalized fractional values.

2.2.3 X-Ray Photoelectron Spectroscopy

X-ray photoelectron spectroscopy (XPS) analysis was conducted on samples synthesized and collected using the same procedure, as those investigated by DRIFTS. To ensure consistency between samples, transmission FTIR was performed before allowing the samples to oxidize. Due to high ambient humidity when some experiments were performed, a Plexiglas humidity-control chamber was constructed to maintain ~15% RH during ambient exposure. Samples were initially kept under nitrogen until they were all ready to be loaded into the XPS system. Survey, as well as high resolution spectra, of Si 2p, O 1s, and C 1s regions were taken of four hydrogenated samples heated to 22, 400, 500, and 700°C at 0 min, 1 week, and 1 month ambient oxidation intervals. This was done using a Surface Science SSX-100 spectrometer. Due to the nonconductive nature of the samples, a charge neutralizer set to ~7 eV was used in conjunction with a stainless steel mesh to avoid charge build-up on the sample surface. For survey spectra, 3 scans were recorded with the spectrometer set to a spot size of 800 µm with a resolution of 1 eV over the range 0-1100 eV. High-resolution spectra were taken by changing the spectral ranges to center each specific peak and changing the resolution to 0.1 eV. The Si 2p region was then analyzed using the spectrometer analysis software suite. Between 2 and 5 peaks were fit to each spectrum, but the best fit was achieved in all but 3 spectra with a 2 peak model so these are the analyses presented in this work. The peaks at ~99 EV and 102 eV (NIST, 2003) are broadly attributed to either pure crystalline silicon or oxidized silicon respectively, and subsequently integrated to find the percent of the Si2p peak attributed to silicon oxide, these numbers will be reported at percents.

2.2.4 Transmission Electron Microscopy

Transmission electron microscopy (TEM) was used both to confirm the crystallinity of as-prepared particles and to gain insight into the chemical state of the particle surface as a function of time. TEM samples were collected on copper grids with lacy carbon mesh (Ted Pella Inc. model 01890) by placing the grids perpendicular to the aerosolized particle flow on either of a pare of copper electrodes. A DC bias was maintained between the electrodes in order to electrostatically collect samples. No auxiliary particle charging was necessary as the particles are naturally charged in the plasma synthesis. TEM data from 0 min, as with DRIFTS and XPS, represent the shortest amount of ambient exposure, but complete avoidance of ambient exposure was not possible. After initial imaging and data collection, the samples were stored in the same humidity control chamber described above. Electron energy loss spectroscopy (EELS) was performed on samples heated to 22, 400, 500, and 700 °C after 0 days, 1 week and 1 month of ambient exposure. Oxide standards were purchased from Sigma-Aldrich for SiO (powder, -325 mesh) and SiO_2 (nanopowder, 10-20 nm (TEM), 99.5% ttrace metals basis). SiO_2 was used as purchased by mixing a dilute solution of sample with methanol and placing one drop onto a TEM grid. The SiO was manually crushed to achieve smaller particle sizes prior to placement on the TEM grid. Special precaution was taken to clean the samples with a plasma cleaner (75% Ar/25% O_2) prior to imaging. An FEI F30 field emission transmission electron microscope set to 300 kV was used for imaging as well as EELS analysis. A dispersion of 0.3 eV and 1 mm entrance apperature

were used for EELS. EELS spectra were acquired at six spots on each sample followed by a power-law background subtraction. Each reported spectrum represents the sum of all six collected spectra having been calibrated to the Si peak at 99 eV and normalized, for clarity.

2.3 Results

2.3.1 The Pristine Silicon Nanoparticle

The hydrogen and deuterium surface coverage, as evidenced by FTIR peak intensities, was qualitatively monitored as a function of processing temperature. Data for deuterated particles is presented along with hydrogenated particles. Observations of deuterated samples are explicitly mentioned only where they differ significantly from the hydrogenated samples. Figure 3 shows the 2200 – 2000 cm^{-1} region from representative transmission FTIR spectra for hydrogenated particles heated to 22, 400, 500, and 700 °C, while Figure 4 shows corresponding DRIFTS spectra for these processing temperatures at four different intervals of ambient oxidation. Peaks near 2100 cm^{-1} are assigned as Si-H_x stretching modes by reference to the literature, including, Si-H_3 (2140 cm^{-1}), Si-H_2 (2113 cm^{-1}), and Si-H (2095 and 2080 cm^{-1}) (Marra, Edelberg et al. 1998). There is also a doublet centered near 875 cm^{-1} which is assigned to bend-wag deformation modes of Si-H_3 and Si-H_2 (Marra, Edelberg et al. 1998). While the deuterated counterpart to the doublet is not observed due to the low wavenumber limit of the detector, the corresponding Si-D_x stretching modes are observed near 1500 cm^{-1} and follow the same

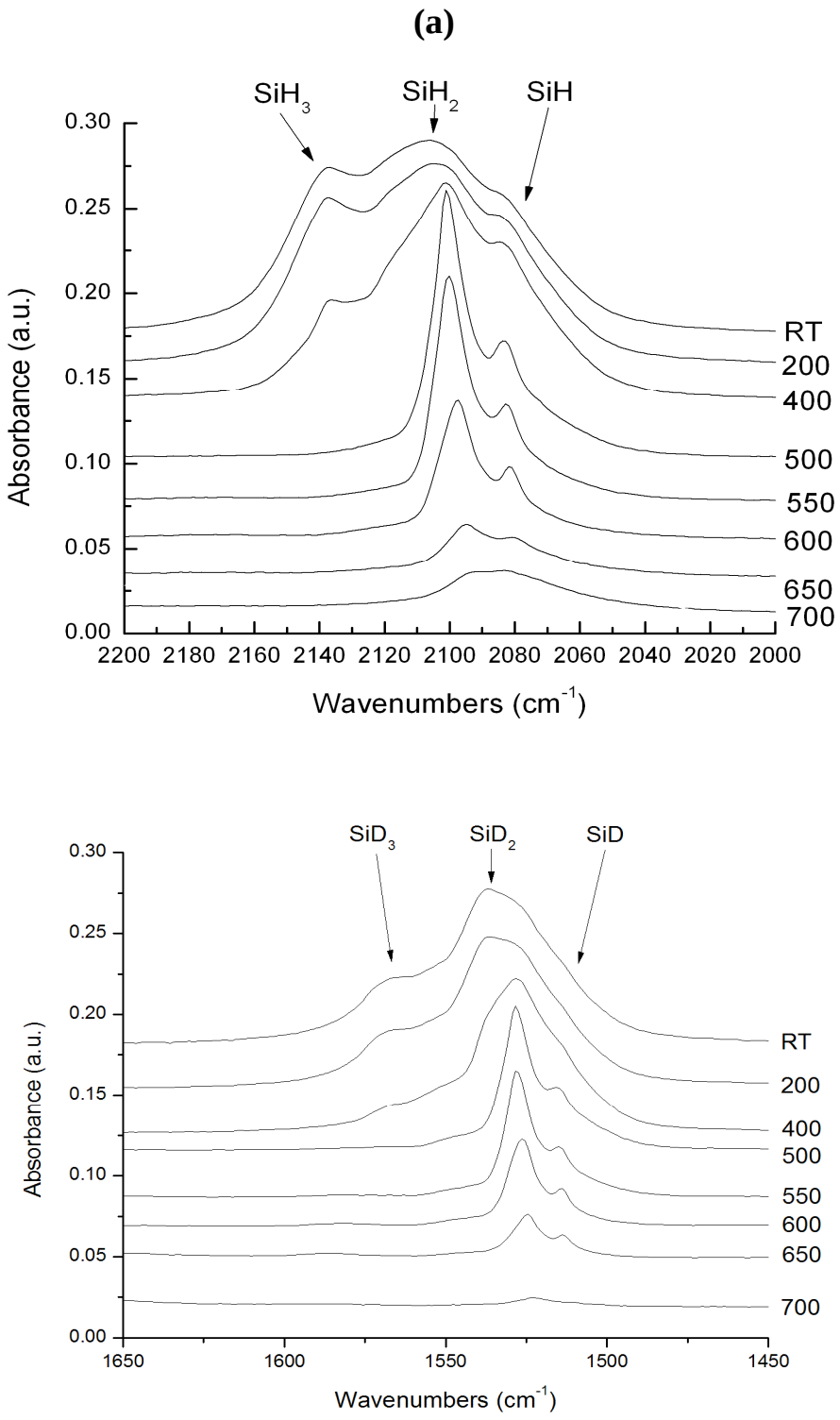

Figure 2.2: Transmission FTIR spectra of the Si-H_x (a) and Si-D_x (b) stretching region for silicon nanoparticles thermally processed at various temperatures (thermal processing temperature indicated in °C)

(Matsumoto, Belogorokhov et al. 2000). These particles were produced relatively free pattern with Si-D_3 (1556 cm^{-1}) at a higher wavenumber than Si-D_2 (1532 cm^{-1}), and Si-D (1519 and 1509 cm^{-1}) from contamination and with no evidence of oxidation. With no viewable peaks for the Si-D_2/Si-D_3 deformation modes, thermal desorption was monitored using the Si-H/D stretching modes alone.

2.3.2 Aerosol-Phase Thermal Treatment

Figure 3 shows the Si-H_x stretching region; peaks are labeled according to the set temperature of the furnace during processing. At room temperature, peaks for all three stretching modes are present; spectra are largely unchanged after heating to 200°C. Heating to 400°C, however, results in Si-H_3 and Si-H_2 features being significantly diminished in intensity. While spectra of deuterium-coated particles are not shown here, FTIR spectra suggest slightly more retention of surface hydride species at 400 °C. However, relatively small changes to the plasma conditions (i.e. changes to gas flow rate, plasma power, and pressure) have been shown to influence the particle surface species so this difference may not be significant. While others have assigned differing numbers of distinct vibrational modes, the existence of at least four modes is well supported by the complete loss of the bend-wag doublet (centered ~850 cm^{-1}), but retention of two peaks in the stretching region in the full spectra at 500 °C (Matsumoto, Belogorokhov et al. 2000; Marra, Kessels et al. 2003). The temperature range from 400 – 500 °C is of great interest since all Si-H_3 and Si-H_2 species are lost. As the processing temperature increases from 500°C the two sets of spectra continue to exhibit the same trend in peak shrinkage and narrowing until 700°C. At this point only a small signal remains for the

hydrogenated particles, this small amount of hydrogen that remains is continuously observed at temperatures up to 1100°C and is also observed in spectra for deuterated particles above 650 °C.

2.3.3 Native Oxidation

In-air, native oxidation of thermally processed particles was examined using DRIFTS. Quantitative chemical analysis was not possible. Particles were heated to 22, 400, 500 and 700°C and collected for DRIFTS analysis. Figure 4 shows spectra of silicon nanoparticles after storage in air for 0 minutes, 1 day, 1 week, and 1 month. As seen in thermal desorption (Figure 3) the Si-H_x modes centered at 2100 and 1500 cm^{-1} show decreasing intensity and narrowing at higher temperatures, which is in good agreement with the *in situ* desorption data. For both sets of spectra, there are several peaks not present in the H/D desorption spectra, one set at ~1050 cm^{-1}, which is assigned as the asymmetric transverse and longitudinal optical lattice phonon modes of the surface oxide layer (TO and LO of Si-O-Si). These peaks are well established (Chabal, Weldon et al. 2001) and appear in their most intense form in the 700°C spectrum where they are present within minutes of particle's exposure to ambient conditions. These are very weak immediately after particle production, but grow rapidly thereafter. There is also a peak at ~805 cm^{-1} for both H and D coated particles processed at 700°C. Due to the temperature dependence of this peak and its presence in both sets of spectra, it is attributed to oxide. In all ways except for the observed oxide peaks at 805 and 1050 cm^{-1} these spectra match those presented for thermal desorption.

(I)

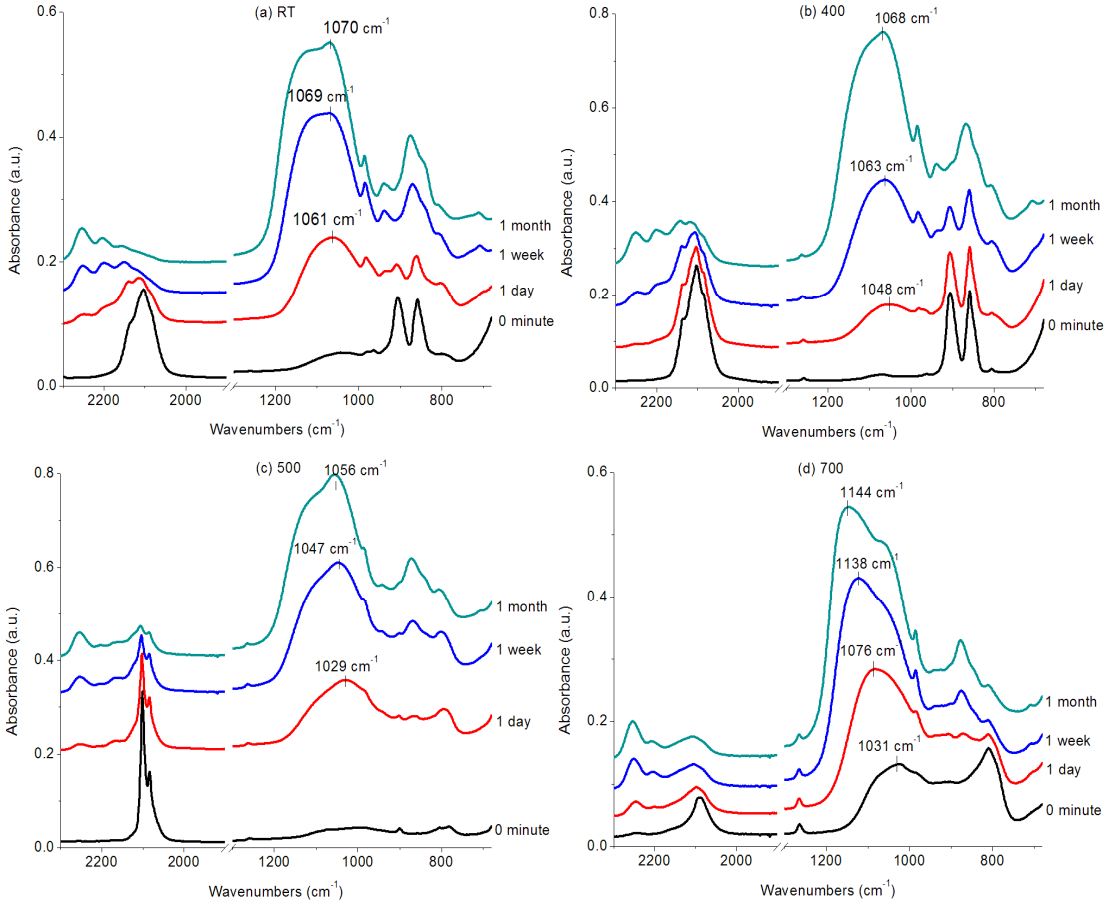

Figure 2.3: DRIFTS spectra of thermally treated hydrogen (I) and deuterium (II) terminated silicon nanoparticles at 4 time intervals of ambient oxidation (a) 22 °C, (b) 400 °C, (c) 500 °C, (d) 700 °C processing

(II)

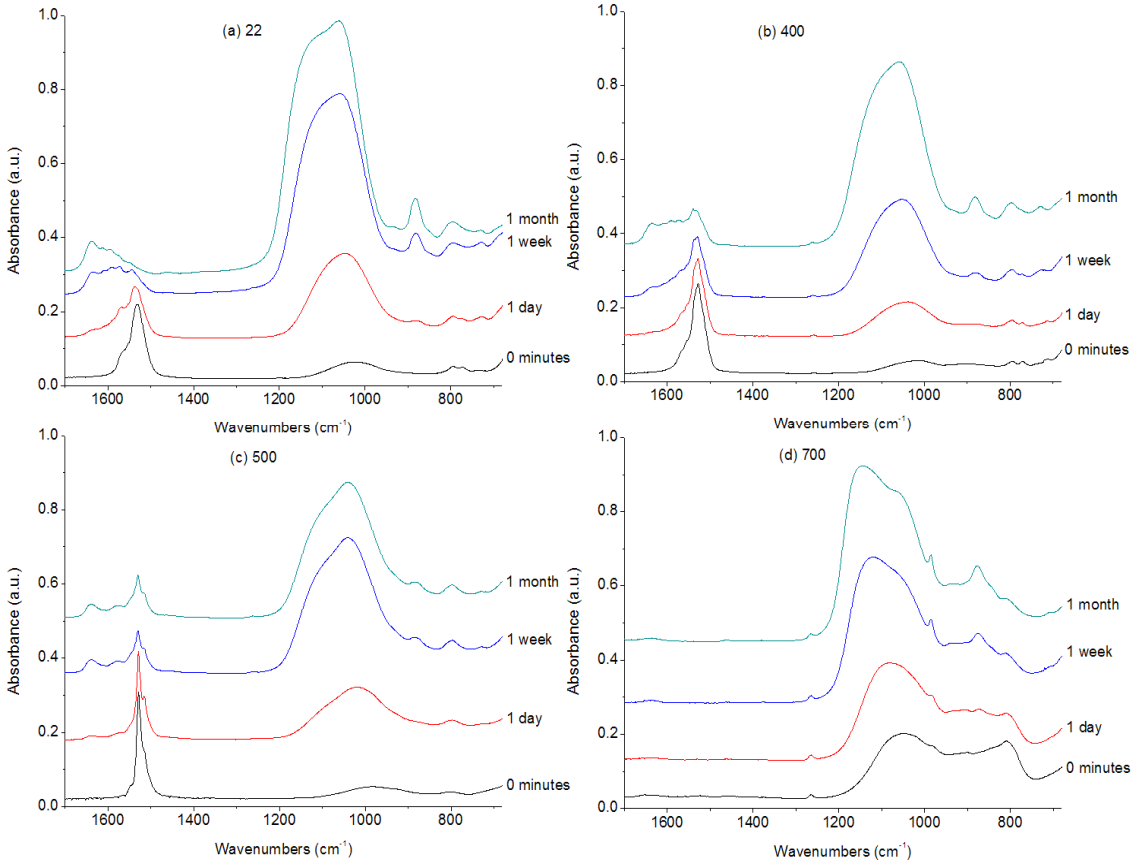

Figure 2.3: DRIFTS spectra of thermally treated hydrogen (I) and deuterium (II) terminated silicon nanoparticles at 4 time intervals of ambient oxidation (a) 22 °C, (b) 400 °C, (c) 500 °C, (d) 700 °C processing

No changes in the spectra are apparent after 1 hour of ambient exposure. After 1 day, however, there is significant growth in the asymmetric Si-O-Si modes at 1050 cm^{-1} in both sets of spectra, accompanied by a decrease in the H/D stretching amplitude and broadening to higher wavenumbers. This broadening is attributed to the formation of oxide. The following peaks are assigned $OSi-H_3$ (2150 cm^{-1}), O_2Si-H_2 (2200 cm^{-1}), O_3Si-H (2248 cm^{-1}), $OSi-D_3$ (1570 cm^{-1}), O_2Si-D_2 (1606 cm^{-1}), O_3Si-D (1641 cm^{-1}), all of which are stretching modes (Matsumoto, 2000). At lower processing temperatures (22, 400, and 500°C), the growth of these peaks begins most rapidly with $OSi-H_3/D_3$ due to the presence of a more complete H/D surface monolayer with higher order $Si-H_x/D_x$ more able to inhibit oxide formation. At 700°C, it begins with the O_3Si-H/D modes, as there are no $Si-H_2/D_2$ or $Si-H_3/D_3$ species on the surface. For the 700°C spectra there is also a difference in the TO-LO modes in that they not only grow more rapidly than for lower temperatures, but they also tend to higher wavenumbers indicating higher ordered, more complete oxide growth (Pai, Chao et al. 1986; Yi, Heitmann et al. 2003). A peak at 980 cm^{-1}, previously only barely detectable, becomes more prominent in all of the spectra of hydrogenated particles and the 700°C spectrum for deuterated particles. This peak is assigned as a Si-O-Si bending mode. In addition to these changes, the 22 °C spectrum in Figure 5 shows nearly a complete loss of both the bend-wag asymmetric doublet at 875 cm^{-1} and the Si-H/D stretching modes at 2100 and 1500 cm^{-1}. The 400°C spectrum, on the other hand, retains much of the original structure.

By 1 week, both sets of spectra show, at all temperatures, two new singlet peaks forming at 805 and 875 cm^{-1}. There is also further growth of the peak at 980 cm^{-1} for

hydrogenated particles at all temperatures, and for deuterated particles processed at 700°C. This feature remains indiscernible for deuterated particles processed at other temperatures. Additionally, the Si-H/D stretching modes for particles processed at 22 °C have diminished to the point that they are no longer distinguishable from the overlapping oxide peaks. For particles processed at 400 and 500 °C, however, these spectroscopic features are still prominent, making it appear that the particles oxidize more slowly. As for the $O_xSi\text{-}H_y/D_y$ oxide peaks, the lower order oxides that were stronger at earlier times are beginning to be eclipsed by higher order oxides. This is particularly true for particles processed at higher temperatures, where, as previously suggested, there are fewer H/D species on the surface to inhibit higher order oxide growth. The asymmetry in the TO-LO peaks observed 1 day after production has become more pronounced. Both sets of spectra show a general tendency for these peaks to grow and broaden. In most of the spectra these two peaks have also started to become individually distinguishable as evidenced by the minima found atop many of them. Tracking ν^{max} for each of these peaks on Figure 4 they have been consistently migrating toward higher wavenumbers indicating higher ordered oxides (Pai, Chao et al. 1986).

After 1 month, the TO-LO peak minima are more pronounced and the peaks have migrated further to higher wavenumbers. The Si-H asymmetric doublet at 875 cm^{-1} has diminished completely in all spectra including the 400°C spectra. While the high order oxide $O_3Si\text{-}H/D$ peak has become the most prominent for virtually all spectra, the $Si\text{-}H_x/D_x$ stretching modes are still visible in the 400 and 500°C spectra. The 22 °C spectrum, on the other hand, shows no sign of these once prominent peaks.

XPS analysis of thermally treated particles was performed. Although XPS is thought of as surface sensitive, nanoparticles are so small, core-shell chemistries are not differentiated. Figure 4 shows the percent silicon oxide (Si-Ox) from the high-resolution spectra of the Si 2p peaks at 0 days (squares), 1 week (circles), and 1 month (triangles). Immediately after particle production there is very little oxide present (< 15% in all samples). Both transmission *in situ* FTIR and DRIFTS support this general finding. While the samples processed at lower temperatures show greater degrees of silicon oxidation, this may be due to annealing that occurs in the furnace at higher temperatures, effectively cleaning the as-produced particle surface. After 1 week of ambient exposure, however, there can be no doubt that 700 °C thermal processing resulted in the smallest amount of oxygen incorporation. While both 22 and 400 °C processing appear to have oxidized equally, it is clear that higher processing temperatures have resulted in less oxidation. This same general trend remains clear after 1 month of oxidation. In fact, not only do the 700 °C particles oxidize most slowly, they almost cease oxidizing after 1 week.

Figure 5a shows a representative transmission electron micrograph of particles that have been thermally treated at 700 °C. Lattice fringes consistent with crystalline silicon are visible. While processing at 22 °C did not require thermal treatment, the crystalline core and circular particle shape are observed in all samples. Interestingly, there appears to be a core-shell structure for these particles. This has been observed

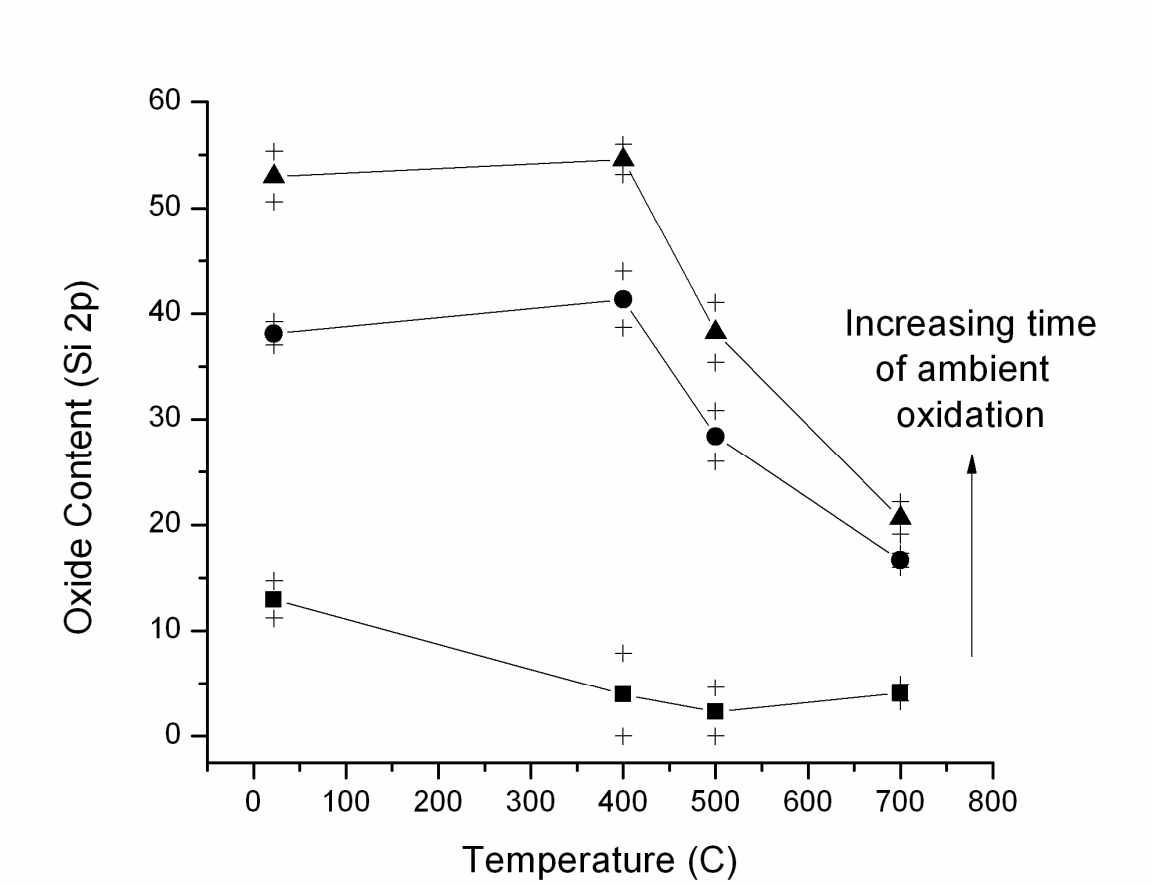

Figure 2.4: XPS data for the oxide content of the Si2p peak for four thermal processing temperatures after 0 days (squares), 1 week (circles), and 1month (triangles) ambient air exposure (oxide content reported as percent of total Si2p peak integration, statistical error indicated with +)

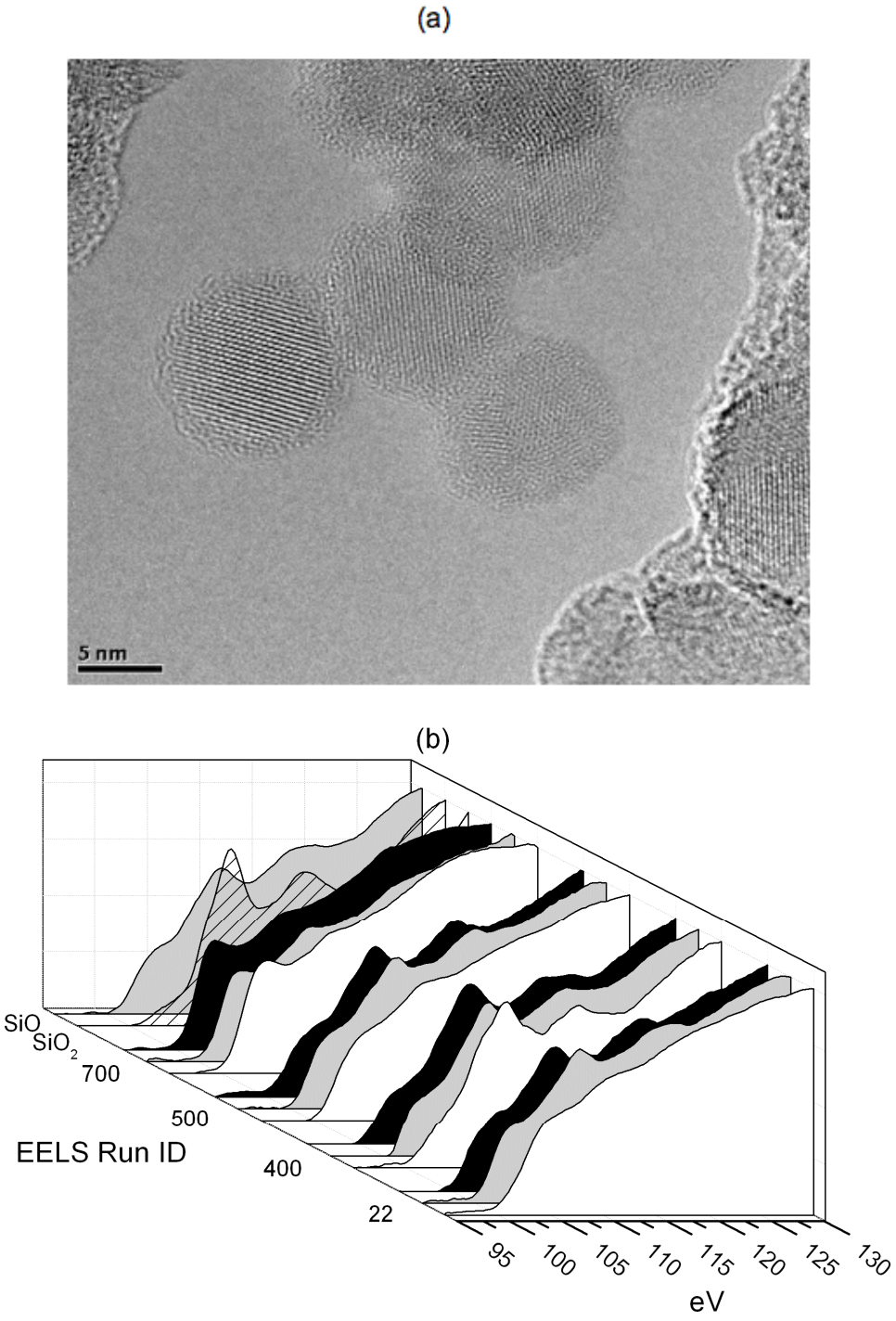

Figure 2.5: (a) Transmission electron micrograph of silicon nanoparticles thermally processed at 700 °C immediately after collection. (b) EELS spectra for silicon nanoparticles having been exposed to ambient conditions for 0 days (white), 1 week (grey), and 1 month (black) after thermal processing at 22, 400, 500, and 700 °C (processing temperatures indicated on plot). Oxide standards also included as indicated

previously (Holm and Roberts 2009) and is thought to be amorphous silicon with a thickness of ~0.5 nm on an 11 nm particle. The amorphous shell represents 25% of the particle volume. The XPS data in Figure 4 shows that particles processed at 700 °C oxidize to ~20% after 1 month ambient exposure which represents less than the amorphous shell thickness. TEM was further used to elucidate information about the surface oxide. EELS was performed on particles over 1 month, and those data are shown in Figure 5b. While EELS is able to give a great deal of in-depth chemical information about thin films and powders, the small sizes of these particles made the analysis more vulnerable to sample drift. Consequently, all EELS data presented represent bulk properties of the samples rather than offering information specifically about any oxide shell. Oxide standards were run with minimal ambient exposure and are shown in Figure 5b. There are two primary differences between the two standards. First, the presence of two peaks for SiO_2 at ~110 and 117 eV is much stronger than for SiO. The growth of these peaks appears to indicate higher order oxides. Second, the peak edge at 99 eV begins to shift as the oxide develops, leaving a shoulder for sub-stoicheometric oxides and latent peak onset for fully developed oxides (Schulmeister and Mader 2003) Both of these features are observed in the sample spectra. Particles processed at 22, 400, and 500 °C show growth of the oxide peaks over time and the development of a small shoulder at lower binding energies without developing latent peak onset. Both of these features suggest the formation of sub-stoicheometric oxide on these samples. The 700 °C spectra, on the other hand, do not exhibit these peaks in great quantities even after 1 month of

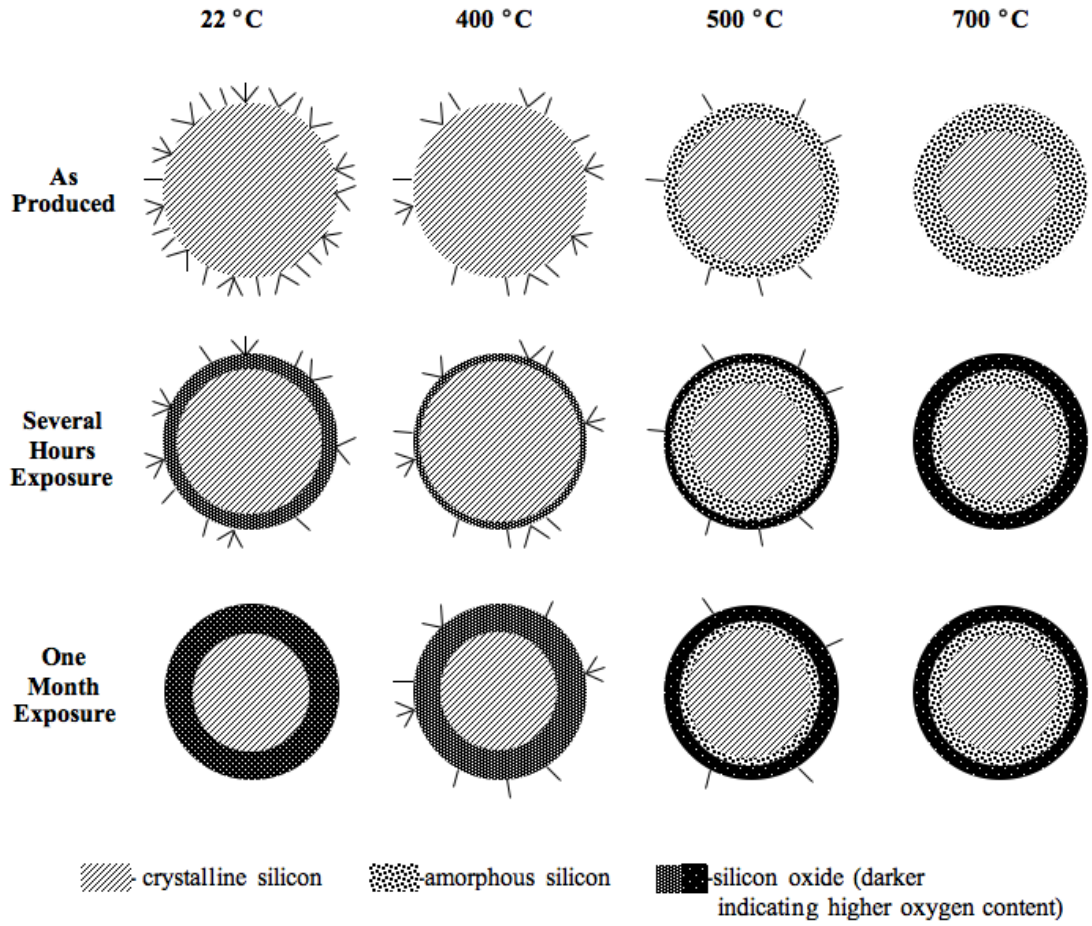

Figure 2.6: Schematic illustration of silicon nanoparticles having been thermally treated at 22, 400, 500, and 700 °C after 0 minutes, 1 day, and 1 month ambient exposure (surface hydride species shown as sticks)

ambient exposure. Futhermore, there is a small peak at ~103 eV, rather than a shoulder, which is consistent with crystalline silicon (Schulmeister and Mader 2003).

2.4 Discussion

Pristine particles have a crystalline silicon core with very few internal point defects, along with a compact surface monolayer of hydrogen or deuterium (Holm and Roberts 2009). Transmission FTIR has shown that thermal processing of small Si-nps (ca. 11 nm) results in varying surface coverages of hydrogen. Figure 6 shows an illustrated representation of the particles after they have been thermally processed at, (a) 22 °C, (b) 400 °C, (c) 500 °C, and (d) 700 °C. It also includes illustrations of these particles after 1 week and 1 month of ambient exposure. Without any thermal processing, the surface is covered with a nearly complete monolayer of mono, di, and trihydride species (Holm and Roberts 2007). This, in conjunction with surfaces that contain very few clean crystal facets (Dabrowski and Mussig 2000), results in a surface chemistry that is likely not very stable (Hawa and Zachariah 2004). When the particles are heated, the instability of their surfaces results in desorption of the di and trihydride species which is likely accompanied by an annealing process through which the particle's surface atoms rearrange into lower energy configurations (Ogata, Yoshimi et al. 2001) and become amorphous. The desorption and annealing process results in particles that have more stable surface structure. As the processing temperature increases, the more stable monohydride species eventually desorb, leaving bare silicon. This bare silicon surface likely contains both strained back bonds and unsatisfied

dangling bonds due to the inability of the surface atoms to completely sp^3 hybridize, making the surface largely amorphous (Holm and Roberts 2009). The high energy nature of this surface chemistry leaves the particles unprotected from chemical attack.

In general, three regimes for oxidation of thermally processed particles are identified. The first regime is particles that have not been thermally treated, leaving large amounts of all three hydride species on the crystalline silicon surface. Second, particles that have been processed at intermediate temperatures (~400 °C) resulting in partial desorption of the surface hydrides, but leaving varying fractions of each on the surface. Lastly, particles that have been processed at temperatures high enough to desorb all higher order hydrides and some or all of the monohydride surface species (≥ 500 °C).

While simple analysis of the peak structure from the DRIFTS spectra does give a great deal of information about the surface oxide environment (ie. 22 and 700 °C processing results in more complete stoicheometric oxides), peak area analysis can give even greater insight. Figure 7 shows the normalized peak area ratios for the Si-H_x stretching and TO-LO modes. These ratios were calculated as follows:

$$F_{Si-Ox} = A_{TO-LO} / \left(A_{TO-LO} + A_{Si-Hx} \right)$$

Where A_{TO-LO} and A_{Si-Hx} are the measured peak areas of the silicon oxide TO-LO and Si-H_x stretching modes respectively and F_{Si-Ox} is the normalized fractional oxide content. While F_{Si-Ox} is not a true measure of oxide content, it has been used as a rough measure for the purpose of analysis. Interestingly, this analysis suggests that intermediate surface hydrogen coverage is best able to passivate a particle toward oxidation. Indeed, 400 °C processing not only initially oxidizes more slowly than any other sample, it also does not

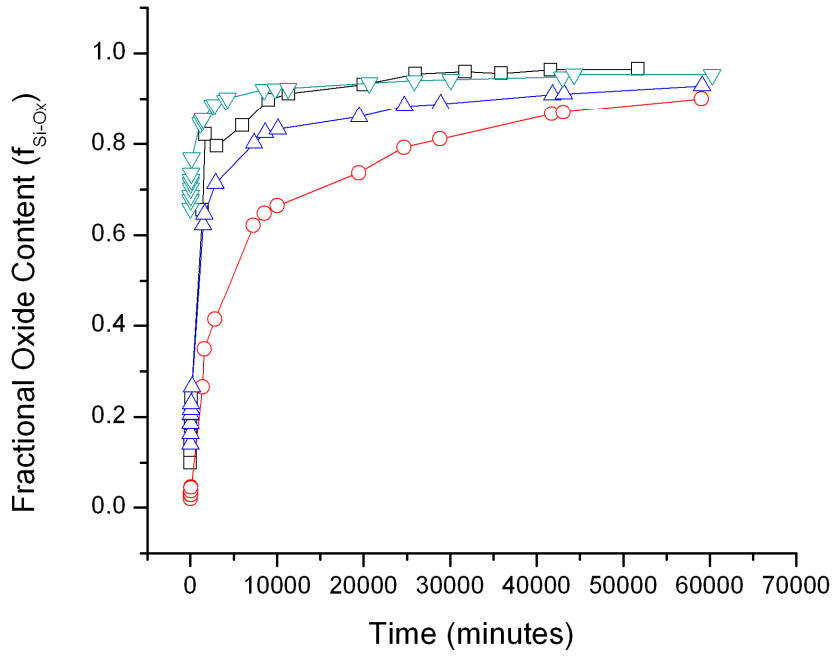

Figure 2.7: Fractional oxide content of Si-nps processed at various temperatures (22 °C (squares), 400 °C (circles), 500 °C (triangles), 700 °C (diamonds)) as indicated by the normalized DRIFTS peak area ratios

reach the same degree of oxidation after ~6 weeks of exposure (60000 minutes), converting only 90%. Additionally, both 22 and 700 °C processing seem to yield the

same results based on DRIFTS analysis in that they both oxidize quickly at first, reaching 90% conversion after only 1 week of exposure.

There are likely several factors influencing the native oxidation rates of these particles. One is surface hydrogen coverage. The nature of the surface hydrogen coverage likely influences the oxidation of these particles in complex ways. While it has been shown that hydrogen passivates bulk silicon, the DRIFTS data reported here suggest there may not be a simple relationship on a nanoparticle surface. More hydrogen coverage does not result in better passivation. The surface rearrangement at intermediate coverage likely reduces the energy of both the bonding configurations and steric interference thus reducing the oxidation rate. This effect is offset at higher temperatures by the loss of hydrogen, leaving highly reactive unsatisfied bonds. Apparently, 400 °C processing results in an optimum coverage/surface energy balance. The surface hydrogen may also influence the ability of the oxide to form well-ordered crystalline regions. Higher hydrogen coverage would likely result in smaller and less ordered oxide regions on the surface.

The silicon-hydrogen/air interface likely influences oxidation as well. Without thermal processing the interface is hydrogen terminated crystalline silicon. While this pristine surface contains many irregularities, as the temperature increases desorption-recombination mechanisms serve to convert the surface into amorphous silicon resulting in as-produced particles with distinctly different surface chemistries (Holm and Roberts 2009). Without consideration for the surface hydrogen, there should be a gradual shift, as processing temperature increases, from crystalline silicon to amorphous silicon. If the

relative properties of crystalline vs. amorphous silicon remain the same for nanoparticles as for bulk materials, then higher temperatures leading to more amorphous surfaces should result in slower oxidation. Qualitatively, this is reasonable. Unsatisfied bonds resulting from hydrogen desorption, if forced to exist in a perfect crystalline system, would be left as dangling bonds or highly strained back bonds on the surface. If the surface is able to reconfigure, however, it could begin to form an amorphous layer that would reduce the number and energy of these unsatisfied bonds. This could, in conjunction with the optimization of surface hydrogen coverage result in particles that oxidize more slowly. Figure 7 supports this analysis for particles processed at 400 °C (circles) showing that they have oxidized the least of any particles out to 2 months of exposure.

There are at least two other combinations of these factors that are exhibited here. At 22 °C, no surface hydrogen has desorbed and the interface, while irregular, remains crystalline. While the greater than optimum hydrogen coverage may passivate the surface in relation to bare crystalline silicon, the crystalline silicon core would presumably oxidize more quickly than an amorphous shell. Furthermore, the presence of the surface hydrogen may cause the oxide to form a less dense amorphous layer. At 700 °C, the bare nanoparticle surface offers no passivation from ambient exposure, but the amorphous shell should oxidize more slowly than a bare crystalline one and with no surface hydrogen, the oxide could form a more highly ordered complete layer.

Finally, changes in the particle's surface area would change oxidation behavior. Less surface area should result in slower oxidation. Thermal treatment of these particles

has been shown to result in sintering, causing decreased surface areas within the temperature range in question (700 °C) (Holm and Roberts 2009). The decreased degree of oxidation for particles processed at 700 °C could be caused, in part, by the decreased surface area of these particles.

We conclude, therefore, that it is a combination of the hydride monolayer and its specific composition along with the crystallinity or amorphisity of the particle surface that results in a given particle's propensity to oxidize. We also suggest that the DRIFTS, XPS, and EELS data reveal less about the actual oxidation rate and more about the nature of the oxide that is formed. Particles having been processed at 700 °C will develop a shell of high ordered oxide limiting further oxidation after a relatively short amount of time (1 month). This shell may or may not contain some sub-oxide silicon, but the spectroscopic analysis presented herein clearly establishes the presence of a more complete, more stoicheometric oxide for particles processed at 700 °C. All other particles, on the other hand, exhibit significant oxidation out to one month and form sub-stoicheometric oxide shells that offer little passivation from further oxidation. Furthermore, when a surface is covered with a well ordered, low energy hydride it will oxidize less than if the monolayer consists of higher order hydrides (di or tri). It is suggested that this surface configuration results in fewer dangling bonds and crystal edge sites on the surface resulting in a less chemically reactive surface chemistry. Additionally, an amorphous surface will oxidize more slowly than a crystalline one. While the loss of surface hydrides at higher processing temperatures results in greater

silicon exposure to native oxidants, this effect is at least partially offset by the formation of an amorphous silicon shell.

2.5 Conclusion

We have shown that, in regards to the thermal treatment of hydrogenated and deuterated silicon nanoparticles, their behavior, as exhibited through FTIR analysis and XPS, they are virtually identical. Both types of particles are formed, in their pristine state, with a large number of mono, di and tri-hydride/deuteride species on their surface. When the particles are heated in the aerosol phase, they begin to loose higher order hydrides/deuterides around 200°C being left with a compact monolayer of mono-hydride/deuteride at 500°C. With additional heating, the remaining hydride/deuteride species are lost by 700°C leaving a bare amorphous silicon surface. When particles from each of these temperatures are allowed to oxidize under ambient conditions, their oxidation rates and behaviors are not the same. Namely, particles processed at intermediate temperatures (400 and 500 °C), retain more surface hydride species than unprocessed particles after 1 month of ambient exposure. All of these particles, (22, 400, and 500 °C) oxidize quickly forming substoicheometric oxide shells while particles processed at 700 °C oxidize very quickly at first, but form a well ordered self-limiting stoicheometric oxide shell. This shell significantly slows oxidation after only 1 week ambient exposure.

Chapter 3

Nanostructural Changes to Thermally Oxidized Natural Gas Soot

Raman microscopy, differential scanning calorimetry – thermogravimetric analysis, Fourier transform infrared spectroscopy and transmission electron microscopy were used to investigate changes to soot upon aerosol phase thermal processing. Three primary conditions, each being either oxidative or non-oxidative, were examined at temperatures in the range 22 – 1100 °C. The graphene crystallite length and changes thereof were examined as a function of oxygen partial pressure and temperature of aerosol phase processing. Additionally, changes to the contained organic functionalities were monitored with respect to the experimental factors. Data shows strong evidence to support changes in crystallite length at or below 800 °C furnace temperature with a complex relationship to the production pressure and furnace temperature. At lower temperatures desorption or combustion of small organic byproducts is likely.

3.1 Introduction

Soot particles are very complex (Cachier 1998). Their size, shape, morphology, and composition can vary widely depending on their specific production conditions. Once produced and emitted into the atmosphere, they are pollutants having complex influences on health (Pukkala, Martinsen et al. 2009; Spira-Cohen, Chen et al. 2011) and climate (Jacobson 2010). Being composed of various small crystallites of polycyclic aromatic hydrocarbons (PAH) they are naturally hydrophobic (Schrader 1975; Chen, Hung et al. 1993), but soon after being emitted into the atmosphere, they are known to act as primary sources for cloud condensation nuclei (CCN) (Ackerman, Toon et al. 2000; Gysel, Nyeki et al. 2003). Water vapor in the upper portions of the atmosphere condenses onto nascent soot particles forming cloud droplets (Kuhn, Petzold et al. 1998). The specific mechanism of this process is unclear.

It has been suggested that the efficacy of soot particles to act as CCN is dependant on the specific chemistries present on their surfaces (Gysel, Nyeki et al. 2003; Popovicheva, Persiantseva et al. 2008). Additionally, the aging process through which hydrophobic soot particles become more hydrophilic is a critical aspect of their CCN activity. Water vapor condensation is thought to begin with very small seed sites (Dubinin 1980; Gregg and Sing 1982; Persiantseva, Popovicheva et al. 2004). These sites may be inherently more hydrophilic than the bulk PAH framework of the soot particles. On the other hand, chemical aging of the soot within the atmosphere may change the specific chemistries present on soot particles (Harrison and Pio 1983; Chughtai, Williams et al. 1999; Zuberi, Johnson et al. 2005). Nonetheless, the adsorption

of inorganic salts or oxidizing species or the loss of hydrophilic organic compounds can increase the hydrophilicity of the soot surface. It is certain that atmospheric soot particles are exposed to all or some of these conditions (Nienow and Roberts 2006).

The degree to which the soot surface chemistries can be modified is dependent on the specific chemistries and morphologies of the graphene crystallites contained within them. For example, large graphene crystallites with very few defects or functionalities present should resist chemical changes thus making them less likely to act as CCN through chemical aging. Soot particles made of small crystallites with an abundance of edge sites and many defects or functionalities, however, could be modified through an aging process making them more susceptible to changes in hydrophilicity. If the aging process involves adsorption of inorganic salts or VOCs rather than changes to the particle chemistries, new and different factors would control the aging process. Whatever the case, a clear understanding of graphene crystallite size and chemistries for various soots would certainly help develop a more complete model for CCN activity. Furthermore, developing an understanding of the synthesis factors influencing soot particle size, shape, morphology, and composition would be invaluable. Indeed, much research has focused on this topic leading to new insights including fuel dependant chemical signatures and temperature dependant morphologies (Wal and Tomasek 2004; Cain, Gassman et al. 2010). Once soot particles have been produced, however, what can be done to change their future health and climate effects? From a practical sense, are their any changes that can be made to exhaust handling systems that would influence future activities of already-generated soot particles?

The present study seeks to use post-synthesis aerosol-phase heating to change the crystallite size and chemistries of natural gas soots. While the temperature at which soot particles are made has been shown to affect graphene crystallite size (Wal and Tomasek 2004), whether this can be done post-synthesis remains to be shown conclusively. Additionally, with typical temperatures in a soot-producing flame around 1200 °C, there may be measurable changes to soot structure or composition at lower temperatures. Raman spectroscopy along with differential scanning calorimetry – thermo-gravimetric analysis (DSC-TGA), Fourier transform infrared (FTIR) spectroscopy, and transmission electron microscopy (TEM) will be used to explore the effects of post-synthesis aerosol-phase heating on soot nano-structure.

3.2 Experimental

3.2.1 Experimental Setup

Soot particles were made using a diffusion burner running ~500 sccm natural gas with a concentric sheath flow of low humidity air (typically ~3% relative humidity). Figure 1 shows a diagram schematic of the soot production system that was used. Particles were immediately pulled through a 1 mm orifice into ½ inch outer diameter quartz tubing, producing a small "flame jet" within the quartz tube. The aerosol stream was maintained just below atmospheric pressure at 620, 660, or 680 Torr. The pressure differential at the orifice was varied depending on the desired oxygen partial pressure of the aerosol flow with values from 0 – 1.7% O_2 being achieved in between pressures of 620 and 660 Torr respectively. The temperature of the flame jet within the quartz tube

was monitored. Table 1 is a summary of the three production conditions. Immediately downstream of the orifice, the humid aerosol flow was dried using an 18 inch copper "Y" condenser with circulating water held at 0 °C. The percent gaseous oxygen in the aerosol stream, from 0 – 100%, was monitored down stream of the condenser. A tube furnace (Linberg-Blue model: HTF55122A) capable of temperatures from room temperature to 1200 °C with a 2 inch o.d. quartz tube was used for thermal processing followed by a 24 inch vertical copper condenser for additional drying. The percent gaseous oxygen was monitored both up and downstream of the tube furnace and Figure 2a shows the downstream values for all three collection pressures at each furnace temperature. For all operating conditions below 600 °C, oxygen was not consumed in the tube furnace, and for all conditions at or above 600 °C, nearly all of the oxygen was consumed. The lower oxygen levels reported in Figure 2 compared to Table 1 were observed occasionally when the aerosol tubes became over laden with diffused soot, these conditions were typically avoided. Nearly all soot collection conditions produce the same mass of soot per minute with the notable exception of 680 Torr with furnace heating to 1100 °C. These collection conditions produced 5-10 times more mass per minute (Figure 2b). Collection efficiency is not thought to play a role in this observation due to the highly fractal nature of these soot particles and their agglomerate size. The particles were then collected for various analysis techniques using either impaction onto quartz filter media or electrostatic collection onto transmission electron microscope grids.

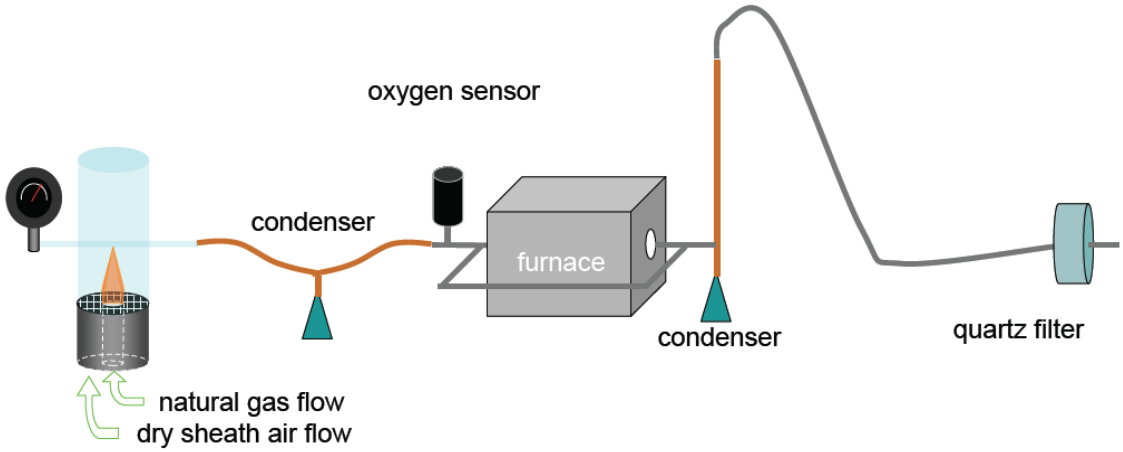

Figure 3.1: Schematic diagram of soot particle synthesis, post synthesis thermal oxidation, and collection setup

Table 3.1: Summary of soot production conditions

Pressure (Torr)	% gaseous oxygen	Flame jet temperature (°C)
620	0	1250
660	1.5	1150
680	1	1140

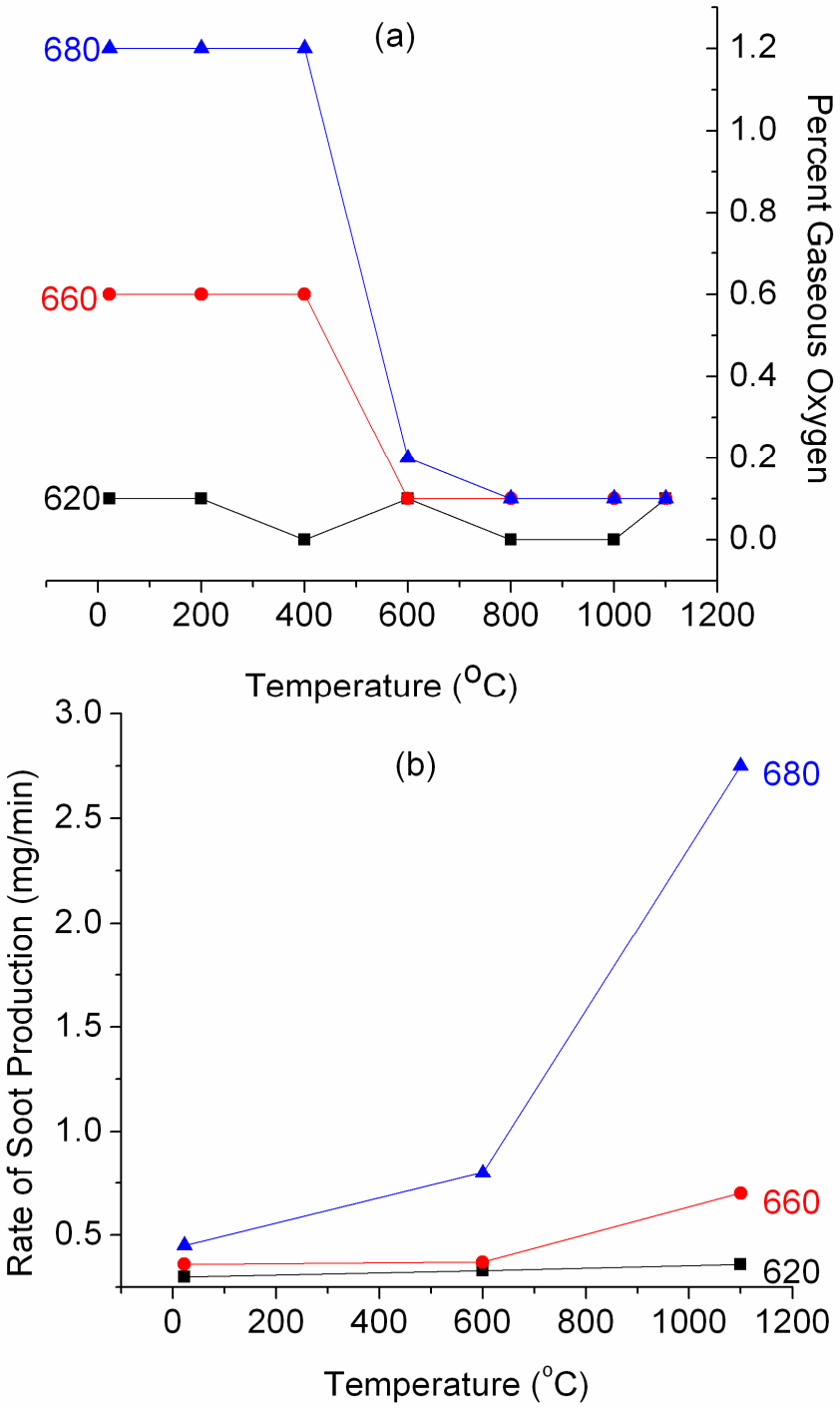

Figure 3.2: (a) percent gaseous oxygen in the aerosol phase down stream of the tube furnace at three collection pressures (collections pressure indicated), (b) rate of soot production for three collection pressures and three tube furnace temperatures (mg/min)

3.2.2 Raman Spectroscopy

For Raman spectroscopy, Fourier transform infra-red spectroscopy (FTIR), and differential scanning calorimetry – thermo-gravametric analysis (DSC-TGA), the samples were collected on quartz filter media (PALL Tisuquartz model 7202) placed through the aerosol flow. The samples were then placed for at least 18 hours in a vacuum desiccator maintained at 60 °C allowing small organic compounds that had adsorbed to the particles to be pumped away before analysis. Approximately 14 % mass loss was recorded for all samples after being stored in the vacuum desiccator. Samples for Raman were collected for 10 minutes and analyzed on the quartz filters while DSC-TGA and FTIR samples were collected for 45 minutes and then scraped from the quartz filter for analysis. Raman spectroscopy was performed using a laser tuned to 532 nm at 500 mW (Model info) with optics to control the laser power and spot size to ~1-3 mW and 1 mm respectively. Samples were held flat on a steel support mounted to an adjustable stage, which was used for sample manipulation. Ten spectra were collected in a straight line approximately 2 cm long on each sample and these spectra were later processed in one of two ways. Baselines were set to zero for all samples, then either the D and G carbon bands were fit with two Lorentzian peaks and a ratio (I_D/I_G) was calculated or the FWHM of the D1 peak was directly measured and averaged over all ten spectra. Both fitting methods produced results with good agreement, but the method that best fit the data will be represented for each set of collection conditions for reasons that will be discussed later.

3.2.3 Differential Scanning Calorimetry – Thermo-gravimetric Analysis

DSC-TGA was performed on samples having been collected on a single quartz filter for 45 minutes and then stored in the vacuum desiccator for 18 hours. The soot particles were manually scraped from the filter media and scooped into the Al_2O_3 crucible for analysis. The ramp rate was set to 10 °C/min from room temperature to 1100 °C and air was used as the purge gas at a flow rate of 20 mL/min. Approximately 3 mg of soot was used for each curve, but small variations in sample mass result in reporting the TGA data as % mass loss rather than actual mass loss.

3.2.4 Fourier Transform Infrared Spectroscopy

Samples for FTIR analysis were collected on the same tissue quartz filters used for Raman and DSC-TGA followed by drying for 18 hours in a heated vacuum desiccator. A small amount of sample was then scraped from the filter and manually crushed with dry KBr to form a fine powder. The resultant powder was pressed to form pellets for transmission mode FTIR spectroscopic analysis. A unique background was taken for each sample after the sample chamber had been purged with dry air for at least 30 minutes. The unprocessed spectra were then automatically baseline subtracted using the spectroscopic collection software, these spectra are reported here without further processing.

3.2.5 Transmission Electron Microscopy

Soot samples for transmission electron microscopy (TEM) were collected onto copper grids with lacy carbon support. An home-built electrostatic collector was used for sample collection and was set to 300 V for a collection time of seven seconds. Imaging

was performed on a Tecnai 120 kV microscope at magnifications above 200x with a typical spot size of 3. Images were analyzed visually and without further processing for differences in the size of the grapheme crystallites

3.3 Results

3.3.1 Raman Spectroscopy

The graphene crystallite size within various natural gas soot particles was monitored as a function of aerosol stream pressure, flame-jet temperature, percent gaseous oxygen, and aerosol-phase thermal processing temperature. Raman spectroscopy was performed on all samples having been first stored at 60 °C in a vacuum desiccator for at least 18 hours. Figure 3 shows representative Raman spectra for soot samples collected at various aerosol system pressures for a wide range of tube furnace temperatures (furnace temperatures indicated). In general, there are two primary peaks present on all Raman spectra and these are assigned as the disorder (~1350 cm^{-1})(D band) and graphite (~1590 cm^{-1})(G band) band of carbon(Dippel, Jander et al. 1999; Sadezky, Muckenhuber et al. 2005; Soewono and Rogak 2009). While these peaks have been generally assigned to the D and G bands of carbon, there are more discrete modes which contribute to their primary structure, the particular identities and fitting of these modes will be discusses in greater detail later. Figure 3a shows spectra of soot samples collected at 620 Torr (the lowest operating pressure) from room temperature to 1100 °C furnace temperature and there is little or no observable change in the spectra with increasing furnace temperature. Figure 3b shows spectra of soot samples collected at 660 Torr for

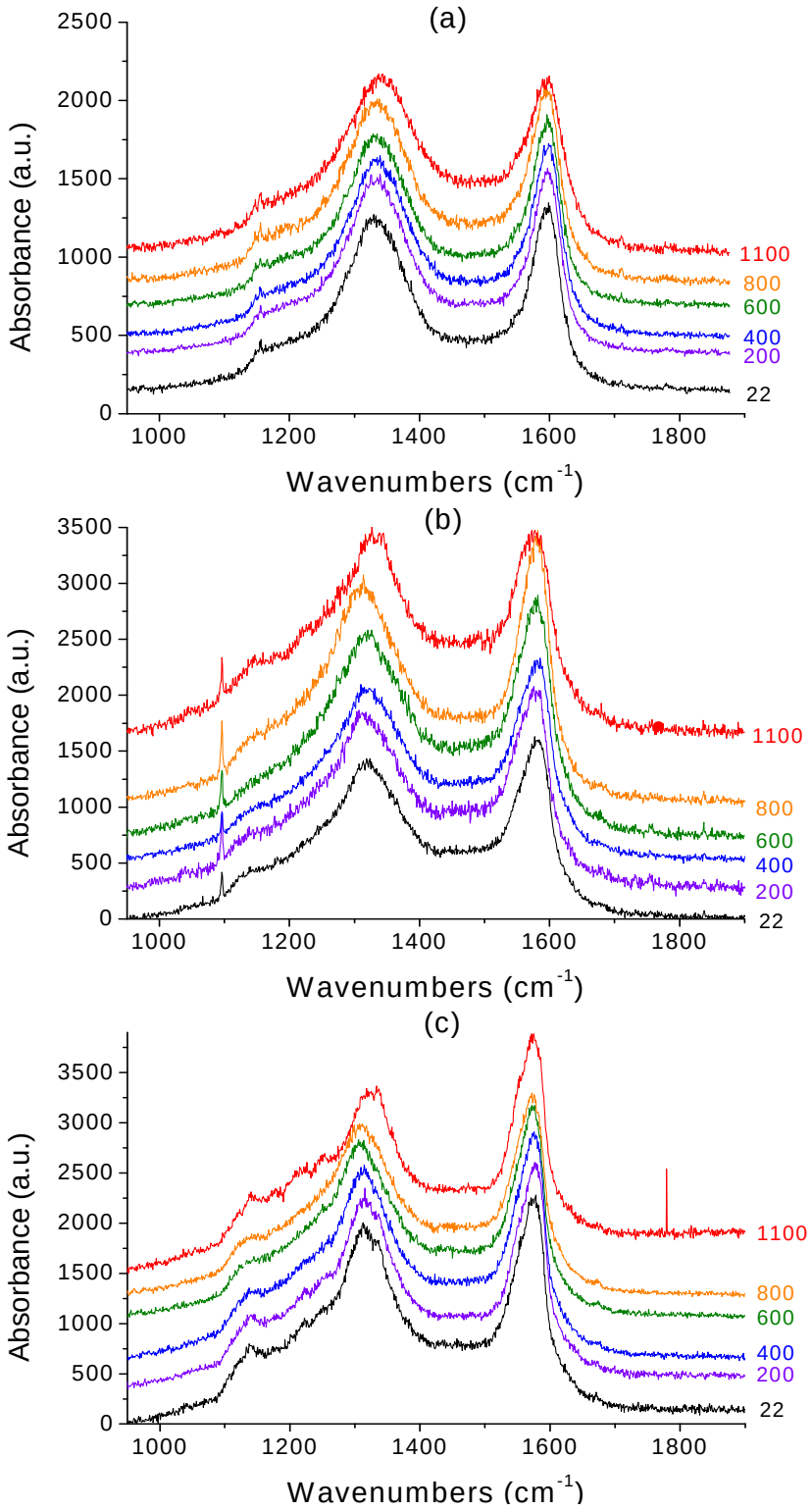

Figure 3.3: Representative Raman spectra for (a) 620 Torr, (b) 660 Torr, and (c) 680 Torr collection pressure. Thermal after-treatment temperature indicated

the same furnace temperatures as Figure 3a. A small change in the peak shape is apparent for 1100 °C furnace temperature; the D band has begun to narrow very slightly and has shifted to higher wavenumbers. Additionally, the narrowing of this band may have resulted in new peaks emerging from 1200 – 1300 cm^{-1}, but these peaks lack real definition. Comparing Figure 3c with 3 a & b, it is apparent that more peak narrowing has occurred for the D band at 1350 cm^{-1} and the emergence of new peaks is supported best for 1100 °C furnace temperature where these peaks are most intense.

Due to the subtle changes in peak structure and intensity present in the Raman spectra, curve fitting was performed on each spectrum using either a two-peak method (Soewono and Rogak 2009) or a five-peak method (Sadezky, Muckenhuber et al. 2005). These peak fitting methods were developed separately, but have been shown to provide relatively equivalent indicators of the grapheme crystallite size. Sadezky, *et al.*,(2005) have examined roughly a dozen different soot or soot surrogates using X-ray diffraction and Raman spectroscopy. Their study has resulted in a more complete identification of first-order Raman peaks. They were able to fit the Raman spectra collected from all samples with four Lorentzian and one Gaussian peak without restricting peak parameters. These peaks were subsequently assigned broad characteristics arising from previously described modes(Figure 4c): G, ideal graphite lattice E_{2g}-symmetry (Tuinstra and Koenig 1970); D1, graphene layer edges A_{1g}-symmetry (Tuinstra and Koenig 1970); D2, surface graphene layers E_{2g}-symmetry (Wang, Alsmeyer et al. 1990); D3, amorphous carbon (Jawhari, Roid et al. 1995); D4, disordered graphitic lattice A_{1g}-symmetry (Al-Jishi, Elman et al. 1982). One of the primary findings of their work was the relation of the D1

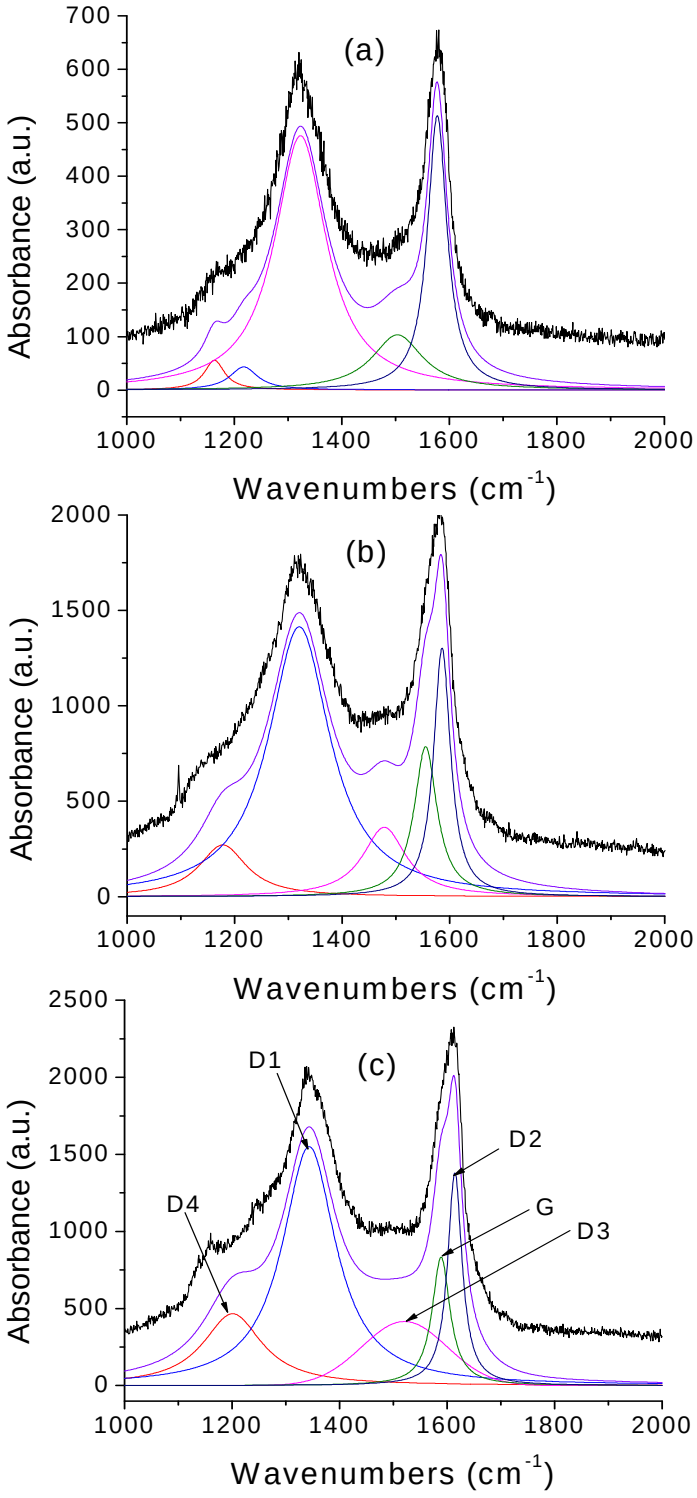

Figure 3.4: Five peak fitting performed on representative Raman spectra from samples collected at (a) 620 Torr, (b) 660 Torr, and (c) 680 Torr (raw data shifted for clarity)

peak FWHM to the relative graphene crystallite size. Figure 4 shows a representative Raman spectrum from each of the production pressures collected without thermal processing, five-peak fitting is shown. For samples produced at 660 and 680 Torr (Figure 4 b and c), the peak parameters are in good agreement with Sadezky *et. al*. for nearly all samples collected. The D1 peak narrows from with increasing pressure, a possible indictor that the graphene crystallites are growing. Figure 4a shows slightly different peak positions than those observed for the other two pressures. The D1 and D3 peaks appear similar, but either the G or D2 peak has shifted from ~1600 cm^{-1} to ~1200 cm^{-1} and the true identity of this peak is not known. In many other spectra collected at 620 Torr, the D3 band grew in intensity to ~1000 and width to ~ 400 cm^{-1}. This could be an indicator that the amount of amorphous carbon has increased, but the widely variable results make it impossible to draw any real conclusions using this peak fitting method.

Soewono and Rogak have presented a comparison of Sadezky's five-peak-fit with a two-peak-fit method(Mernagh, Cooney et al. 1984; Lee, Cole et al. 2002). In their study, several diesel engine soots were compared alongside a highly ordered polycrystalline graphite sample and two carbon black samples. Their comparison shows the same relative assignment of crystallite sizes regardless of peak fitting method. In the present study, both methods have been employed and are shown to be in good agreement. While the five-peak method was not suitable for spectra from samples collected at 620 Torr due to irregularities in peak parameters, the two-peak method did not fit the narrowing structure of spectra from samples collected at 680 Torr. In light of these

fitting concerns, spectra from a given pressure were all fit with the method that produced the best fit. Spectra from samples collected at 660 Torr were fit using both methods.

3.3.2 Differential Scanning Calorimetry – Thermo-gravimetric Analysis

The thermal oxidation and combustion of these particles was analyzed with DSC-TGA. Figure 5 show representative DSC thermograms for samples collected at each pressure. Thermal processing was performed at either 22, 600, or 1100 °C. The primary features common to all DSC plots are the desorption of small organic compounds from 22 – 400 °C, oxidation of organic compounds/functionalities at ~ 400 °C and the pyrolysis of the graphene framework starting from 450 to 500 °C. The assessment of these general features is consistent with what has been reported for diesel soot elsewhere(Stratakis and Stamatelos 2003). While there is some variation in the peak temperatures for the graphene framework combustion, the striking feature of all three soot thermograms is the difference in peak height for the sample collected at 680 Torr and thermally processed at 1100 °C (Figure 5c, orange line). Noting that the scales of the ordinates for all plots have been normalized, the heat output of the sample in question is approximately three times as large as all of the rest. Taking into account the non-zero heat output at room temperature, the total heat produced by this sample was ~45 μV/mg. Interestingly, the heat output for the graphite sample (Figure 5d) was ~30 μV/mg, still twice the heat output of the remaining samples. This could point to increased carbonization of the sample collected at 680 Torr and processed at 1100 °C.

Gravimetric analysis for the samples presented in Figure 5 is shown in Figure 6. The 50% burn off point is indicated with the horizontal dashed line in each plot.

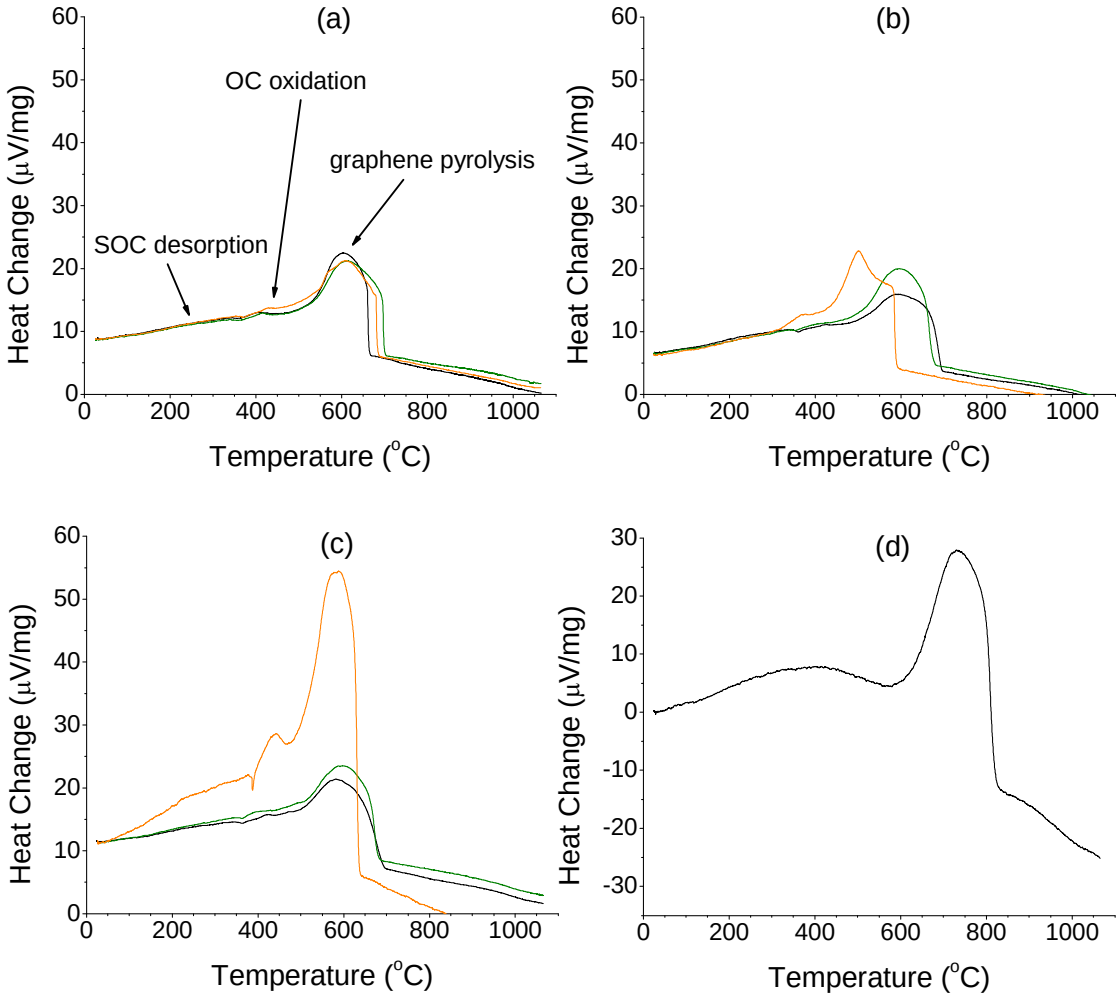

Figure 3.5: Heat change (μV/mg) from differential scanning calorimetry for samples collected at different pressures, (a) 620 torr, (b) 660 torr, (c) 680 torr, and (d) graphite nanoparticles. (black – room temperature, green – 600 °C, orange – 1100 °C thermal processing)

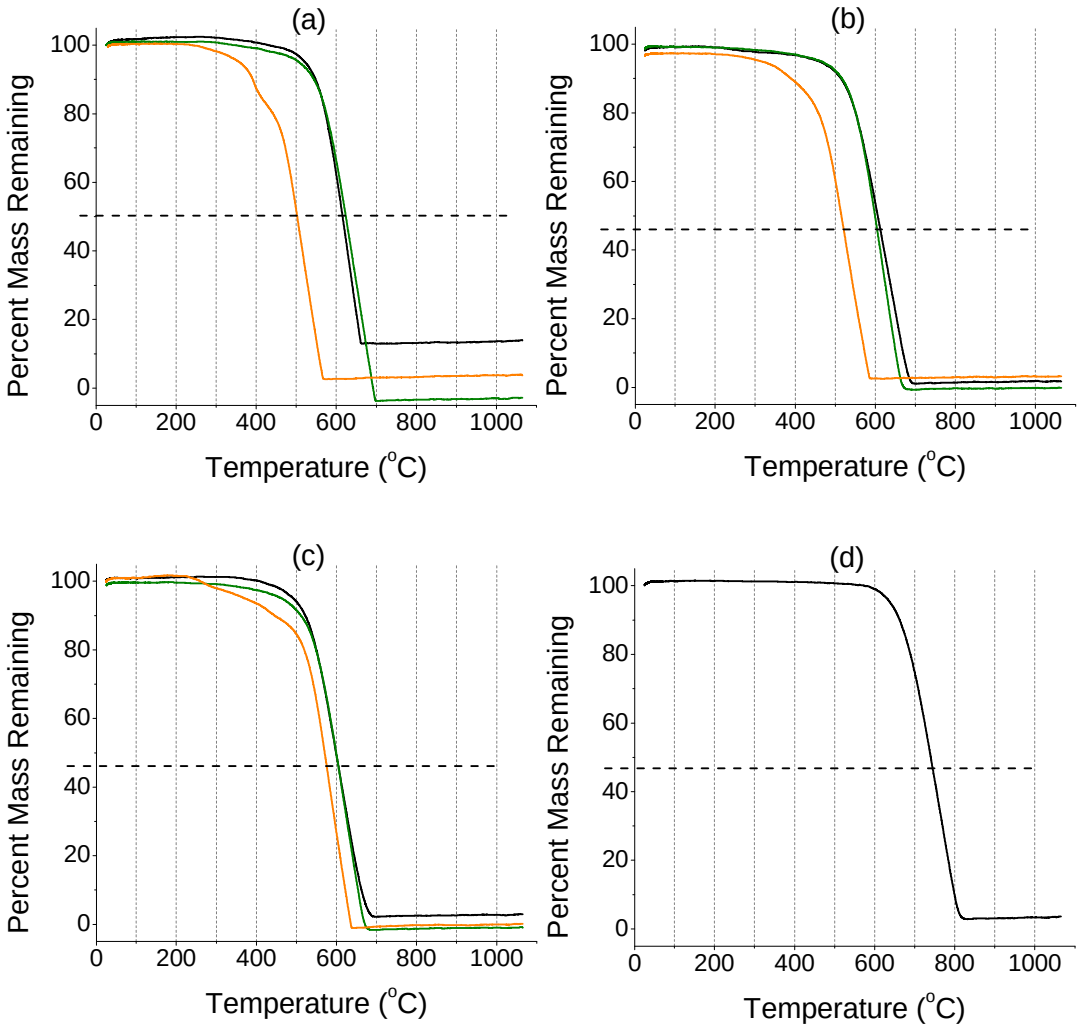

Figure 3.6: Percent mass remaining from thermo-gravametric analysis for samples collected at different pressures, (a) 620 torr, (b) 660 torr, (c) 680 torr, and (d) graphite nanoparticles.

Interestingly, the samples represented with orange lines in each plot begin losing mass at lower temperatures than any other samples. These lines represent particles that were heated to the highest temperature (1100 °C) in the tube furnace. While it has beenreported that charring of organic materials makes them more stable at high temperatures(Leifeld 2007), the TGA data may suggest that these soot samples exhibit an opposite trend. Post-synthesis aerosol-phase thermal treatment at 1100 °C produces particles that are less thermally stable than their unheated counterparts. For all other samples, the 50% burnoff at ~600 °C is consistent with what has been reported elsewhere(Leifeld 2007). The graphite nanoparticle sample presented in Figure 6d, on the otherhand, does not produce a 50% burnoff that is consistent with the 850 °C that has been reported by Leifeld. Instead, 50% burnoff is observed at ~730 °C.

3.3.3 Fourier Transform Spectroscopy

An FTIR spectrum with peak locations indicated is shown in Figure 7. The specific assignments of these peaks is presented in Table 2. In general, spectra collected from these samples exhibit some degree of sp^3 and sp^2 hybridized C-H stretching at ~2900 and 3030 cm^{-1} respectively. There are also varying amounts of oxygen moieties present as evidenced by the peaks at 1700, 1267, 1086, and 1048 cm^{-1}. The broad, strong peak around 1250 cm^{-1} is attributed to carbon skeletal modes of the graphene framework and is present for all samples. The peak at 3435 cm^{-1} is attributed to non-hydrogen bound water adsorbed to either the soot or the KBr. The intensity of this peak was observed to scale with prolonged exposure of the samples and KBr to ambient. Heating the prepared pellets in a vacuum desiccator and heating to 60 °C for one week removed this peak

almost entirely. The peak at 1385 cm^{-1} is observed in pure KBr pellets, so further assignment of this peak is not important to the present study.

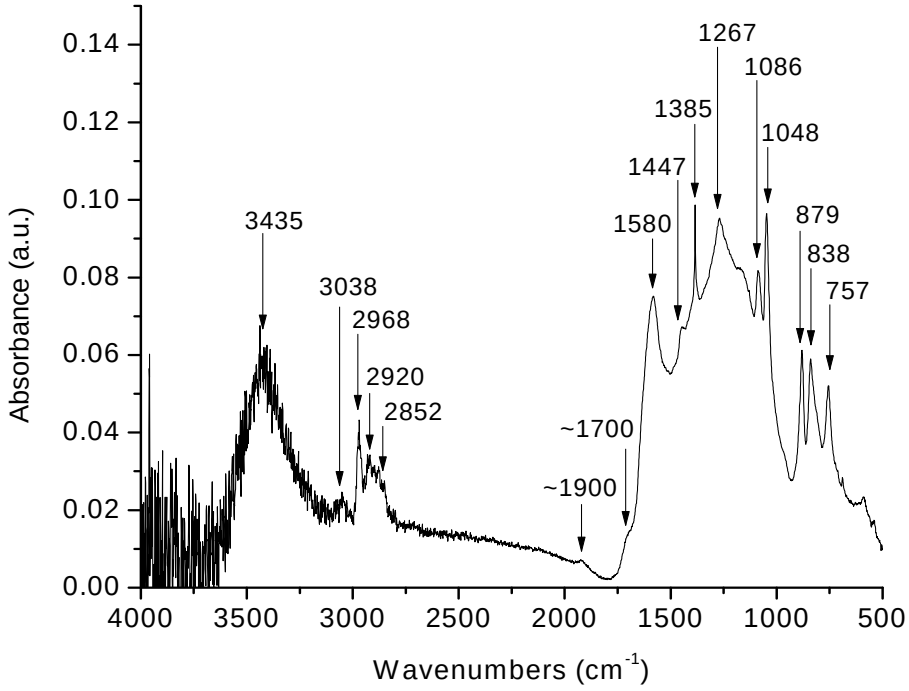

Figure 3.7: Representative FTIR spectrum of soot particles showing peak assignments**.**

Table 3.2: Summary of FTIR peak locations and assignments

Peak Location	Peak Assignment
3435	O-H stretch from absorbed water (Nakahara and Sanada 1995)
3038	C-H stretch from SP2 carbon (Cain, Gassman et al. 2010)
2968	Asymmetric C-H stretch from SP_3 carbon (Cain, Gassman et al. 2010)
2920	Asymmetric C-H stretch from SP_3 carbon (Cain, Gassman et al. 2010)
2852	Symmetric C-H stretch from SP_3 carbon (Cain, Gassman et al. 2010)
~1900	Acetal
~1700	C=O stretch (Cain, Gassman et al. 2010)
1580	Aromatic C=C enhanced by C=O conjugation (Cain, Gassman et al. 2010)
1447	Unsaturated C-H ($=CH_2$) (Cain, Gassman et al. 2010)
1385	KBr
1267	Ether C-O-C stretch (Nakahara and Sanada 1995)
1250	Carbon Skeletal (Shaffer, Fan et al. 1998)
1086	OH, aromatic and α-unsaturated (Cain, Gassman et al. 2010)
1048	Unsaturated hydroxyl C-C-O (Cain, Gassman et al. 2010)
879	Substituted aromatic C-H (Cain, Gassman et al. 2010)
838	Substituted aromatic C-H (Cain, Gassman et al. 2010)
757	Substituted aromatic C-H (Cain, Gassman et al. 2010)

3.4 Discussion

Soot particles have complex chemistries. Depending on their source fuel and combustion parameters, they can be produced with varying degrees of graphene crystallinity and with miriad organic functionalities. Raman spectroscopy has been shown to be an effective method for determining the relative size of graphene crystallites within various soot samples. Using the peak fitting methods discussed above and developed elsewhere, each of the Raman spectra was fitted with either two Lorentzian peaks or four Lorentzian and one Gaussian peak. Figure 8 shows the data from both fitting methods for all sampling conditions. While the narrowing of the D1 peak at higher temperatures and higher pressures shown in Figure 4 may indicated an increase in graphene crystallite size, the data presented in Figure 8 clearly establishes unique trends for each collection pressure. For soot samples collected at 620 Torr (black squares), the D/G band area ratio does not appear to have any correlation to the furnace temperature. For these samples, the graphene crystallite size varies widely irrespective of the processing temperature. The D/G band area ratio varies from 2.6 representing the largest crystallites, to nearly 3.2 representing the smallest crystallites. Particles collected at 620 Torr and subsequently thermally processed at any temperature can contain crystallites with similar sizes to the smallest or largest crystallites produced in particles collected at 660 Torr. There is, however, little or no apparent control over the crystallite sizes for these particles, at least not within the parameters and conditions presented herein.

Looking again at the data for samples collected at 660 Torr (blue circles), the crystallites start at some intermediate size when no thermal processing is performed, but

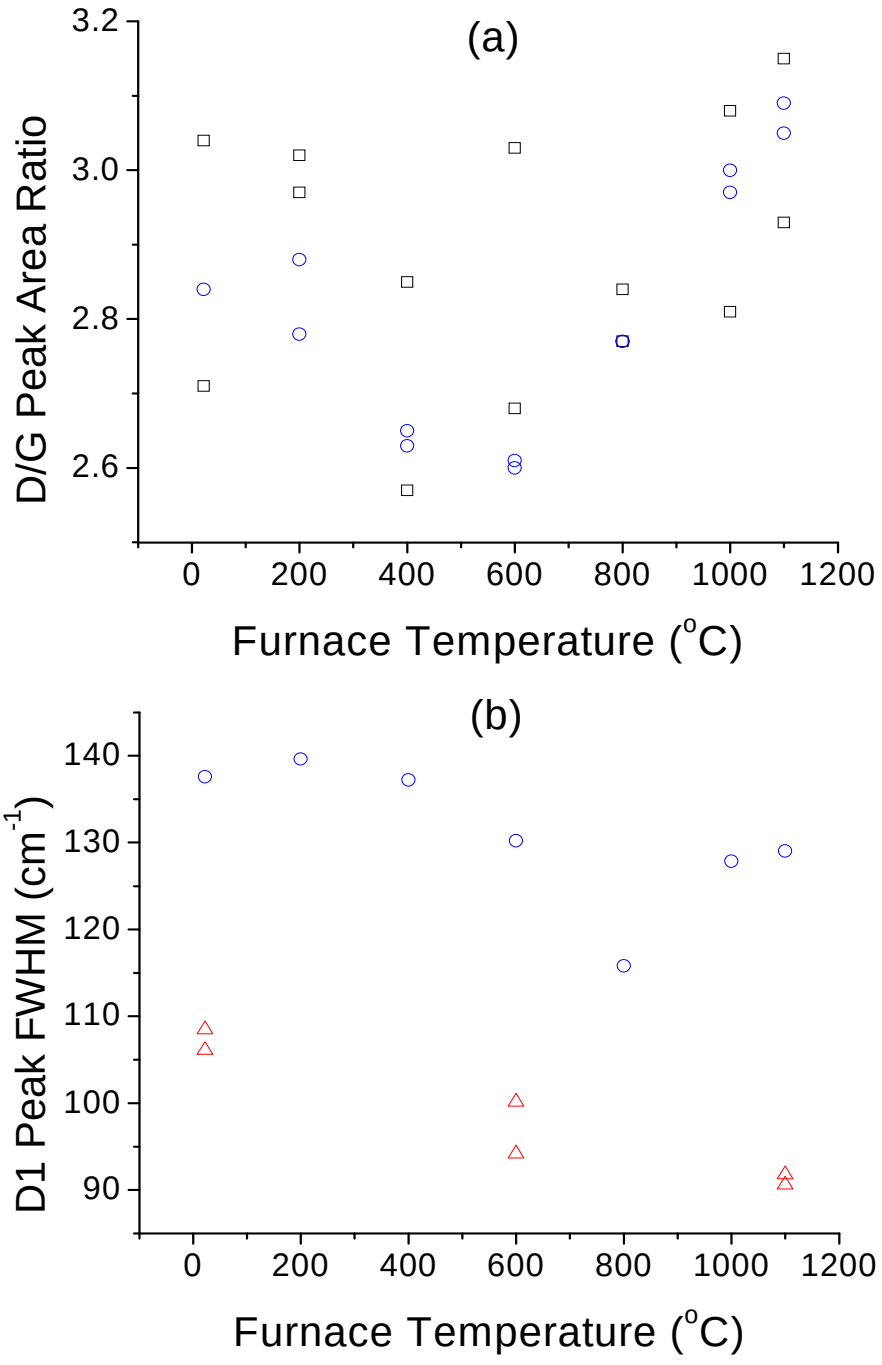

Figure 3.8: Data from analyzed Raman spectra either (a) two peak fitting and D/G band area ratio, or (b) five peak fitting and FWHM of D1 peak. (squares, 620 torr; circles, 660 torr; triangles, 680 torr).

increase with increasing furnace temperature up to an intermediate temperature. The exact temperature at which the crystallites stop growing is not clear due to conflicting data from the different peak fitting methods (both fitting methods are reported for these samples to better correlate relative crystallite size across the fitting methods). Using the 2-peak-fitting method, the maximum crystallite size is reached around 600 °C, but the 5-peak-fitting method results in a maximum at 800 °C. For both fitting methods, the relative crystallite size increases to this intermediate temperature and then decreases through the high temperature limit of the furnace. Apparently the process for crystallite growth has a complex dependence on processing temperature. While no mechanistic studies of these processes have been performed in the present study, the oxygen levels present downstream of the furnace shown in Figure 2 may indicate that the process for crystallite growth involves gaseous oxygen or oxygen containing surface functionalities. This could help explain the lack of crystallite size/temperature correlation for particles collected at 620 Torr as it was an intentionally anaerobic aerosol flow. For these particles little or no oxygen was available in the gas phase for crystallite growth, but some samples may have scavenged oxygen-containing surface functionalities resulting in increased crystallite size. If this suggested role of oxygen in the crystallite growth is indeed correct, it is not clear why some samples exhibit scavenging while others do not.

For soot samples collected at 680 Torr (red triangles), the crystallite size with no thermal processing is measurably larger than those for any samples collected at either 620 or 660 Torr regardless of furnace temperature. In similar fashion to the soot collected at 660 Torr, the crystallite size for these high-pressure samples increases up to 600 °C.

Then, uniquely, with increasing furnace temperature, the crystallite size continues to increase as well. The Raman data suggests that increasing furnace temperature results in larger crystallites for all samples collected at 680 Torr, there is no change in this trend at an intermediate temperature. Due to the presence of approximately 1 % gaseous oxygen in the aerosol phase at this pressure, there may be more support for crystallite growth through an oxygen consuming mechanism. As with samples collected at the intermediate pressure (660 Torr), the oxygen in the aerosol phase may serve as a source for this proposed crystallite growth up to 600 °C at which point any excess gaseous oxygen not consumed in crystallite growth is burned in the tube furnace. At higher temperatures there maybe some specific chemistries of particles produced at 680 Torr that allows more efficient scavenging of oxygen-containing functionalities for continued crystallite growth.

Further support for the growth of the graphene crystallites under specific conditions can be found in the GSC-TGA data (Figure 5). The large heat output for the soot sample collected at 680 Torr and thermally processed at 1100 °C supports the growth of graphene crystallites and increase in the fractional carbon content of these soot particles. Evidently, changes in crystallite size detected with Raman spectroscopy for all samples other than the one in question was not significant enough to affect their heat content. The sample collected at 680 Torr with greater heat output, on the other hand, is significantly different from the others and has a heat output more similar to the graphene sample than the others.

The lower onset temperature for mass loss and lower complete burn-off temperature in all samples thermally treated at 1100 °C does not support the trends in crystallite size changes found through Raman spectroscopy. Since this TGA data is seemingly inconsistent with the Raman data, it must either contradict it or be rooted in other causes. In fact, the low-temperature burn off for these samples may suggest that high furnace temperatures prime these soot particles for future combustion. The initial combustion that undoubtedly occurs win the tube furnace leaves decomposed functionalities and deteriorated structures that begin combustion much easier later. In this way, it thermal treatment at 1100 °C is much like producing charcoal. As mentioned above, the 50% burn off for the graphite standard is lower than has been reported elsewhere. This is however, likely due to morphological differences in the samples. In the literature, graphite was obtained from a graphite rod and may have been larger crystalline pieces while the standard used for the present study was a nano powder. This may be a good example of the difference between bulk and nano-scale material properties.

The representative FTIR spectra shown in Figure 9 may help support a possible role of oxygen in the growth mechanism for graphene crystallites. These spectra represent soot samples with small, medium, and large crystallites (black, green, and orange respectively). For the spectrum of small crystallites, there is little difference from the spectrum shown above in Figure 7. There is clear signal from the aliphatic C-H stretch (~ 2900 cm^{-1}) with very little aromatic C-H stretching. The lack of significant C-H stretching in the aromatic region above 3000 cm^{-1} is likely due to the highly symmetric

nature of the graphene framework. In addition to the C-H stretching, there are peaks for several oxygen-containing functionalities including a carbonyl, ether, and hydroxyl (1700, 1267, and 1086 cm^{-1} respectively). As the relative crystallite size increases from small to medium and then to large, the peaks for C-H stretching above 3000 cm^{-1} grow. While growth of the crystallites does not necessitate an increase in the aromatic C-H stretching peaks, the loss of edge site organic functionalities would likely cause this increase. As substituted aromatic structures become less and less substituted, the vacated sites would likely be filled with hydrogen. This would cause an increase in the aromatic C-H signal above 3000 cm^{-1}. Looking at the change in the peaks attributed to oxygen moieties mentioned above, many of these peaks either decrease in size or are completely absent in the spectrum for large crystallites. This, in addition to the increase in the signal strength for substituted aromatic C-H at 879, 838, and 757 cm^{-1} supports the idea that oxygen containing functionalities are driven off or consumed as graphene crystallites increase in size. Furthermore, the narrowing of the peak at 1580 cm^{-1} with increasing crystallite size supports the loss of carbonyl functionalities from these particles as this peak is enhanced by conjugation with carbonyls. While these

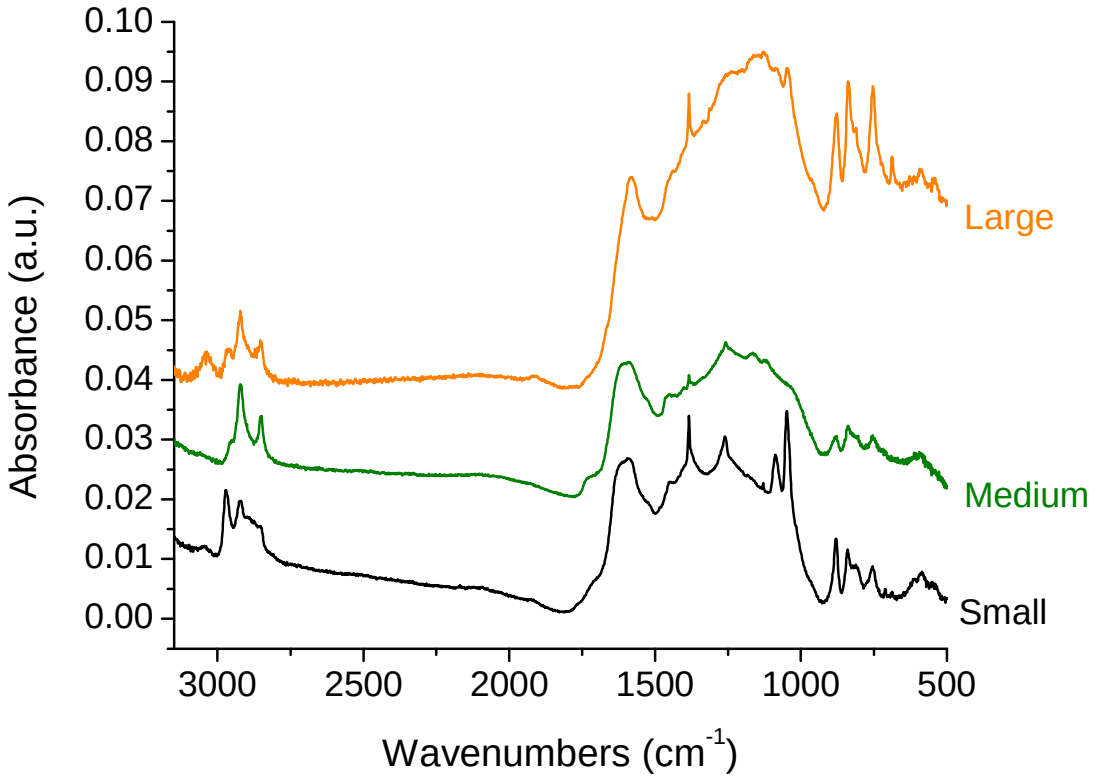

Figure 3.9: Representative FTIR spectra from soot sample with small, medium, and large graphene crystallites (relative crystallite size indicated).

representative FTIR spectra offer little or no support for changes to the graphene crystallite size, they clearly show changes in the organic functionalities. In general, samples exhibiting larger crystallites appear to contain fewer organic functional groups having been replaced either by increasing the size of the conjugated aromatic framework, or by producing unsubstituted edge sites.

Changes in the relative graphene crystallite sizes for various particles and the trends for these changes reported above are interesting, but without some information about the significance of these changes, they carry little meaning. The TEM micrographs shown in Figure 10 help give some quantification to the relative changes reported. Figure 10a represents particles with small crystallites. The fuzzy nature of the material within each particle is evidence of its amorphous structure. There is some definition of small crystallites (the dark spots and lines), but these crystallites are too small to achieve good resolution. Particles with measured medium sized crystallites (Figure 10b,c) exhibit slightly greater definition of the crystallites. They also exhibit the same general primary particle diameter of ~ 20 nm. The primary particle size, particle agglomeration, and fractal structure of the samples represented in Figures 10a,b,c are consistent with particles collected under all conditions and processed at all temperatures except for those collected at 680 Torr and processed at 1100 °C. Figure 10d shows that these unique particles have coalesced into larger particles with primary diameters of several hundred nanometers. Furthermore, high-resolution images of these particles shows(Figure 10e,f) the sintering of small particles. These high-resolution images clearly show larger crystallites than for any other samples.

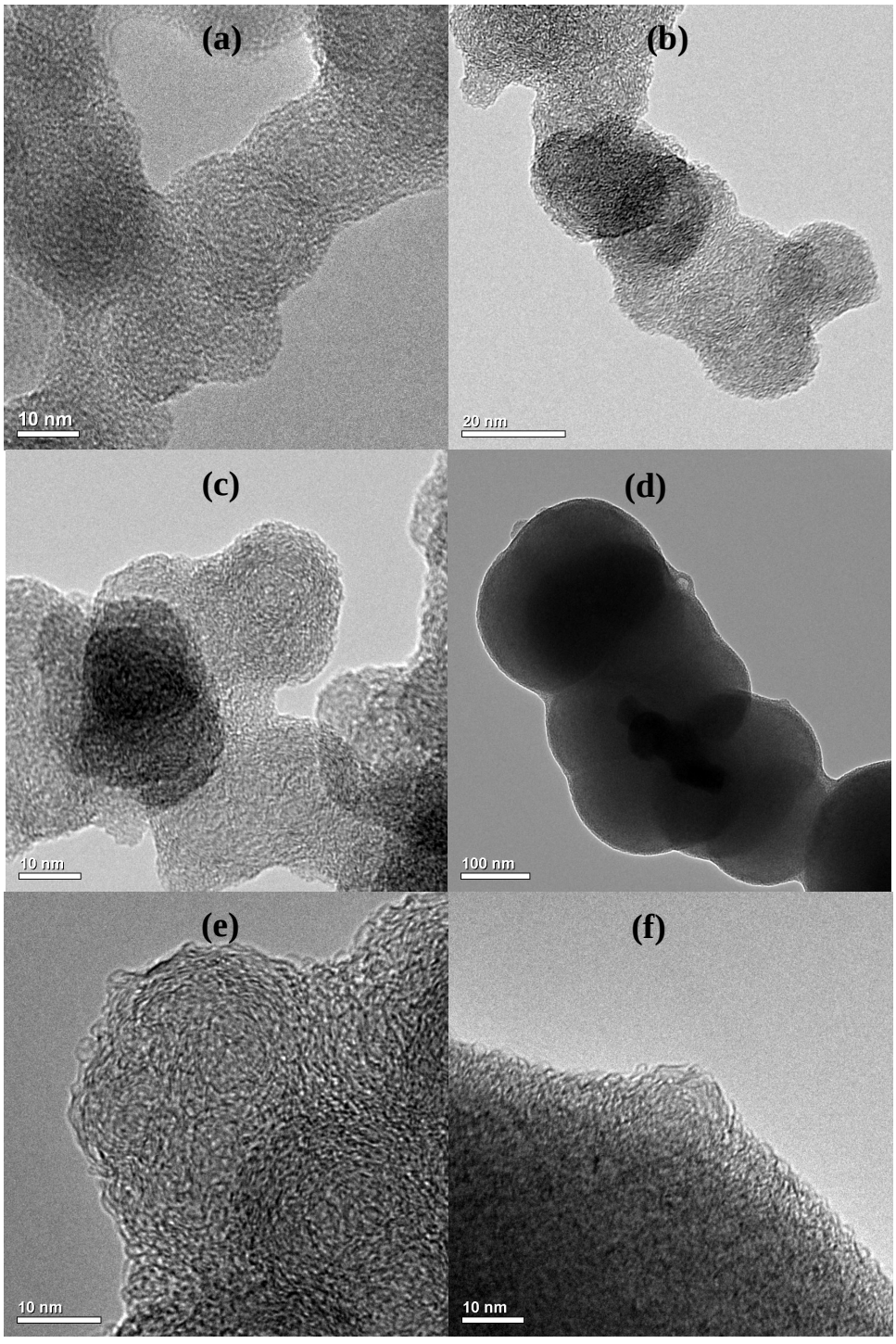

Figure 3.10: Representative TEM images of soot particles collected under conditions that produce (a) small crystallites, (b-c) medium crystallites, (d-f) large crystallites.

3.5 Conclusion

Soot particulates in the atmosphere have gained much attention in discussions about public health and climate change. Systems and processes for the regeneration of diesel soots have become increasingly important as these soots are one of the primary sources for urban particulates. The success of any regeneration process is ultimately dependant on the reactivity of the particulates, a property which can be controlled through their structure. The present study has investigated the effects of post-sythesis aerosol-phase heating on the nanostructure of natural gas soots produced under various conditions. These soots, while not identical to diesel soots, do serve as a good starting point from which to begin a more broad investigation into the effects of heating on various types of soot particles.

Raman spectroscopy and TEM analysis have shown aerosol-phase heating to be effective at producing large graphene crystallites within some soot samples. The factors that influence the growth or shrinkage of the crystallites likely include production pressure and temperature, oxygen partial pressure, and graphene crystallite chemistries. While increased furnace temperature produced larger crystallites for some particles, others showed no apparent change, and others still showed decreased crystallite size. Furthermore, all samples heated to 1100 °C exhibited lower combustion temperatures upon further heating. Apparently, the heating process primed these particles for combustion, leaving partially decomposed functionalities or adsorbed small organic molecules. Clearly, there are competing factors with complex influences on the crystallite growth mechanism.

Chapter 4

Sulfuric Acid Treatment and Water Adsorption of Freshly Generated Natural Gas Soots

The effects of post-synthesis aerosol-phase oxidative processing on water uptake of natural gas soot were examined. Soot was produced from incomplete combustion of natural gas at different pressures, heated in the aerosol state to temperatures between room temperature and 1100 °C under several different oxygen partial pressures, exposed (or not) to sulfuric acid and then exposed to humid air. Change in particle mobility diameter were measured using tandem differential mobility analysis. While the morphology and composition of the soot particles is thought to influence water uptake, and oxidative processing has been shown to affect both graphene crystallite size and composition, no correlation between water uptake and oxidative processing was confirmed. Sulfuric acid treatment prior to exposure to humid air was shown to result in enhanced water uptake. Several reasons for the high degree of uncertainty within the experimental data are explored including volatile organic content and changes to flow dynamics within the experimental apparatus. The possible atmospheric implications of the primary finding are discussed in relation to likely influences the oxidative processing will exhibit through further exploration. Useful future investigations are briefly outlined.

4.1 Introduction

Soot particles are a major fraction of particulate matter in the atmosphere (Sheridan, Brock et al. 1994; Kuhn, Petzold et al. 1998). They are produced naturally through forest fires and volcanic activity and anthropogenically in jet turbine engines, internal combustion engines, and biomass burning. Soot particles have complex structures, morphologies, and chemical compositions as a result of their myriad sources (Studebaker and Snow 1955; Cachier 1998). In the atmosphere, soot particles are an important factor in climate change (Cachier 1998; Seinfeld and Pandis 1998; Jacobson 2002; Zuberi, Johnson et al. 2005). Large particles are strongly absorbing in the visible and UV range and may cause increases in atmospheric temperatures (Nienow and Roberts 2006). Small particles are activated as cloud condensation nuclei (CCN) increasing the reflectivity of clouds and cooling the atmosphere (Cachier 1998; Ackerman, Toon et al. 2000). Clouds play a large role in the Earth's radiative budget so any changes in cloud albedo will affect climate (Jensen and Toon 1997). While soot particles are removed from the atmosphere through rainout or wet scavenging, fresh soot particles are generally hydrophobic (Schrader 1975; Chen, Hung et al. 1993). After entering the atmosphere they undergo an aging process that increases their hydrophilicity (Chughtai, Brooks et al. 1996; Weingartner, Burtscher et al. 1997). They react with other species in the atmosphere including OH, O_3, SO_2, HNO_3, and N_2O_5, changing their composition and surface chemistries (Brodzinsky, Chang et al. 1980; Harrison and Pio 1983; Smith and Chughtai 1997; Mikhailov, Vlasenko et al. 2001; Decesari, Facchini et al. 2002). Fresh soot contains absorbed small organic molecules which have been shown

to affect their hydroscopic properties(Barthazy, Stetzer et al.). These factors and others influence the behavior of soot in the atmosphere ultimately affecting global climate.

Considering the impact soot particles have in the atmosphere and the number of oxidative species they interact with, it is important to understand how oxidative processing changes the hydroscopic properties of these particles. While it has been shown that sulfuric acid is not necessary to activate soot particles as CCN, there is an understanding that sulfuric acid and other oxidizing sulfur-containing species likely still play a role in the aging processes of many soot particles (Karcher, Peter et al. 1996; Persiantseva, Popovicheva et al. 2004). Previous work has shown that post-synthesis aerosol-phase heating under different oxygen partial pressures and at different production pressures results in the controlled growth or shrinkage of the graphene crystallites. Along with the change in crystallite size, infrared spectroscopy has shown evidence of changes in the chemical composition of the graphene; as the crystallites grow, polar oxygen-containing functional groups are lost. Holding all other factors equal, growth of the crystallites accompanied by decreases in polarity should result in particles that resist droplet activation more. The hydrophobic nature of the polycyclic aromatic hydrocarbon framework should only increase with crystallite growth. The present study seeks to examine how oxidative processing of soot particles affects their hydroscopic properties. Soot particles were oxidized in a tube furnace at various temperatures and oxygen partial pressures resulting in particles with varying degrees of crystallinity, compositions and particle sizes.

4.2 Experimental Details

4.2.1 Experimental Apparatus

Natural gas soot particles were produced using a diffusion burner running 510 sccm natural gas and 85 Lpm dry sheath air (Figure 1). Particles were extracted from the flame 50 mm above the base into a 12 mm outer diameter quartz tube through a 1 mm orifice. The pressure of the aerosol system was monitored just upstream of the orifice and maintained at 620, 660, or 680 Torr. Immediately downstream from the diffusion burner, the moist combustion aerosol was dried in a copper condenser using ice-cold circulating water. The oxygen partial pressure of the aerosol stream, which was found to relate to the total aerosol pressure, was monitored down to 0% oxygen. Three oxygen partial pressures (0, 1.5, and 1%) corresponding with the three aerosol total pressures 620, 660, and 680 Torr respectively were examined. These conditions, described previously, were chosen based on local maxima and minima in oxygen partial pressures that were attainable. After drying, the particles were passed through a tube furnace (Lindberg-Blue model HTF55122A) at temperatures from room temperature to 1100 °C, or through the furnace bypass line. The tube furnace contained a 2 inch outer diameter quartz tube to increase residence time within the furnace. A second copper condenser was used after the furnace to remove any remaining water vapor or volatile organic compounds desorbed or generated within the tube furnace. The aerosol/ambient pressure differential was maintained with a Venturi pump downstream of the second condenser using dry nitrogen gas. Passing through the venturi pump, the aerosol stream increased in

pressure to atmospheric pressure and flowed into a differential mobility analyzer (DMA)(TSI nano-DMA model 3085). The poly-disperse aerosol flow rate was maintained at 1.5 Lpm with accompanying nitrogen DMA sheath flow of 15 Lpm. Excess aerosol flow was allowed to vent through the venturi pump so as to maintain the proper DMA flow ratios. The first DMA was set to a static voltage and the selected mono-disperse aerosol flow was either passed through the reaction zone or bypassed the reaction zone. For the reaction zone, fuming sulfuric acid with an overhead nitrogen gas flow rate of 10 sccm was added to the aerosol stream after which the acid laden aerosol stream was passed through a quartz tube heated to approximately 40 °C. The heating was used to increase the gas-phase sulfuric acid concentration thereby enhancing acid uptake onto the soot particles. For reaction line as well as the bypass line, moist air was added to the aerosol stream with relative humidities (RH) from 0 to 100% (0% RH may contain a small amount of water vapor that was not removed from the moist combustion source). Relative humidities of 0 or 80% were used most commonly. A two inch outer diameter glass tube 24 inches long was used downstream of the humid air addition to increase residence time. After water vapor condensation, the particle stream was passed into the second DMA set to scan across a wide range of voltages. The use of similar DMA systems has been described elsewhere and has gained widespread use in recent years. An ultrafine condensation particle counter (TSI model 3776) was used to count particles passing through the second DMA.

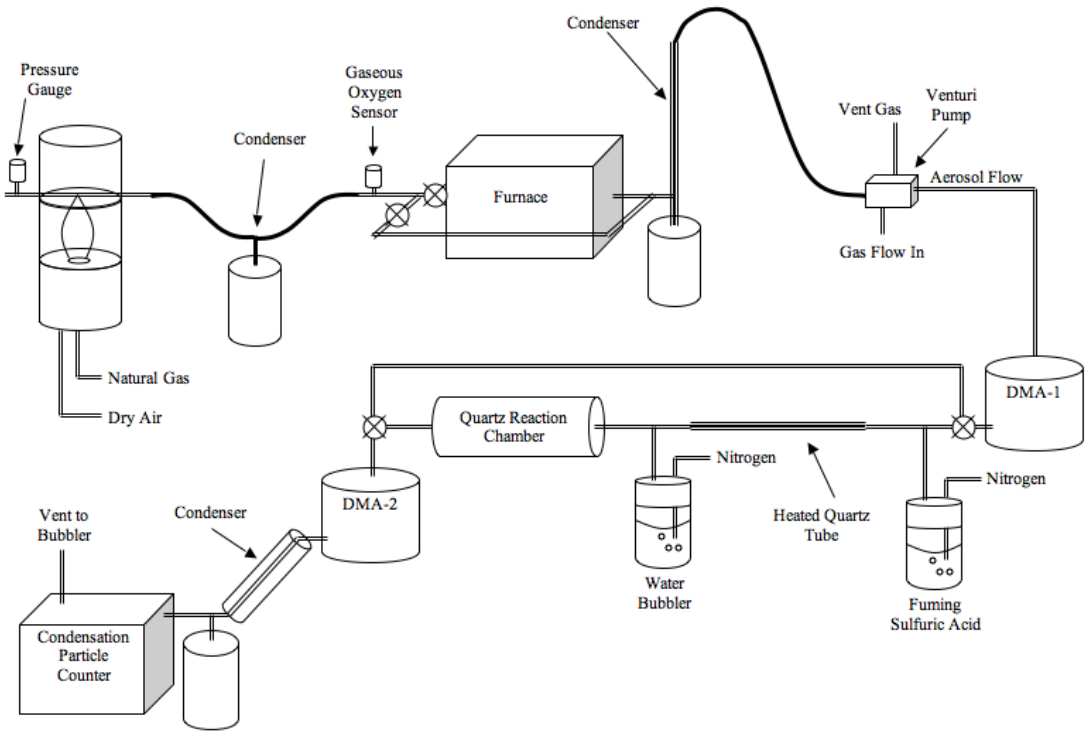

Figure 4.1: Schematic illustration of the experimental setup for sulfuric acid treatment and water adsorption measurements.

4.2.2 Particle Distributions

While the specific shape of the full particle distribution is influenced by the exact production conditions, Figure 2 shows a representative particle distribution (orange diamonds). No particles were counted below mobility diameter 20 nm, but the number increases rapidly up to 60 nm. The distribution is assumed lognormal based on previously reported data but the present study was unable to measure above 60 nm due to instrumental limitations. The distribution for size-selected particles (green squares) is considered mono-disperse.

The homogeneous nucleation of sulfuric acid within the reaction line was measured to ensure little or no interference at experimental acid flow rates. Figure 3 show the distributions for homogeneous acid nucleation at various flow rates through the acid bubbler. Nitrogen flow rates at or above 15 sccm produce varying amounts of homogeneous nucleation. While these particle counts are significantly lower than the soot particle counts at corresponding mobility diameters, 10 sccms nitrogen flow was used to avoid measurable homogeneous nucleation.

For average particle mobility diameters, ten individual mono-disperse particle distributions were measured. In some cases, less than ten points are reported due to low confidence in the data or significant changed to operational parameters within the soot synthesis system. Figures 4-12 show the mean diameters for each of the individual distributions having been calculated using a Gaussian fit. Standard deviations were calculated for the averages and are reported as error bars for the raw data. The dashed

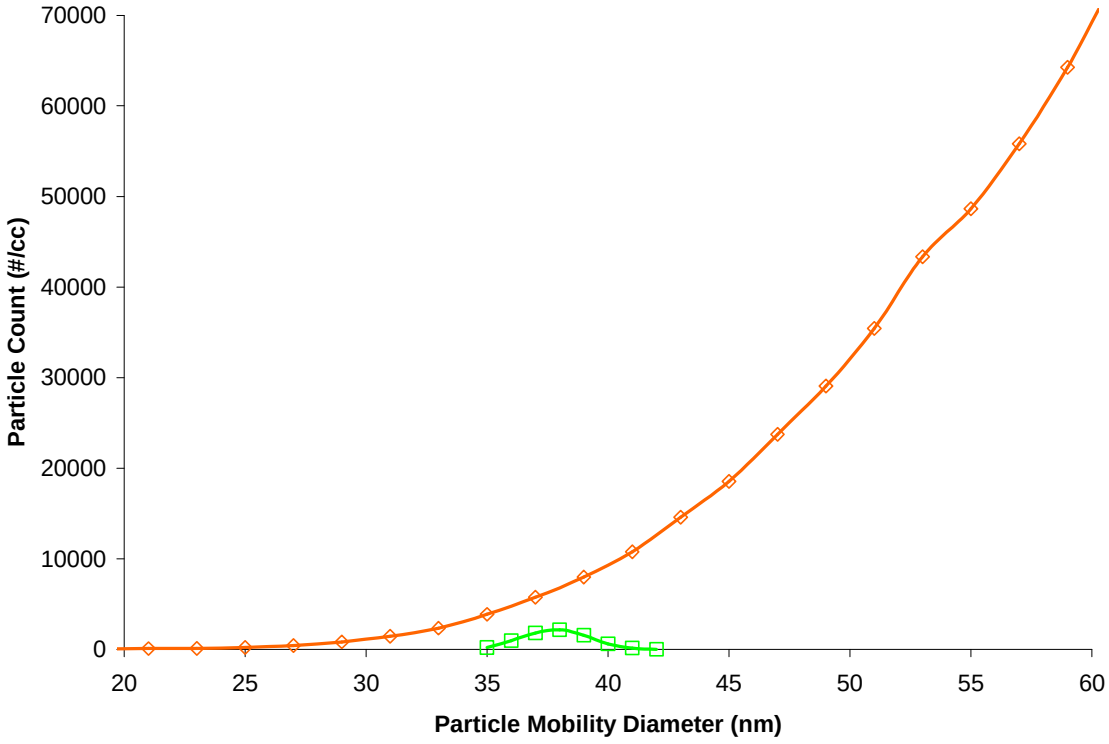

Figure 4.2: Representative particle distribution (orange diamonds) with monodisperse sampling (green squares).

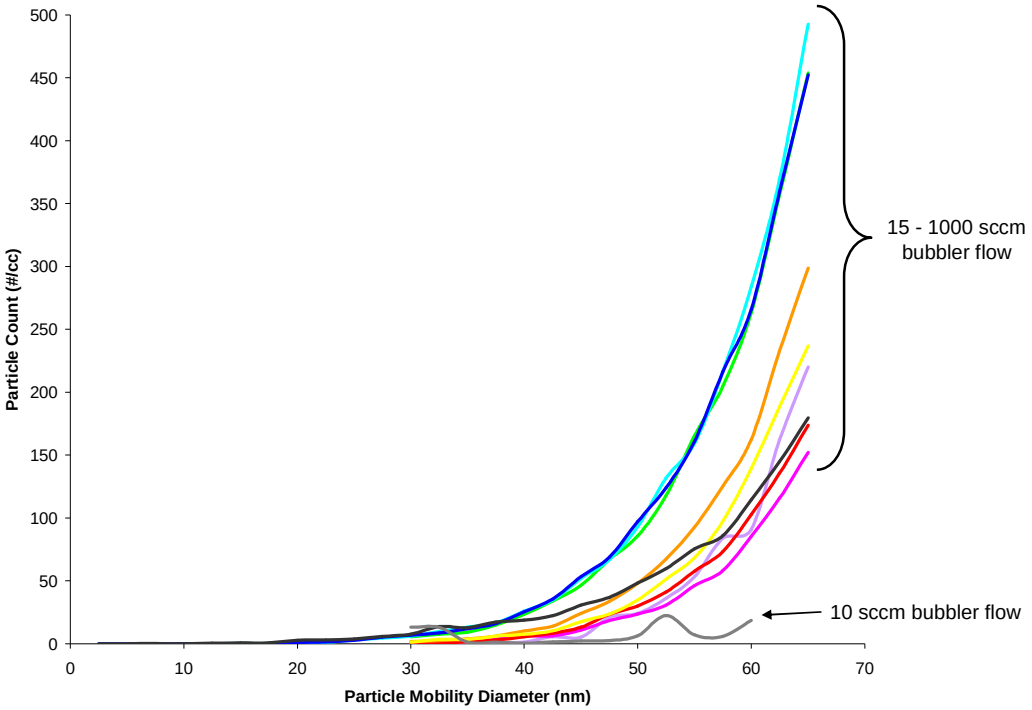

Figure 4.3: Particle counts for homogeneous nucleation of sulfuric acid at various bubbler nitrogen flow rates.

horizontal lines represent the calculated average mobility diameters and include the calculated average value on the left, the averages are listed with the dashed lines.

4.3 Results

Figures 4-12 represent soot samples that were collected under various oxidative conditions. Soot particles were collected at three different pressures, 620, 660, and 680 Torr and subsequently passed through the tube furnace at three different temperatures, 22, 800, and 1100 °C. In total, nine different oxidative conditions were examined and are represented, one each, in the raw DMA data figures. These oxidative conditions have been investigated previously, along with their effects on the soot nanostructure and surface chemistries.

Looking at Figure 4 (620 Torr, room temperature furnace, 0% oxygen) 0.07 nm of water has been absorbed by particles that were not treated with sulfuric acid, but 0.38 nm of water was added after sulfuric acid treatment. This general trend, sulfuric acid treatment increases the total amount of water vapor that is absorbed by soot particles, can be seen in virtually all of the reported data. Figure 13 shows the change in the mobility diameter (Δd_p) for all samples when no acid was added and dry air was used instead of humid air. The average mobility diameter for each of the three pressures when the tube furnace was set to room temperature and neither acid nor moisture were included, are set as the baseline values. While the actual measured mobility diameters under these conditions were not equal and varied from day to day, each new experiment was calibrated based on one of these values before new data was collected. In this way, daily variations in the

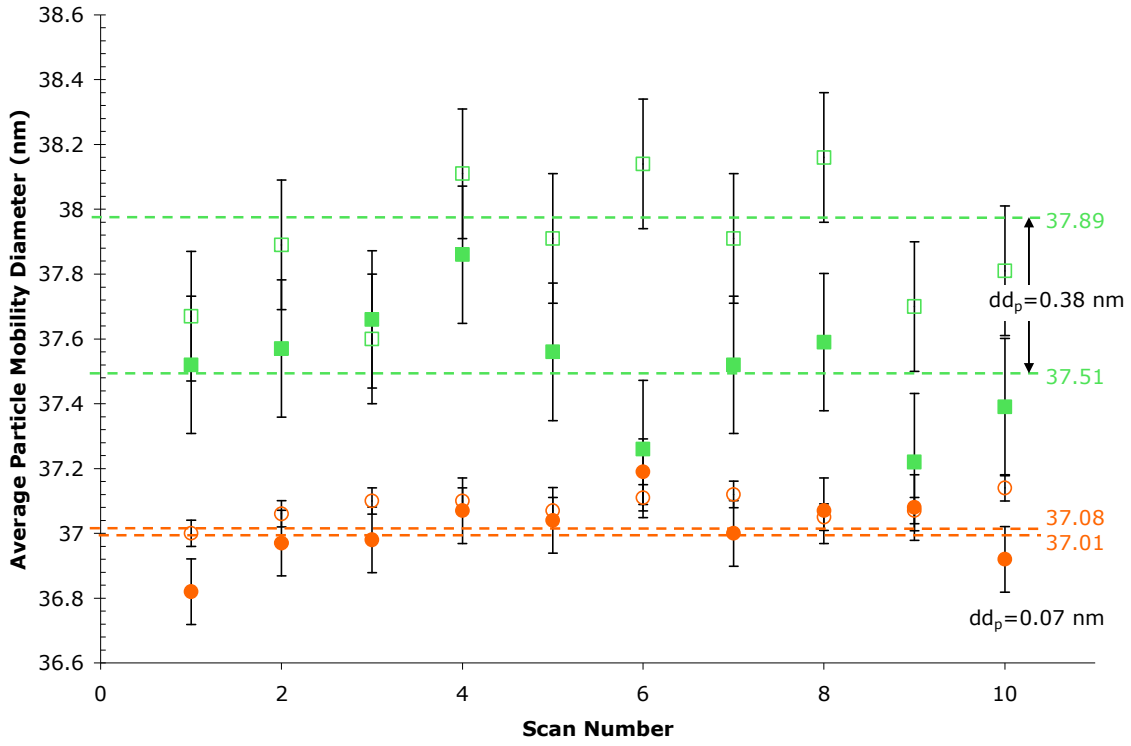

Figure 4.4: Measured particle mobility diameters for individual scans of particles collected at 620 torr with no heating (standard deviation shown), average mobility diameter shown with dashed line (● bypass, 0% RH; ○ bypass, 90% RH; ■ acid line, 0% RH; □ acid line, 90% RH)

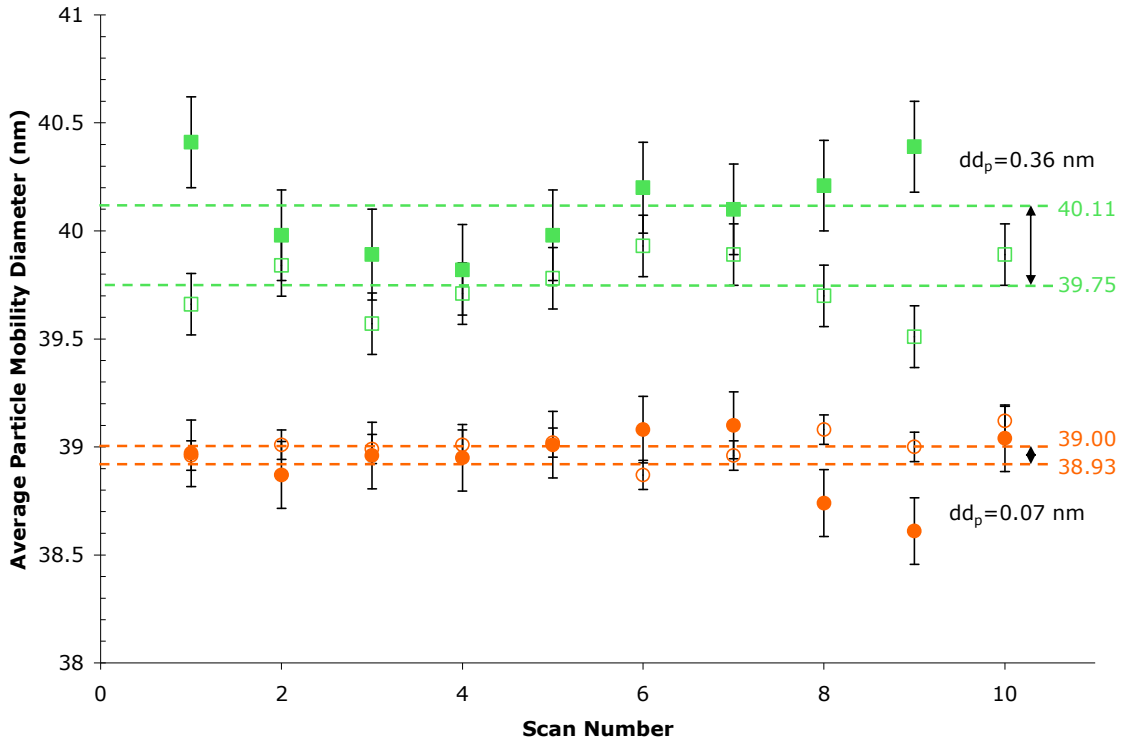

Figure 4.5: Measured particle mobility diameters for individual scans of particles collected at 620 torr heated to 800 °C (standard deviation shown), average mobility diameter shown with dashed line (● bypass, 0% RH; ○ bypass, 90% RH; ■ acid line, 0% RH; □ acid line, 90% RH)

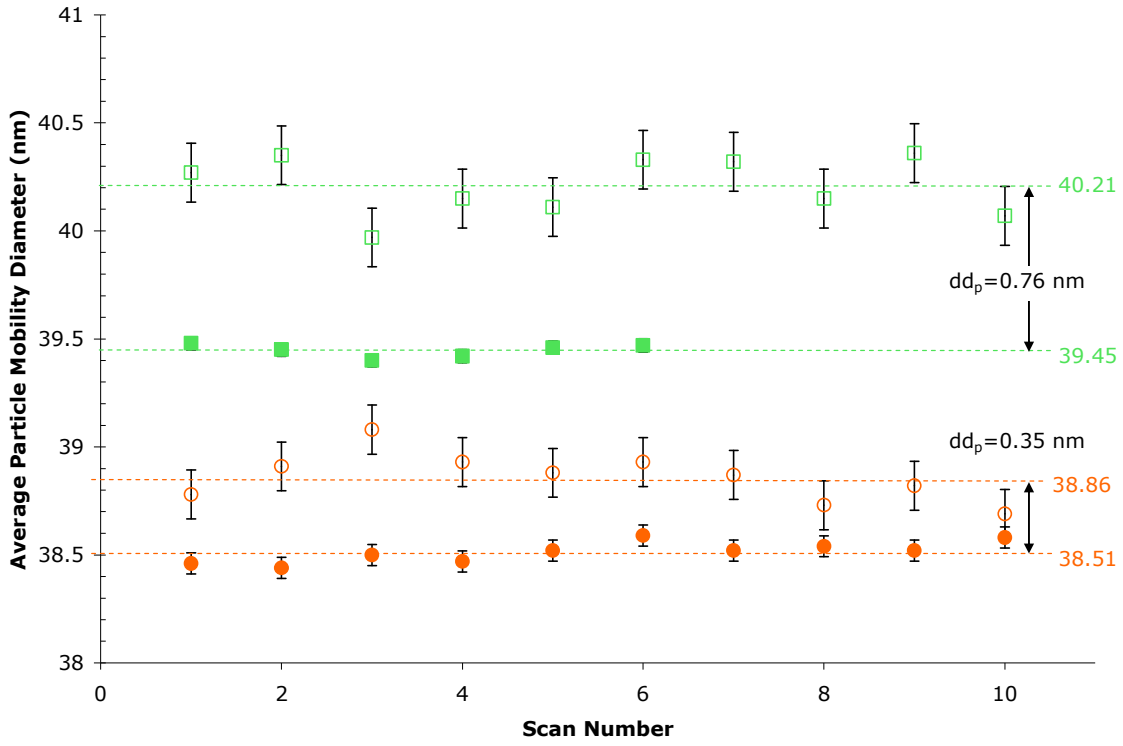

Figure 4.6: Measured particle mobility diameters for individual scans of particles collected at 620 torr heated to 1100 °C (standard deviation shown), average mobility diameter shown with dashed line (● bypass, 0% RH; ○ bypass, 90% RH; ■ acid line, 0% RH; □ acid line, 90% RH)

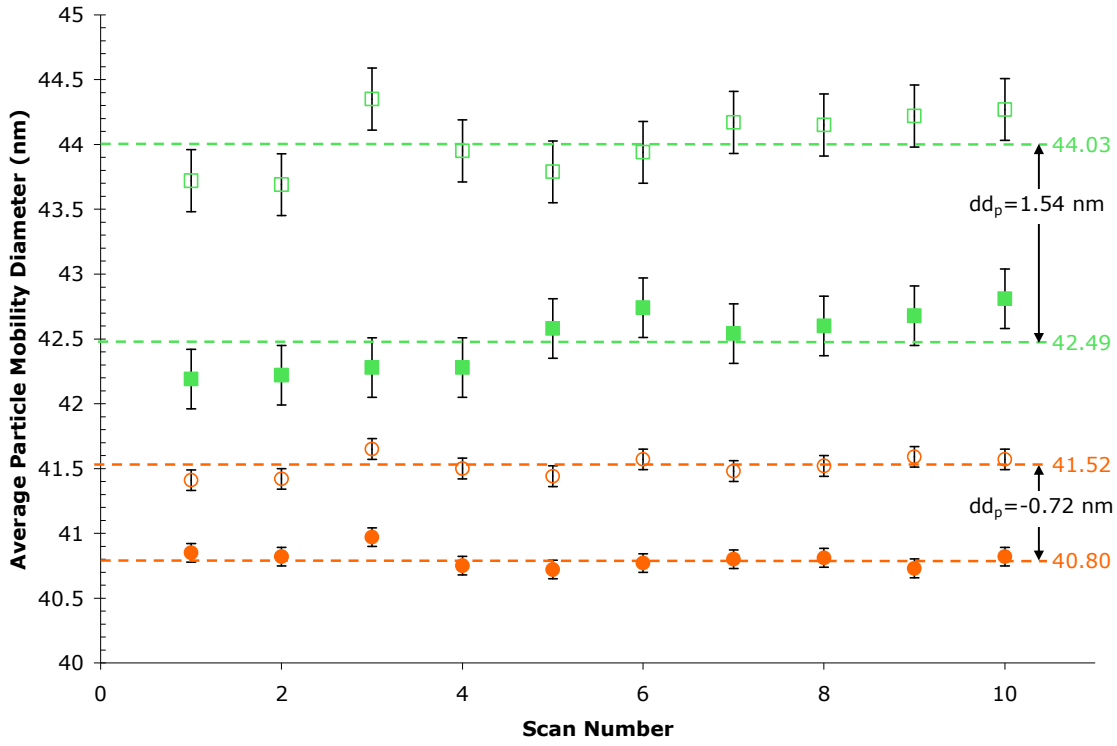

Figure 4.7: Measured particle mobility diameters for individual scans of particles collected at 660 torr with no heating (standard deviation shown), average mobility diameter shown with dashed line (● bypass, 0% RH; ○ bypass, 90% RH; ■ acid line, 0% RH; □ acid line, 90% RH)

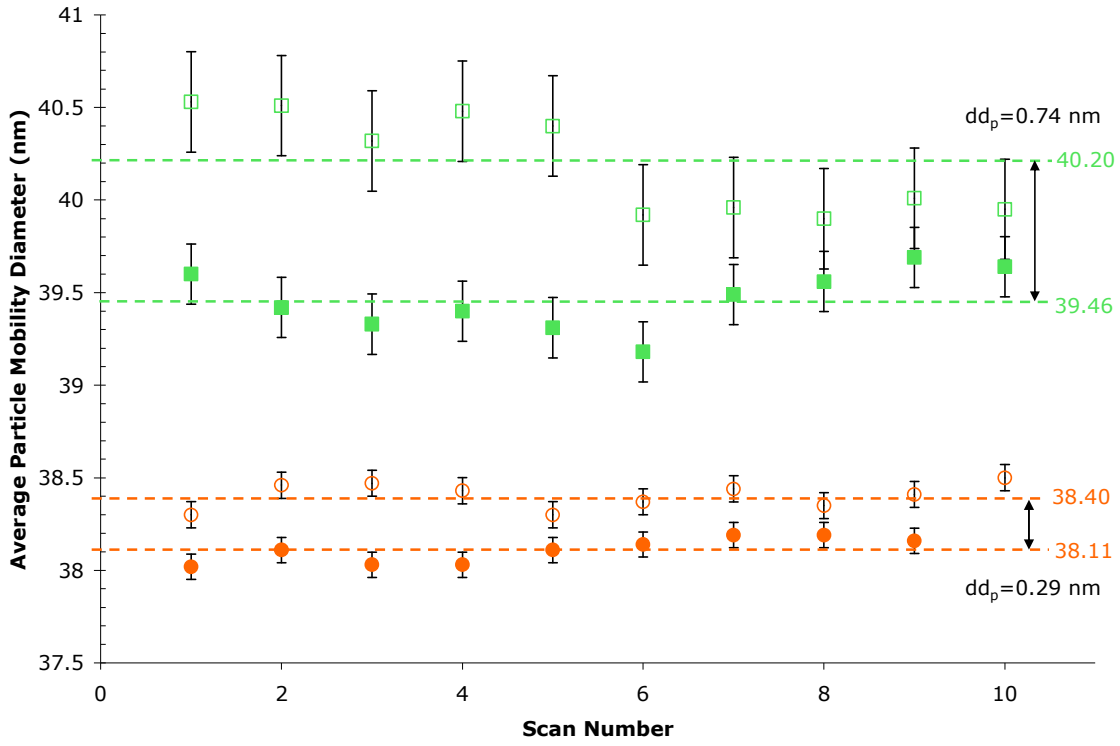

Figure 4.8: Measured particle mobility diameters for individual scans of particles collected at 660 torr heated to 800 °C (standard deviation shown), average mobility diameter shown with dashed line (● bypass, 0% RH; ○ bypass, 90% RH; ■ acid line, 0% RH; □ acid line, 90% RH)

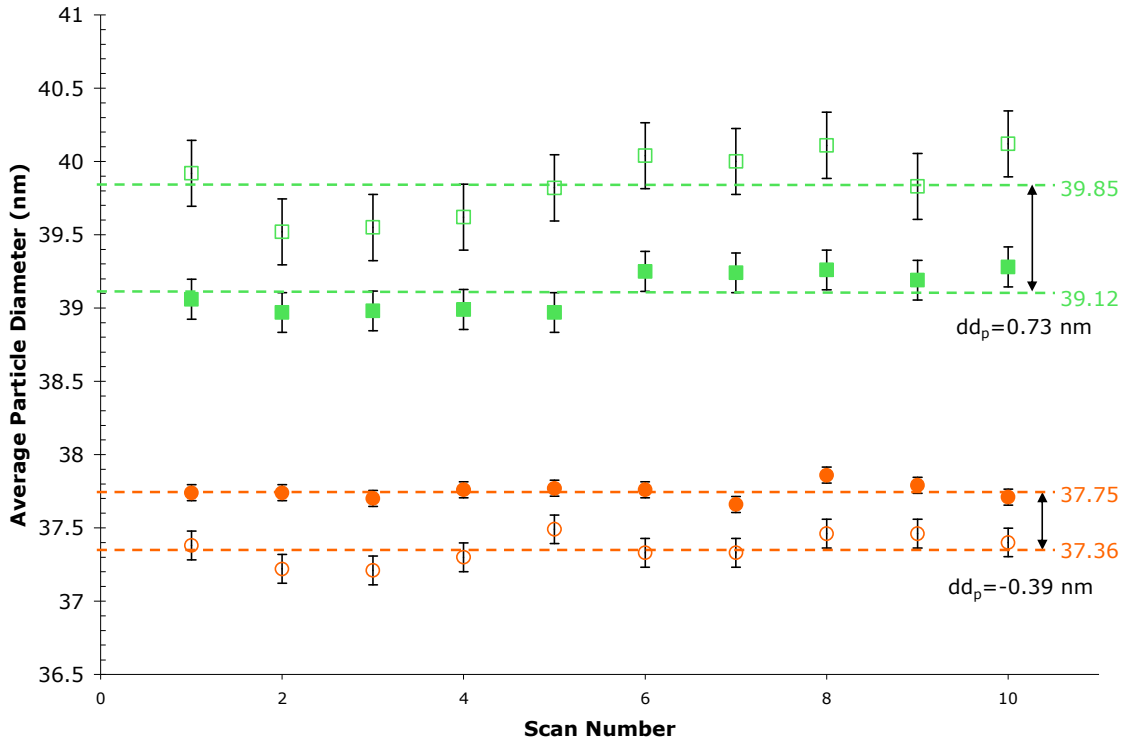

Figure 4.9: Measured particle mobility diameters for individual scans of particles collected at 660 torr heated to 1100 °C (standard deviation shown), average mobility diameter shown with dashed line (● bypass, 0% RH; ○ bypass, 90% RH; ■ acid line, 0% RH; □ acid line, 90% RH)

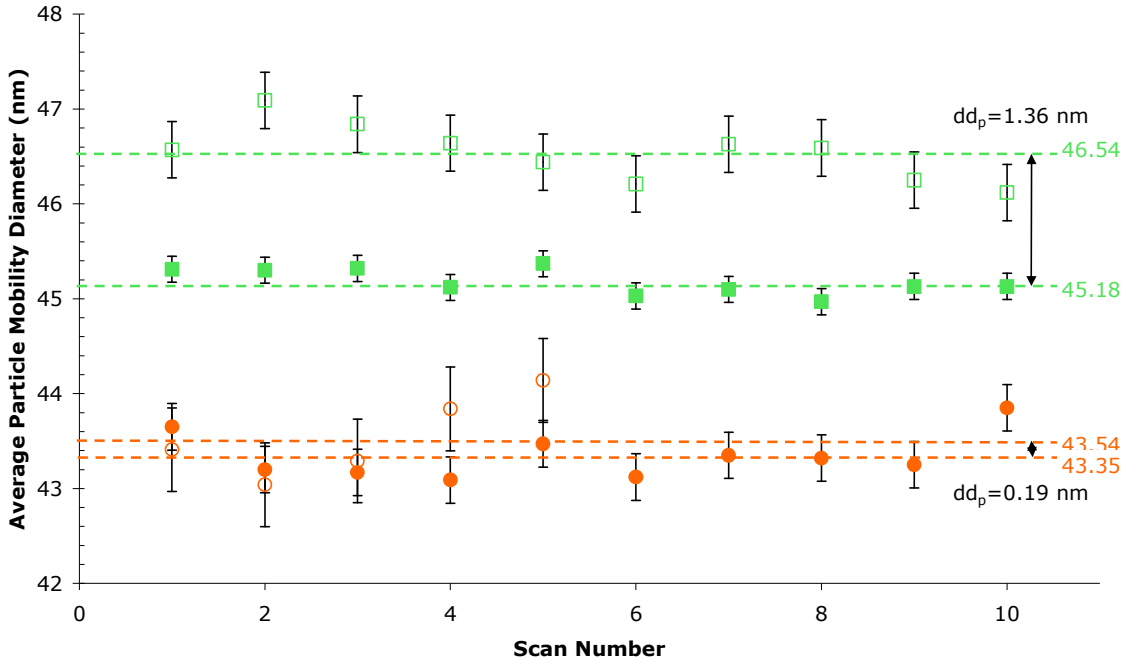

Figure 4.10: Measured particle mobility diameters for individual scans of particles collected at 680 torr with no heating (standard deviation shown), average mobility diameter shown with dashed line (● bypass, 0% RH; ○ bypass, 90% RH; ■ acid line, 0% RH; □ acid line, 90% RH)

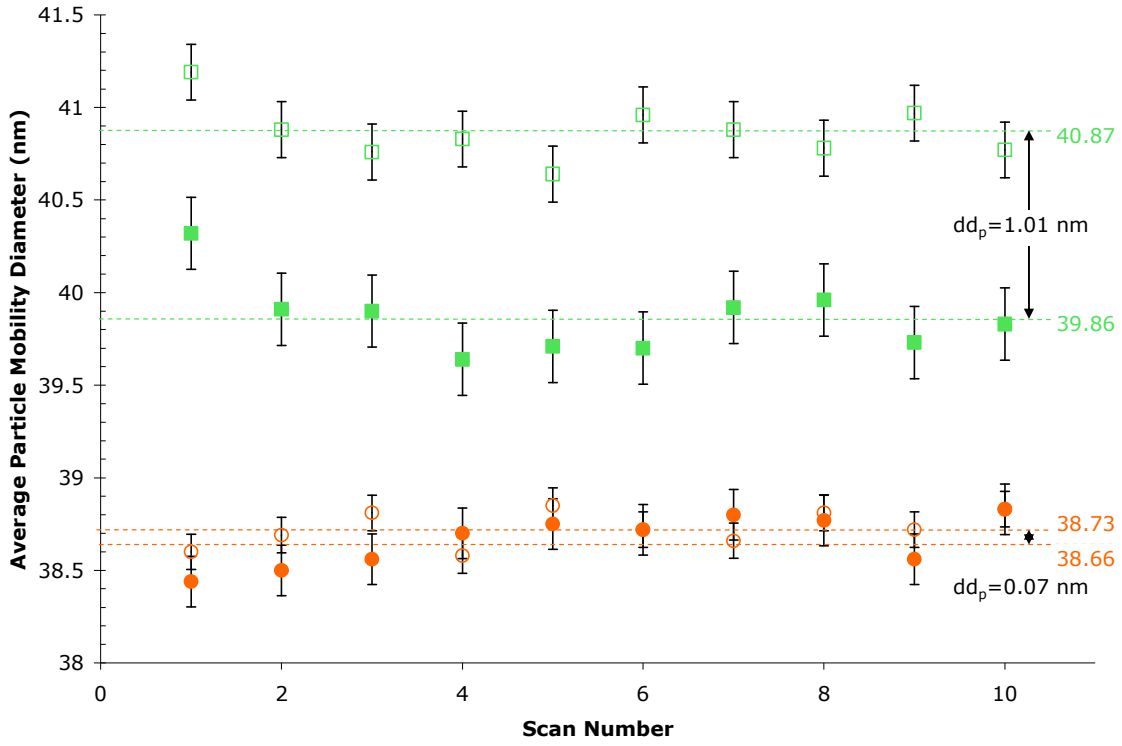

Figure 4.11: Measured particle mobility diameters for individual scans of particles collected at 680 torr heated to 800 °C (standard deviation shown), average mobility diameter shown with dashed line (● bypass, 0% RH; ○ bypass, 90% RH; ■ acid line, 0% RH; □ acid line, 90% RH)

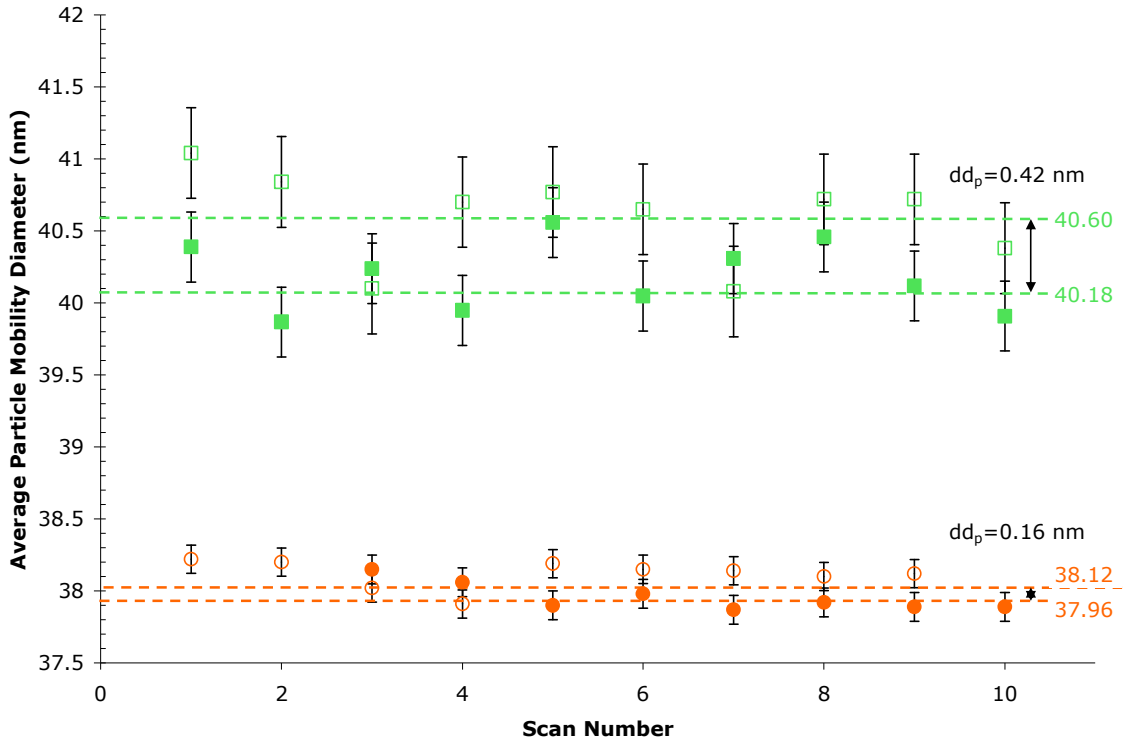

Figure 4.12: Measured particle mobility diameters for individual scans of particles collected at 680 torr heated to 1100 °C (standard deviation shown), average mobility diameter shown with dashed line (● bypass, 0% RH; ○ bypass, 90% RH; ■ acid line, 0% RH; □ acid line, 90% RH)

measured mobility diameters arising from small changes to the flow dynamics of the DMA system from diffusive lose have been minimized. Figure 13 shows two different conditions which caused particle growth or swelling from heating. These two condition sets do not, however, stand out having produced oxidative or nanostructural changes that would help explain this observation.

Figure 14 shows the changes in average mobility diameter for samples having been processed without acid in the presence of 80% RH. The change in mobility diameter for these samples is caused by water absorption without any other treatment thus reflecting the pristine particle hydrophobicity. The large variability of these Δd_p values does not allow for meaningful statistical analysis with a standard deviation greater than the average dd_p (0.2 ± 0.3 nm). In general, there is measureable growth under these conditions with the exception of one sample condition (660 Torr, 1100 °C furnace).

When sulfuric acid is added to the DMA reaction line in the absence of humidity (0% RH), particles grow an average of 1.4 ± 0.5 nm (Figure 15). This value still has a great deal of uncertainty and, but is significantly larger than the growth exhibited in Figure 14. It is important, however, that this represents growth due to acid adsorption only, no water vapor was introduced. For particles that were treated with acid and then 80% humid air, the average total growth is 2.1 ± 0.9 nm. If the acid adsorption for different reaction conditions is comparable, these particles grew by 0.7 ± 0.6 nm due to water alone after sulfuric acid treatment. Again, the uncertainty in these values is very large, but there is clearly an increase in the average water adsorption with sulfuric acid

treatment. Further modifications or improvements to the experimental apparatus may help decrease the uncertainty by providing more consistent results.

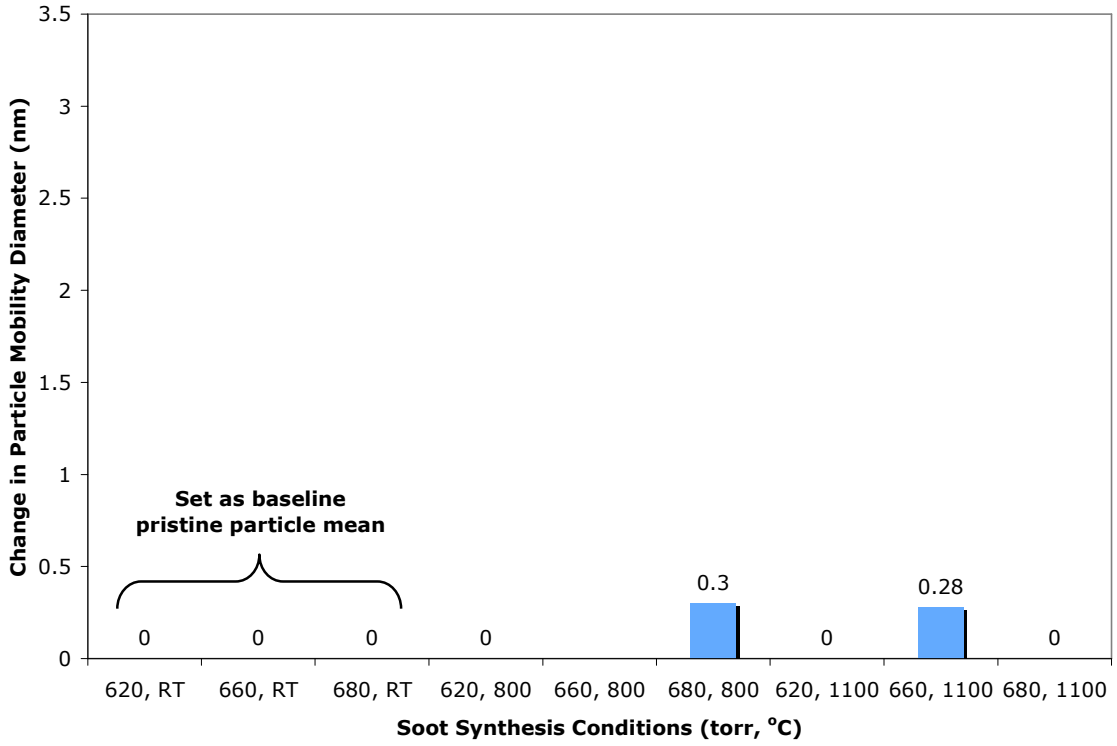

Figure 4.13: Change in mobility diameter for particles collected at the indicted (pressure, furnace temperature) conditions with no acid and 0% relative humidity.

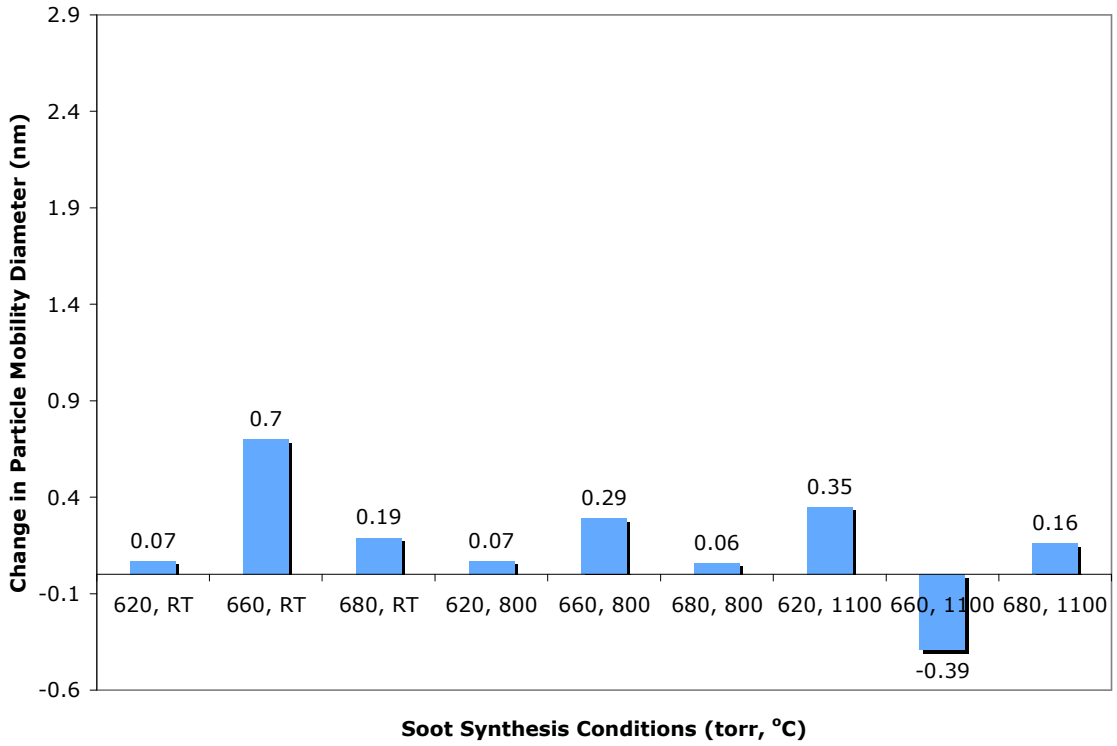

Figure 4.14: Change in mobility diameter for particles collected at the indicted (pressure, furnace temperature) conditions with no acid and 90% relative humidity.

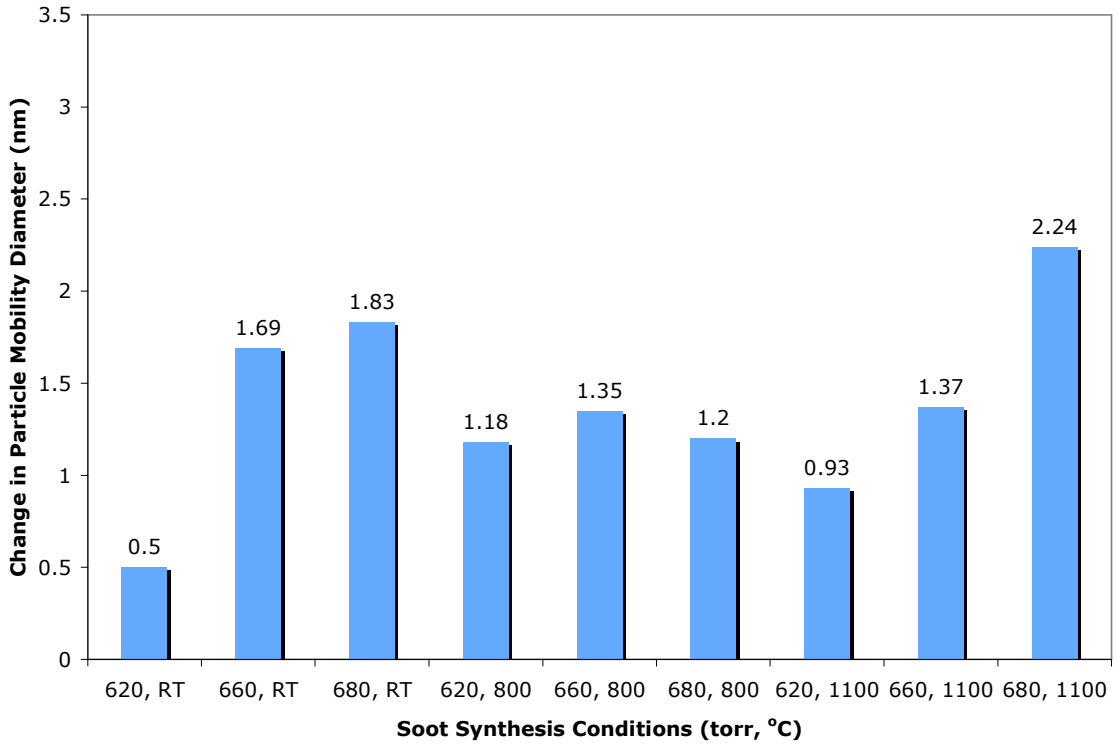

Figure 4.15: Change in mobility diameter for particles collected at the indicted (pressure, furnace temperature) conditions with 10 sccm acid and 0% relative humidity.

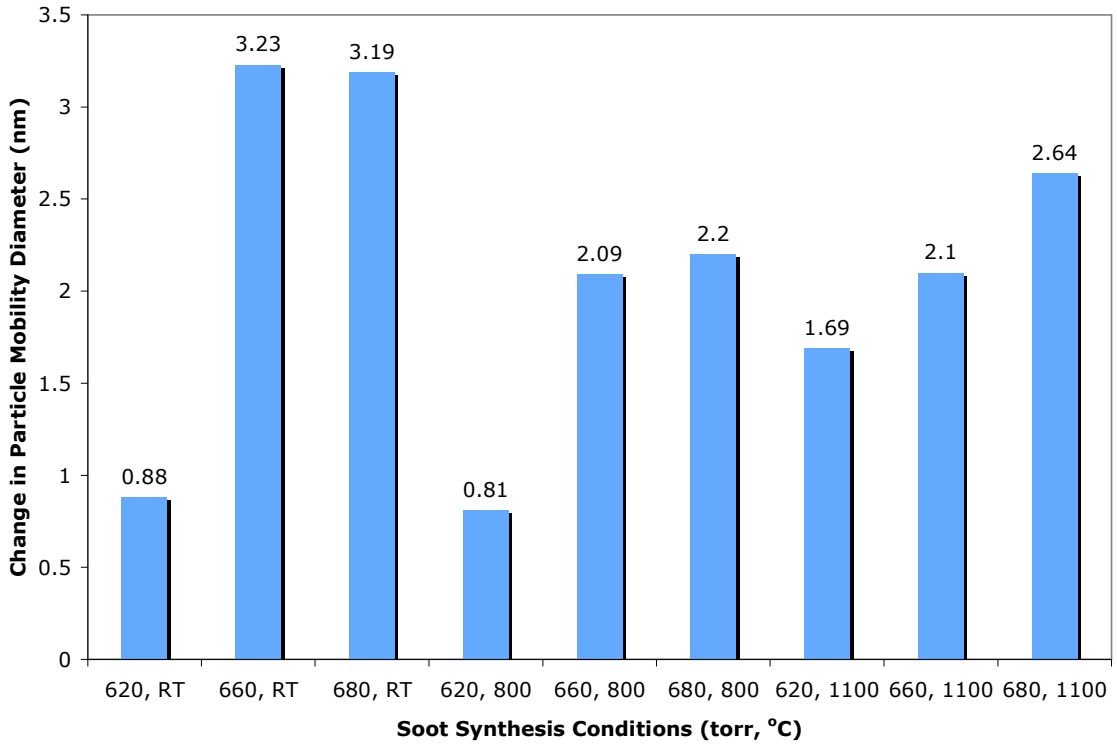

Figure 4.16: Change in mobility diameter for particles collected at the indicted (pressure, furnace temperature) conditions with 10 sccm acid and 90% relative humidity.

4.4 Discussion

For the present study, the effects of oxidative processing on sulfuric acid and water uptake of natural gas soots were under investigation. As previously reported (Chapter 3), the size of graphene crystallites within various soot particles can be controlled through the synthetic conditions and post-synthesis aerosol-phase heating. Using three operation pressures and heating the particles to various temperatures from room temperature to 1100 °C has been shown to affect crystallite size and composition. Specifically, particles processed at 620 Torr did not show any morphological or compositional correlation to processing temperature, while particles processed at higher pressures did. Namely, particles processed at 660 Torr exhibited crystallite growth up to an intermediate furnace temperature (~800 °C) and then crystallite shrinkage with increasing temperature while 680 Torr synthesis resulted in a continuous increase in crystallite size with increasing furnace temperature for all temperatures. The goal of this work was to explore any possible relationships between the oxidation of soot particles and their subsequent uptake of water. It is believed that the polar oxygen-containing functional groups on soot surfaces are the initial sites for water condensation as the particles are activated as CCN (Dubinin 1980). Due to the swelling of soot particles as water absorbs into their pores (Popovicheva, Persiantseva et al. 2008) and the hydrophobic nature of graphene without organic functionalities (Studebaker and Snow 1955; Schrader 1975), the changes in crystallite size and composition investigated previously could have a large impact on hydrophilicity. Furthermore, the suspected role of sulfates and sulfuric acid in the aging process of nascent soots in the atmosphere

(Popovicheva, Persiantseva et al. 2004; Petzold, Gysel et al. 2005) has been explored in relation to the above mentioned oxidative changes to soot structure and composition.

The data presented herein do not, however, show any correlation of the oxidative processing and water uptake. There are several possible reasons for this. First, there may be other factors that are ultimately more important in determining the water uptake characteristics of a given soot particle. The organic carbon content, for example, has been shown to strongly influence the hydrophilicity of soot nanoparticles (Barthazy, Stetzer et al.). Gravimetric analysis of samples collected under similar conditions to the ones used for this study has been performed immediately after collection as well as after 24 hour storage in a vacuum desicator at 60 °C. For these samples ~ 14% of the initial mass was pumped away in the desicator, but there were some samples with as much as 20% or as little as 10% mass loss. This difference in the initial mass fraction of what is presumed to be either adsorbed water vapor or volatile organic compounds could result in very different hydroscopic properties. It has been shown that the loss of the very first water condensate off of the soot particles or out of their micropores is irreversible (Popovicheva, Persiantseva et al. 2008), so the mass loss is most likely due to volatile organic compounds that were produced in the incomplete combustion of the natural gas fuel and subsequently adsorbed into the soot particles in the aerosol phase. Volatile organic compounds are typically very hydrophobic and would likely reduce the amount of water vapor that could adsorb into the micropores between the graphene crystallites.

Another possible cause for the experimental uncertainty is ultimately caused the diffusive loss of particles within the experimental apparatus. Soot particles have a fractal

structure and readily stick to various surfaces. When particles diffuse to the walls of the DMA system or are impacted there, the flow dynamics of the system begin to change. For some particles, the rate of particle production is so great that there can be changes in the baseline mobility diameter within several hours of beginning analysis. While large and sudden changes in the measured mobility diameter were investigated, smaller and more gradual changes could affect the confidence range of any data. This problem has been dealt with, in most cases, regular cleaning, but some data may still represent these changes in flow dynamics.

Finally, the particle mobility diameter selected for this study could result in varied behavior within the apparatus. While TEM analysis of these samples shows primary particles with diameter ~ 20 nm, the rapid agglomeration of the particles in the aerosol phase in tandem with the necessarily long residence time within the experimental apparatus, results in very few single primary particles reaching the DMA system. For this reason larger particles were selected, roughly 35 nm. These particles could represent large primary particles or agglomerates of smaller primary particles with several primary particles held together. The varied structures of particles passing into the reaction zone of the DMA results in several possible behaviors during vapor condensation. Single primary particles will expand uniformly making nearly spherical particles more spherical and producing changes in mobility diameter that correlate well with the actual change in particle diameter. Agglomerated particles, on the other hand, may rearrange upon condensation causing changes in mobility diameter not representative of the volume of condensate. While these differences should be balanced across similar samples due to the

large number of particles that are being measured, there maybe subtle differences between the size and morphology of particles arising from different synthesis conditions that would result in unpredictable mobility diameter changes. Ultimately, only a more in-depth study of the specific morphologies produced under these conditions could resolve this uncertainty.

The ability of some soot samples to absorb water and exhibit growth without sulfuric acid supports the assertion that sulfuric acid in not necessary for particle activation. While the mobility diameter of several samples did increase without sulfuric acid treatment, it is clear that, in the presence of sulfuric acid, soot particles can be activated as CCN. The aerosol-phase oxidation of soot particles producing varying graphene crystallite lengths and compositions does not reflect the expected oxidative environment soot particles are natively exposed to in the atmosphere. Specifically, the high temperatures of the tube furnace are not observed in the atmosphere. The recorded exhaust temperatures of commercial aircraft turbine and diesel engines are, however, similar to those produced in the tube furnace and any changes in CCN activity attributed to heating could theoretically be achieved within these two types of soot producing engines.

4.5 Conclusions

While it has been suggested that aging of soot in the atmosphere activating it as CCN is thought to involve adsorption of water soluble salts (Kotzick and Niessner 1999) or oxidative species such as H_2SO_4, O_3, or HNO_3 (Kirchner, Scheer et al. 2000), the controlled aerosol-phase oxidation of natural gas soot had no measureable affect on water uptake. The oxidative process under investigation may not have been a good surrogate for atmospheric oxidation considering the high temperatures achieved within the tube furnace. This oxidative process could apply more directly to the conditions found within jet turbine or diesel engine exhaust systems. The adsorption of sulfuric acid onto soot particles has been shown to aid in water uptake and presumably the activation of particles as CCN.

References

Chapter 1

Andrews, E. and S. M. Larson (1993). Environ. Sci. Technol 27: 857.

Aubin, D. G. and J. P. Abbatt (2003). J. Phys. Chem. A 107: 11030.

Baron, P. A. and K. Willeke (1993). Aerosol Fundamentals. In: K. Willeke and P. A. Baron (ed) Aerosol Measurement: Principles Techniques and Applications. John Wiley & Sons, Inc., New York, 8-22.

Baron, P. A. and K. Willeke (1993). Bridging Science and Application in Aerosol Measurement. In: K. Willeke and P. A. Baron (ed) Aerosol Measurement: Principles Techniques and Applications. John Wiley & Sons, Inc., New York, 3-7.

Brown, D. M., M. R. Wilson, et al. (2001). Size-Dependent Proinflammatory Effects of Ultrafine Polystyrene Particles: A Role for Surface Area and Oxidative Stress in the Enhanced Activity of Ultrafines. Toxicology and Applied Pharmacology 175: 191-199.

Buffat, P. and J. P. Borel (1976). Size effect on the melting temperature of gold particles. Physical Review A 13: 2287.

Buriak, J. M. (2002). Organometallic chemistry on silicon and germanium surfaces. Chem Rev 102: 1271-308.

Burleson, D. J., M. D. Driessen, et al. (2004). On the Characterization of Environmental Nanoparticles. Journal of Environmental Science & Health, Part A: Toxic/Hazardous Substances & Environmental Engineering 39: 2707-2753.

Cassee, F., H. Muijser, et al. (2002). Particle size-dependent total mass deposition in lungs determines inhalation toxicity of cadmium chloride aerosols in rats. Application of a multiple path dosimetry model. Archives of Toxicology 76: 277-286.

Chughtai, A. R., M. E. Brooks, et al. (1996). J. Geophys. Res. Atmos. 101: 19505.

Chughtai, A. R., G. R. Williams, et al. (1999). Carbonaceous particle hydration. Atmospheric Environment 33: 2679-2687.

Dabrowski, J. and H. Mussig (2000). Silicon Surfaces and Formation of Interfaces. World Scientific, New Jersey.

DeCarlo, P., J. Slowik, et al. (2004). Particle Morphology and Density Characterization by Combined Mobility and Aerodynamic Diameter Measurements. Part 1: Theory. Aerosol Science and Technology 38: 1185 - 1205.

Decesari, S., M. C. Facchini, et al. (2002). Water soluble organic compounds formed by oxidation of soot. Atmospheric Environment 36: 1827-1832.

DeMott, P. J., Y. Chen, et al. (1999). Ice formation by black carbon particles. Geophys. Res. Lett. 26: 2429-2432.

Diehl, K. and S. K. Mitra (1998). A laboratory study of the effects of a kerosene-burner exhaust on ice nucleation and the evaporation rate of ice crystals. Atmospheric Environment 32: 3145-3151.

Dubinin, M. M. (1980). Carbon. 18: 355.

He, X. x., K. Wang, et al. (2003). Bioconjugated Nanoparticles for DNA Protection from Cleavage. J. Am. Chem. Soc. 125: 7168-7169.

Holm, J. and J. T. Roberts (2007). Surface chemistry of aerosolized silicon nanoparticles: evolution and desorption of hydrogen from 6-nm diameter particles. J Am Chem Soc 129: 2496-503.

Hua, F., F. Erogbogbo, et al. (2006). Organically capped silicon nanoparticles with blue photoluminescence prepared by hydrosilylation followed by oxidation. Langmuir 22: 4363-70.

Jensen, E. J. and O. B. Toon (1997). The potential impact of soot particles from aircraft exhaust on cirrus clouds. Geophys. Res. Lett. 24: 249-252.

John, W. (1993). The Characteristics of Environmental and Laboratory-Generated Aerosols. In: K. Willeke and P. A. Baron (ed) Aerosol Measurement: Principles Techniques and Applications. John Wiley & Sons, Inc., New York, 54-76.

Karcher, B., T. Peter, et al. (1996). The Initial Composition of Jet Condensation Trails. Journal of the Atmospheric Sciences 53: 3066-3083.

Karn, B. (2005). Overview of Environmental Applications and Implications. How Does Nanotechnology Relate to the Environment? Or Why Are We Here? . In: B. Karn, T. Masciangioli, W.-x. Zhang, V. Colvin and P. Alivisatos (ed) Nanotechnology and the Environment Applicaitons and Implications. American Chemical Society, Washington D.C., 2-6.

Keller, A., M. Fierz, et al. (2001). Surface science with nanosized particles in a carrier gas. Journal of Vacuum Science & Technology A: Vacuum, Surfaces, and Films 19: 1-8.

Kirchner, U., V. Scheer, et al. (2000). FTIR Spectroscopic Investigation of the Mechanism and Kinetics of the Heterogeneous Reactions of NO2 and HNO3 with Soot. The Journal of Physical Chemistry A 104: 8908-8915.

Kotzick, R., U. Panne, et al. (1997). Changes in condensation properties of ultrafine carbon particles subjected to oxidation by ozone. Journal of Aerosol Science 28: 725-735.

Kristensson, A., J. F. Gayet, et al. (2000). Geophys. Res. Lett 27: 681.

Kuhn, M., A. Petzold, et al. (1998). Particle composition of a young condensation trail and of upper tropospheric aerosol. Geophys. Res. Lett. 25: 2679-2682.

Lammel, G. and T. Novakov (1995). Water nucleation properties of carbon black and diesel soot particles. Atmospheric Environment 29: 813-823.

Lehtimaki, M. and K. Willeke (1993). Measurement Methods. In: K. Willeke and P. A. Baron (ed) Aerosol Measurement: Principles Techniques and Applications. John Wiley & Sons, Inc., New York, 112-129.

Liao, Y.-C., A. M. Nienow, et al. (2006). Surface Chemistry of Aerosolized Nanoparticles:Thermal Oxidation of Silicon. J. Phys. Chem. B 110: 6190-6197.

Liao, Y. C. and J. T. Roberts (2006). Self-assembly of organic monolayers on aerosolized silicon nanoparticles. J Am Chem Soc 128: 9061-5.

Masciangioli, T. M. and W.-x. Zhang (2005). Environmental Technologies at the Nanometer-Scale. In: B. Karn, T. Masciangioli, W.-x. Zhang, V. Colvin and P. Alivisatos (ed) Nanotechnology and the Environment Applicaitons and Implications. American Chemical Society, Washington D.C., 7-12.

Maynard, A. and E. Kuempel (2005). Airborne Nanostructured Particles and Occupational Health. Journal of Nanoparticle Research 7: 587-614.

McMurry, P. H. (2000). A review of atmospheric aerosol measurements. Atmospheric Environment 34: 1959-1999.

Mulhall, D. (2005). Reassessing Risk Assessment. In: B. Karn, T. Masciangioli, W.-x. Zhang, V. Colvin and P. Alivisatos (ed) Nanotechnology and the Environment Applicaitons and Implications. American Chemical Society, Washington D.C., 13-20.

Oberdorster, G. (2005). Effects and Fate of Inhaled Ultrafine Particles. In: B. Karn, T. Masciangioli, W.-x. Zhang, V. Colvin and P. Alivisatos (ed) Nanotechnology and the Environment Applicaitons and Implications. American Chemical Society, Washington D.C., 37-59.

Persiantseva, N. M., O. B. Popovicheva, et al. (2004). Wetting and hydration of insoluble soot particles in the upper troposphere. Journal of Environmental Monitoring 6: 939-945.

Polschl, U., T. L. C. Schauer, et al. (2001). Interaction of Ozone and Water Vapor with Spark Discharge Soot Aerosol Particles Coated with Benzo[a]pyrene: O3 and H2O Adsorption, Benzo[a]pyrene Degradation, and Atmospheric Implications. J. Phys. Chem. A 105: 4029-4041.

Popovicheva, O., N. M. Persiantseva, et al. (2008). Water interaction with hydrophobic and hydrophilic soot particles. Physical Chemistry Chemical Physics 10: 2332-2344.

Seinfeld, J. H. and S. N. Pandis (1998). Atmospheric Chemistry and Physics: From Air Pollution to Climate Change.

Seinfeld, J. H. and J. F. Pankow (2003). ORGANIC ATMOSPHERIC PARTICULATE MATERIAL. Annual Review of Physical Chemistry 54: 121-140.

Sengupta, A., N. Brar, et al. (2007). Bioaerosol detection and characterization by surface-enhanced Raman spectroscopy. Journal of Colloid and Interface Science 309: 36-43.

Smith, D. M. and A. R. Chughtai (1995). Colloids Surf. A 105: 47.

Smith, D. M. and A. R. Chughtai (1997). J. Atmos. Chem. 26: 77.

Smith, J. N., K. F. Moore, et al. (2005). Chemical composition of atmospheric nanoparticles during nucleation events in Atlanta. J. Geophys. Res. 110: D22S03.

Willeke, K. and P. A. Baron (1993). Aerosol Measurement: Principles Techniques and Applications. John Wiley & Sons, Inc., New York.

Zou, J., R. K. Baldwin, et al. (2004). Solution Synthesis of Ultrastable Luminescent Siloxane-Coated Silicon Nanoparticles. Nano Letters 4: 1181-1186.

Zuberi, B., K. S. Johnson, et al. (2005). Hydrophilic properties of aged soot. Geophys. Res. Lett. 32: L01807.

Chapter 2

Bapat, A., M. Gatti, et al. (2007). A plasma process for the synthesis of cubic-shaped silicon nanocrystals for nanoelectronic devices. JOURNAL OF PHYSICS D: APPLIED PHYSICS 40: 2247-2257. DOI: 10.1088/0022-3727/40/8/S03

Buffat, P. and J. P. Borel (1976). Size effect on the melting temperature of gold particles. Physical Review A 13: 2287. DOI: 10.1103/PhysRevA.13.2287

Burleson, D. J., M. D. Driessen, et al. (2004). On the Characterization of Environmental Nanoparticles. Journal of Environmental Science & Health, Part A: Toxic/Hazardous Substances & Environmental Engineering 39: 2707-2753. DOI: 10.1081/LESA-200027029

Carter, R. S., S. J. Harley, et al. (2005). Use of NMR Spectroscopy in the Synthesis and Characterization of Air- and Water-Stable Silicon Nanoparticles from Porous Silicon. Chem. Mater. 17: 2932-2939. DOI: 10.1021/cm040377u

Chabal, Y. J., M. K. Weldon, et al. (2001). Fundamental Aspects of Silicon Oxidation. Springer-Verlag, New York.

Dabrowski, J. and H. Mussig (2000). Silicon Surfaces and Formation of Interfaces. World Scientific, New Jersey.

Dong, Y. (2005) Devices made on single crystal silicon nanoparticles. Dissertation, University of Minnesota

Fritzsche, H. (1984). Electronic Properties of Surfaces in a-Si:H. In: J. I. Pankove (ed) Semiconductors and Semimetals: Hydrogenated Amorphous Silicon. Academic Press, Inc., New York, 314-316.

Hawa, T. and M. R. Zachariah (2004). Internal Pressure and Surface Tension of Bare and Hydrogen Coated Silicon Nanoparticles. J. Chem. Phys. 121: 9043. DOI: 10.1063/1.1797073

Holm, J. and J. T. Roberts (2007). Surface chemistry of aerosolized silicon nanoparticles: evolution and desorption of hydrogen from 6-nm diameter particles. J Am Chem Soc 129: 2496-503. DOI: 10.1021/ja0658970

Holm, J. and J. T. Roberts (2007). Thermal Oxidation of 6 nm Aerosolized Silicon Nanoparticles: Size and Surface Chemistry Changes. Langmuir 23: 11217-11224. DOI: 10.1021/10010869

Holm, J. and J. T. Roberts (2009). Sintering, Coalescence, and Compositional Changes of Hydrogen-Terminated Silicon Nanoparticles as a Function of Temperature. The Journal of Physical Chemistry C 113: 15955-15963. DOI: 10.1021/jp905748j

Hua, F., F. Erogbogbo, et al. (2006). Organically capped silicon nanoparticles with blue photoluminescence prepared by hydrosilylation followed by oxidation. Langmuir 22: 4363-70. DOI: 10.1021/la0529106

Kortshagen, U., L. Mangolini, et al. (2007). Plasma synthesis of semiconductor nanocrystals for nanoelectronics and luminescence applications. Journal of Nanoparticle Research 9: 39-52. DOI: 10.1007/s11051-006-9174-6

Kovalevskii, A. A., A. A. Shevchenok, et al. (2008). Oxidation behavior of micro- and nanostructured silicon powders. Inorganic Materials 44: 445-449. DOI: 10.1134/S0020168508050014

Liao, Y.-C., A. M. Nienow, et al. (2006). Surface Chemistry of Aerosolized Nanoparticles:Thermal Oxidation of Silicon. J. Phys. Chem. B 110: 6190-6197. DOI: 10.1021/jp054195e

Liao, Y. C. and J. T. Roberts (2006). Self-assembly of organic monolayers on aerosolized silicon nanoparticles. J Am Chem Soc 128: 9061-5. DOI: 10.1021/ja0611238

Mangolini, L., E. Thimsen, et al. (2005). High-Yield Plasma Synthesis of Luminescent Silicon Nanocrystals. Nano Lett. 5: 655-659. DOI: 10.1021/nl050066y

Marra, D. C., E. A. Edelberg, et al. (1998). Silicon hydride composition of plasma-deposited hydrogenated amorphous and nanocrystalline silicon films and surfaces. Journal of Vacuum Science & Technology A: Vacuum, Surfaces, and Films 16: 3199-3210. DOI: 10.1116/1.581520

Marra, D. C., W. M. M. Kessels, et al. (2003). Surface hydride composition of plasma deposited hydrogenated amorphous silicon: in situ infrared study of ion flux and temperature dependence. Surface Science 530: 1-16. DOI: 10.1016/S0039-6028(03)00396-0

Matsumoto, T., A. I. Belogorokhov, et al. (2000). The effect of deuterium on the optical properties of free-standing porous silicon layers. Nanotechnology 11: 340-347. DOI: 10.1088/0957-4484/11/4/330

Mayeri, D., B. L. Phillips, et al. (2001). NMR Study of the Synthesis of Alkyl-Terminated Silicon Nanoparticles from the Reaction of SiCl4 with the Zintl Salt, NaSi. Chem. Mater. 13: 765-770. DOI: 10.1021/cm000418w

Maynard, A. and E. Kuempel (2005). Airborne Nanostructured Particles and Occupational Health. Journal of Nanoparticle Research 7: 587-614. DOI: 10.1007/s11051-005-6770-9

Mills, R. L., B. Dhandapani, et al. (2003). Highly stable amorphous silicon hydride. Solar Energy Materials and Solar Cells 80: 1-20. DOI: 10.1016/S0927-0248(03)00107-7

Miura, T.-a., M. Niwano, et al. (1996). Initial stages of oxidation of hydrogen-terminated Si surface stored in air. Applied Surface Science 100-101: 454-459. DOI: 10.1016/0169-4332(96)00319-4

Nayfeh, M. H. (2003). Synthesis, Functionalization and Surface Treatment of Nanoparticles. American Scientific Publishers, Stevenson Ranch, CA.

Nienow, A. M. and J. T. Roberts (2006). Chemical Vapor Deposition of Zirconium Oxide on Aerosolized Silicon Nanoparticles. Chem. Mater. 18: 5571-5577. DOI: 10.1021/cm060883e

NIST X-ray Photoelectron Spectrsocopy Database, Version 3.5 (National Institute of Standards and Technology, Gaithersburg, 2003); http://srdata.nist.gov/exp/.

Ogata, Y. H., N. Yoshimi, et al. (2001). Structural change in p-type porous silicon by thermal annealing. Journal of Applied Physics 90: 6487-6492. DOI: 10.1063/1.1416862

Pai, P. G., S. S. Chao, et al. (1986). Infrared spectroscopic study of SiO[sub x] films produced by plasma enhanced chemical vapor deposition. Journal of Vacuum

Science & Technology A: Vacuum, Surfaces, and Films 4: 689-694. DOI: 10.1116/1.573833

Rogozhina, E. V., D. A. Eckhoff, et al. (2006). Carboxyl functionalization of ultrasmall luminescent silicon nanoparticles through thermal hydrosilylation. Journal of Materials Chemistry 16: 1421-1430. DOI: 10.1039/b509868h

Schulmeister, K. and W. Mader (2003). TEM investigation on the structure of amorphous silicon monoxide. Journal of Non-Crystalline Solids 320: 143-150. DOI: 10.1016/S0022-3093(03)00029-2

Tersoff, J., Y. Tu, et al. (1998). Effect of curvature and stress on reaction rates at solid interfaces. Applied Physics Letters 73: 2328-2330. DOI: 10.1063/1.121812

Yi, L. X., J. Heitmann, et al. (2003). Phase separation of thin SiO layers in amorphous SiO/SiO2 superlattices during annealing. Journal of Physics: Condensed Matter 15: S2887-S2895. DOI: 10.1088/0953-8984/15/39/012

Zou, J., R. K. Baldwin, et al. (2004). Solution Synthesis of Ultrastable Luminescent Siloxane-Coated Silicon Nanoparticles. Nano Letters 4: 1181-1186. DOI: 10.1021/nl0497373

Chapter 3

Ackerman, A. S., O. B. Toon, et al. (2000). Reduction of Tropical Cloudiness by Soot. Science 288: 1042-1047.

Al-Jishi, R., B. S. Elman, et al. (1982). 24. Lattice dynamical model for graphite. Carbon 20: 127-127.

Cachier, H. (1998). IUPAC Series on Analytical and Physical Chemistry of Environmental Systems.

Cain, J. P., P. L. Gassman, et al. (2010). Micro-FTIR study of soot chemical composition - evidence of aliphatic hydrocarbons on nascent soot surfaces. Physical Chemistry Chemical Physics 12: 5206-5218.

Chen, C.-C., L.-C. Hung, et al. (1993). Heterogeneous Nucleation of Water Vapor on Particles of SiO2, Al2O3, TiO2, and Carbon Black. Journal of Colloid and Interface Science 157: 465-477.

Chughtai, A. R., G. R. Williams, et al. (1999). Carbonaceous particle hydration. Atmospheric Environment 33: 2679-2687.

Dippel, B., H. Jander, et al. (1999). NIR FT Raman spectroscopic study of flame soot. Physical Chemistry Chemical Physics 1: 4707-4712.

Dubinin, M. M. (1980). Carbon. 18: 355.

Gregg, S. J. and K. S. W. Sing (1982). Adsorption, Surface Area and Porosity. Academic Press, New York.

Gysel, M., S. Nyeki, et al. (2003). Properties of jet engine combustion particles during the PartEmis experiment: Hygroscopicity at subsaturated conditions. Geophys. Res. Lett. 30: 1566.

Harrison, R. M. and C. A. Pio (1983). Kinetics of SO2 oxidation over carbonaceous particles in the presence of H2O, NO2, NH3 and O3. Atmospheric Environment (1967) 17: 1261-1275.

Jacobson, M. Z. (2010). Short-term effects of controlling fossil-fuel soot, biofuel soot and gases, and methane on climate, Arctic ice, and air pollution health. J. Geophys. Res. 115: D14209.

Jawhari, T., A. Roid, et al. (1995). Raman spectroscopic characterization of some commercially available carbon black materials. Carbon 33: 1561-1565.

Kuhn, M., A. Petzold, et al. (1998). Particle composition of a young condensation trail and of upper tropospheric aerosol. Geophys. Res. Lett. 25: 2679-2682.

Lee, K. O., R. Cole, et al. (2002). Morphological investigation of the microstructure, dimensions, and fractal geometry of diesel particulates. Proceedings of the Combustion Institute 29: 647-653.

Leifeld, J. (2007). Thermal stability of black carbon characterised by oxidative differential scanning calorimetry. Organic Geochemistry 38: 112-127.

Mernagh, T. P., R. P. Cooney, et al. (1984). Raman spectra of Graphon carbon black. Carbon 22: 39-42.

Nakahara, M. and Y. Sanada (1995). FT-IR ATR spectroscopy of the edge surface of pyrolytic graphite and its surface/PVC interface. Journal of Materials Science 30: 4363 - 4368.

Nienow, A. M. and J. T. Roberts (2006). HETEROGENEOUS CHEMISTRY OF CARBON AEROSOLS. Annual Review of Physical Chemistry 57: 105-128.

Persiantseva, N. M., O. B. Popovicheva, et al. (2004). Wetting and hydration of insoluble soot particles in the upper troposphere. Journal of Environmental Monitoring 6: 939-945.

Popovicheva, O., N. M. Persiantseva, et al. (2008). Water interaction with hydrophobic and hydrophilic soot particles. Physical Chemistry Chemical Physics 10: 2332-2344.

Pukkala, E., J. I. Martinsen, et al. (2009). Occupation and cancer ,Äì follow-up of 15 million people in five Nordic countries. Acta Oncologica 48: 646-790.

Sadezky, A., H. Muckenhuber, et al. (2005). Raman microspectroscopy of soot and related carbonaceous materials: Spectral analysis and structural information. Carbon 43: 1731-1742.

Schrader, M. E. (1975). Ultrahigh vacuum techniques in the measurement of contact angles. IV. Water on graphite (0001). J. Phys. Chem. 79: 2508-2515.

Shaffer, M. S. P., X. Fan, et al. (1998). Dispersion and packaging of carbon nanotubes. Carbon 36: 1603 - 1612.

Soewono, A. and S. Rogak (2009). Morphology and Microstructure of Engine-Emitted Particulates. SAE International 1906-1915.

Spira-Cohen, A., L. C. Chen, et al. (2011). Personal Exposures to Traffic-Related Air Pollution and Acute Respiratory Health among Bronx Schoolchildren with Asthma. Environ Health Perspect 119.

Stratakis, G. A. and A. M. Stamatelos (2003). Thermogravimetric analysis of soot emitted by a modern diesel engine run on catalyst-doped fuel. Combustion and Flame 132: 157-169.

Tuinstra, F. and J. L. Koenig (1970). Raman Spectrum of Graphite. Journal of Chemical Physics 1126-1130.

Wal, R. L. V. and A. J. Tomasek (2004). Soot nanostructure: dependence upon synthesis conditions. Combustion and Flame 136: 129-140.

Wang, Y., D. C. Alsmeyer, et al. (1990). Raman spectroscopy of carbon materials: structural basis of observed spectra. Chemistry of Materials 2: 557-563.

Zuberi, B., K. S. Johnson, et al. (2005). Hydrophilic properties of aged soot. Geophys. Res. Lett. 32: L01807.

Chapter 4

Ackerman, A. S., O. B. Toon, et al. (2000). Reduction of Tropical Cloudiness by Soot. Science 288: 1042-1047.

Barthazy, E., O. Stetzer, et al. Water uptake of soot particles emitted from a jing-cast soot generator.

Brodzinsky, R., S. G. Chang, et al. (1980). Kinetics and mechanism for the catalytic oxidation of sulfur dioxide on carbon in aqueous suspensions. The Journal of Physical Chemistry 84: 3354-3358.

Cachier, H. (1998). IUPAC Series on Analytical and Physical Chemistry of Environmental Systems.

Chen, C.-C., L.-C. Hung, et al. (1993). Heterogeneous Nucleation of Water Vapor on Particles of SiO2, Al2O3, TiO2, and Carbon Black. Journal of Colloid and Interface Science 157: 465-477.

Chughtai, A. R., M. E. Brooks, et al. (1996). J. Geophys. Res. Atmos. 101: 19505.

Decesari, S., M. C. Facchini, et al. (2002). Water soluble organic compounds formed by oxidation of soot. Atmospheric Environment 36: 1827-1832.

Dubinin, M. M. (1980). Carbon. 18: 355.

Harrison, R. M. and C. A. Pio (1983). Kinetics of SO2 oxidation over carbonaceous particles in the presence of H2O, NO2, NH3 and O3. Atmospheric Environment (1967) 17: 1261-1275.

Jacobson, M. Z. (2002). Atmospheric Pollution: History, Science, and Regulation.

Jensen, E. J. and O. B. Toon (1997). The potential impact of soot particles from aircraft exhaust on cirrus clouds. Geophys. Res. Lett. 24: 249-252.

Karcher, B., T. Peter, et al. (1996). The Initial Composition of Jet Condensation Trails. Journal of the Atmospheric Sciences 53: 3066-3083.

Kirchner, U., V. Scheer, et al. (2000). FTIR Spectroscopic Investigation of the Mechanism and Kinetics of the Heterogeneous Reactions of NO2 and HNO3 with Soot. The Journal of Physical Chemistry A 104: 8908-8915.

Kotzick, R. and R. Niessner (1999). The effects of aging processes on critical supersaturation ratios of ultrafine carbon aerosols. Atmospheric Environment 33: 2669-2677.

Kuhn, M., A. Petzold, et al. (1998). Particle composition of a young condensation trail and of upper tropospheric aerosol. Geophys. Res. Lett. 25: 2679-2682.

Mikhailov, E. F., S. S. Vlasenko, et al. (2001). Interaction of soot aerosol particles with water droplets: influence of surface hydrophilicity. Journal of Aerosol Science 32: 697-711.

Nienow, A. M. and J. T. Roberts (2006). HETEROGENEOUS CHEMISTRY OF CARBON AEROSOLS. Annual Review of Physical Chemistry 57: 105-128.

Persiantseva, N. M., O. B. Popovicheva, et al. (2004). Wetting and hydration of insoluble soot particles in the upper troposphere. Journal of Environmental Monitoring 6: 939-945.

Petzold, A., M. Gysel, et al. (2005). On the effects of organic matter and sulfur-containing compounds on the CCN activation of combustion particles. Atmospheric Chemistry and Physics 5: 3187-3203.

Popovicheva, O., N. M. Persiantseva, et al. (2008). Water interaction with hydrophobic and hydrophilic soot particles. Physical Chemistry Chemical Physics 10: 2332-2344.

Popovicheva, O. B., N. M. Persiantseva, et al. (2004). Aircraft engine soot as contrail nuclei. Geophys. Res. Lett. 31: L11104.

Schrader, M. E. (1975). Ultrahigh vacuum techniques in the measurement of contact angles. IV. Water on graphite (0001). J. Phys. Chem. 79: 2508-2515.

Seinfeld, J. H. and S. N. Pandis (1998). Atmospheric Chemistry and Physics: From Air Pollution to Climate Change.

Sheridan, P. J., C. A. Brock, et al. (1994). Aerosol particles in the upper troposphere and lower stratosphere: Elemental composition and morphology of individual particles in northern midlatitudes. Geophys. Res. Lett. 21: 2587-2590.

Smith, D. M. and A. R. Chughtai (1997). J. Atmos. Chem. 26: 77.

Studebaker, M. L. and C. W. Snow (1955). The Influence of Ultimate Composition upon the Wettability of Carbon Blacks. The Journal of Physical Chemistry 59: 973-976.

Weingartner, E., H. Burtscher, et al. (1997). Atmos. Environ. 31: 2311.

Zuberi, B., K. S. Johnson, et al. (2005). Hydrophilic properties of aged soot. Geophys. Res. Lett. 32: L01807.